University of Southampton

Faculty of Engineering and the Environment

Aerodynamics and Flight Mechanics Research Group

High-order Computations on Aerofoil-Gust Interaction Noise and the Effects of Wavy Leading Edges

by

Alex Siu Hong LAU

Thesis for the Degree of Doctor of Philosophy

October 2012

UNIVERSITY OF SOUTHAMPTON

ABSTRACT

FACULTY OF ENGINEERING AND THE ENVIRONMENT

Aerodynamics and Flight Mechanics Research Group

Doctor of Philosophy

HIGH-ORDER COMPUTATIONS ON AEROFOIL-GUST INTERACTION NOISE AND THE EFFECTS OF WAVY LEADING EDGES

by

Alex Siu Hong Lau

High-order accurate numerical simulations are performed to investigate the effects of wavy leading edges on aerofoil-gust interaction (AGI) noise. The present study is based on periodic velocity disturbances predominantly in streamwise (x-) and vertical (y-) directions that are mainly responsible for the surface pressure fluctuation of an aerofoil. The perturbed velocity components of the present gust model do not vary in the spanwise (z-) direction. In general, the present results show that wavy leading edges lead to reduced AGI noise. Under the current incident gusts, it is found that the ratio of the wavy leading-edge peak-to-peak amplitude (LEA) to the longitudinal wavelength of the incident gust (λ_g) is the most important factor for the reduction of AGI noise. It is observed that AGI noise reduces with increasing LEA/λ_g, and significant noise reduction can be achieved for $LEA/\lambda_g \geq 0.3$. The present results also suggest that any two different cases with the same LEA/λ_g lead to a strong similarity in their profiles of noise reduction relative to the straight leading-edge case. The wavelength of wavy leading edges (LEW), however, shows minor influence on the reduction of AGI noise under the present gust profiles used. Nevertheless, the present results show that a meaningful improvement in noise reduction may be achieved when $1.0 \leqslant LEW/\lambda_g \leqslant 1.5$. In addition, it is found that the beneficial effects of wavy leading edges are maintained for various angles of attack and aerofoil thicknesses. Also, wavy leading edges remain effective in reducing AGI noise for gust profiles containing multiple frequency components. It is discovered in the current research that wavy leading edges result in incoherent response time to the incident gust across the span, which causes a decreased level of surface pressure fluctuations, hence a reduced level of AGI noise.

DECLARATION OF AUTHORSHIP

I, Alex Siu Hong Lau

declare that the thesis entitled

HIGH-ORDER COMPUTATIONS ON AEROFOIL-GUST INTERACTION NOISE
AND THE
EFFECTS OF WAVY LEADING EDGES

and the work presented in the thesis are both my own, and have been generated by me as the result of my own original research. I confirm that:

- this work was done wholly or mainly while in candidature for a research degree at this University;
- where any part of this thesis has previously been submitted for a degree or any other qualification at this University or any other institution, this has been clearly stated;
- where I have consulted the published work of others, this is always clearly attributed;
- where I have quoted from the work of others, the source is always given. With the exception of such quotations, this thesis is entirely my own work;
- I have acknowledged all main sources of help;
- where the thesis is based on work done by myself jointly with others, I have made clearly exactly what was done by others and what I have contributed myself;
- parts of this work have been published as:
  J.W. Kim, A.S.H. Lau and N.D. Sandham, "Proposed boundary conditions for gust-airfoil interaction noise", *AIAA J. Technical Notes*, vol 48(11), pp. 2705-2710, 2010.

Signed:

Date:

ACKNOWLEDGEMENT

I would like to express my deepest gratitude to my supervisors Professor Neil D. Sandham, and in particular, Dr. Jae Wook Kim. I would not have been able to complete the present research without Dr. Jae Wook Kim's valuable advise, useful yet casual discussions, guidance and patience. There were times when the works were not advancing as fast as we had hoped. His support and encouragement were one of the major factors which enable me to complete the current research.

I would also like to thank Vestas, which also sponsors the current research project, and its people, particularly Rotor Systems UK Director Mr. Tomas Vronsky and former-employee Dr. Dongke Sun, who took good care of me when I visited the Vestas Isle of Wight site.

I would further like to thank Mr. Tomas Vronsky, Dr. Dongke Sun, my supervisors and Dr. T Glyn Thomas for their helpful comments during my transfer.

I am grateful to all the staff and friends in the Aerodynamics and Flight Mechanics Research Group and the graduate school office of the faculty of Engineering and the Environment.

Last but not least, without my beloved family, especially my wife Miao, my daughter Evelyn and my parents, it would be impossible for me to complete my current study.

Contents

List of Tables

List of Figures

Nomenclature

Roman Characters

a	A number from a uniform distribution, Section 3.4 only
a_m	Coefficient in the current FD scheme, with $m = 1, 2, 3$, Section 3.1.3
a_∞	The speed of sound of the freestream, Section 4
A_{ij}	The amplitude for the cosine part of an inflow wave-mode, or gust-mode
b	A number from a uniform distribution, Section 3.4 only
B_{ij}	The amplitude for the sine part of an inflow wave-mode, or gust-mode
c	The speed of sound
c	A number from a standard normal distribution, Section 3.4 only
C	The Coriolis parameter due to the Earth's rotation about its own axis, Section 3.4 only
C_L	The lift coefficient
$C_{L'}$	The perturbed lift coefficient
d	A number from a standard normal distribution, Section 3.4 only
dt_n	The time step size at the n^{th} time step
e	Energy per unit mass
$\mathbf{E}$	An inviscid flux term in N-S or Euler equations
E_{ij}	The energy content of the i^{th} component of the perturbed velocity of the j^{th} inflow wave-modo
$\mathbf{F}$	An inviscid flux term in N-S or Euler equations
$f(x)$	Target function, Section 1
f_i	Discretised target function, Section 1
$\bar{f}'_i$	Numerical approximation of the spatial derivative $\partial f(x)/\partial x$ at location i
$\widetilde{f}(k)$	Fourier transform of $f(x)$
f	Frequency, Section 3.4 onwards
$\mathbf{F}$	A non-linear vector function of the conservative variable vectors, Section 3.2
$\mathbf{G}$	An inviscid flux term in N-S or Euler equations
g_i	Extrapolation spline function for spatial boundary scheme
g'_i	The slope of the spline function
h_b	The height of the atmospheric boundary layer
i	Grid point number
I_1	The longitudinal turbulence intensity
I_2	The vertical turbulence intensity
J	Transformation Jacobian for the derivation of grid metrics
j	$\sqrt{-1}$

Nomenclature Continued

Roman Characters

k	Scalar wavenumber or wavenumber vector magnitude
$\bar{k}$	Numerical scalar wavenumber
k_{ij}	The i^{th} component of the non-dimensional wavenumber vector for the j^{th} gust-mode
k_{ijd}	The deterministic part of the wavenumber
k_{ijr}	The random part of the wavenumber
L	Characteristic convection term, Section 3.3 only
L	Aerofoil chord
L'	Non-dimensional lift computed from the code
L_1	Length scale of the longitudinal component of the perturbed flow
L_2	Length scale of the vertical component of the perturbed flow
${}^xL_u$	Integral length scale of the longitudinal component of the perturbed flow in the longitudinal direction
${}^xL_v$	Integral length scale of the vertical component of the perturbed flow in the longitudinal direction
M_∞	The freestream Mach number
N	The number of grid points, Section 3.1
n	An integer that denotes the solution at time level $t = (n+1)\Delta t$, Section 3.2 only
n	The number of grid points
p	Hydrostatic pressure, referred simply as pressure
p_m	Coefficient of the spline functions for extrapolation for boundary scheme, Section 3.1.3 only
p'	The unsteady pressure perturbation or fluctuation
p'_L	The loading noise
P_{RMS}	Root mean square perturbation pressure
$\mathbf{Q}$	3D conservative variables vector
q_m	Coefficient of the spline functions for extrapolation for boundary scheme, Section 3.1.3 only
r	Distance between an observer and a sound source
r_m	Coefficient of the spline functions for extrapolation for boundary scheme, Section 3.1.3 only
R	Radial distance from centre of the aerofoil
$\mathbf{R}$	The 3D characteristic variables vector
R_i	The i^{th} element of the 3D characteristic variables vector
S	The damping coefficient for the buffer zone damping function

Nomenclature Continued

Roman Characters

$\mathbf{S}_C$	Source term vector of the quasi-linearised Navier-Stokes or Euler equation, Section 3.3 only
S_i	The autospectral density function, Section 3.4 only
t_{sample}	The duration of time of a sample
t	Time
U	The velocity normal to the boundary in the generalised coordinates
$\overline{U}$	The mean wind speed, Section 3.4
u	x-velocity component
$\mathbf{u_{gust}}$	2D or 3D gust velocity vector
u^*	friction velocity, Section 3.4
u_{gust}	x-component of gust velocity
u_{st}	Grid translation velocity
u_i	The i^{th} component of the perturbed velocity vector
u_{ij}	The i^{th} component of the perturbed velocity vector for the j^{th} gust-mode
$\mathbf{u}^{(I)}$	The known portion of the unsteady compressible and vortical velocity field, Section 2.2 only
v	y-velocity component
v_{gust}	y-component of gust velocity
w	z-velocity component
W_{sp}	The width of the buffer zone
w_{gust}	z-component of gust velocity
x	First Cartesian coordinate
x	Longitudinal direction
bfx	Spatial vector of a general point
x_i	Spatial vector i^{th} element
x^*	Non-dimensional coordinate from the point of interest x_i
$x_1(\xi)$	A polynomial used for the algebraic grid generation method
$x_2(\xi)$	A polynomial used for the algebraic grid generation method
y	Second Cartesian coordinate
y	Vertical direction
y_h	The height above ground
y_i	The isotropic height
y_0	The surface roughness
z	Third Cartesian coordinate
z	Lateral direction

Nomenclature Continued

Greek Characters

α	Coefficient in the current FD scheme, Section 3.1 only
α	Angle of attack, or incidence angle
β	Coefficient in the current FD scheme
Δx	Grid point spacing
Δt	Time step size
ρ	Density
ρ_0	Steady uniform constant density
κ	Scaled wavenumber, Section 3.1 only
κ	Von Karman constant, Section 3.4 only
$\bar{\kappa}$	Scaled pseudo-wavenumber, Section 3.1 only
σ	Any of α, β and a_m for $m = 1, 2, 3$, Section 3.1.3 only
σ_i	The standard deviation about the mean wind speed, Section 3.4 only
ξ	First generalised coordinate
η	Second generalised coordinate
ζ	Third generalised coordinate
θ	A carefully chosen constant for the spatial scheme optimisation
θ	A number for the estimation of the longitudinal standard deviation, Section 3.4 only
τ	The retarded time
ϵ	Resolution error, Section 3.1.3
ϵ	2D gust velocity amplitude, 0.02, Section 3.1.4 onwards
Λ	Diagonal eigenvalues vector
Γ	The buffer zone damping function
ϕ	Perturbation potential, Section 2.2
ϕ	A number for the estimation of the longitudinal standard deviation, Section 3.4 only
Φ	Integrated error, Section 3.1
ϕ_m	Parameter for boundary scheme optimisation
ϕ	The perturbation potential, Section 2.2 only
Ω	The angular velocity of the Earth's rotation, Section 3.4 only
λ	The latitude, Section 3.4 only
λ_g	The longitudinal wavelength of the incident gust

Nomenclature Continued

superscript

a	End of the first stage of the Runge-Kutta scheme, Chapter 3.2
b	End of the second stage of the Runge-Kutta scheme, Chapter 3.2
c	End of the third stage of the Runge-Kutta scheme, Chapter 3.2

subscript

ret	retarded time
0	Mean value
∞	Freestream value

Abbreviations

APE	Acoustic perturbation equations
BC	Boundary conditions
BEM	Blade element momentum
CAA	Computational aeroacoustics
CFD	Computational fluid dynamics
CFL	Courant Friedrichs Lewy
DES	Detached eddy simulation
DF	Digital filter
DNS	Direct numerical simulation
DRP	Dispersion-relation-preserving
FW-H	Ffowcs-Williams Hawkings
FD	Finite difference
FE	Finite element methods
FV	Finite volume method
FRPM	Fast random particle-mesh
HAWT	Horizontal axis wind turbine
LEE	Linearised Euler equations
LES	Large eddy simulation
L.H.S.	Light hand side
LEA	Wavy leading-edge peak-to-peak amplitude
LEW	Wavy leading edge wavelength
MPI	Message passing interface
N-S	Navier-Stokes
ODE	Ordinary differential equation
PDE	Partial differential equation

Nomenclature Continued

Abbreviations

RANS	Reynolds Averaged Navier-Stokes
Re	Reynolds number
R.H.S.	Right hand side
R-K	Runge-Kutta
RPM	Random particle-mesh
rpm	Revolutions per minute
SPL	Sound pressure level

1 Introduction

Aerodynamic sound is generated when a solid surface, such as a wind turbine blade, is situated in an incident flow which is unsteady and non-uniform. Noise generated in this manner will be referred to as aerofoil-gust interaction (AGI) noise herein. The generation of AGI noise is mainly an inviscid phenomenon, where pressure fluctuations are generated to balance the momentum fluctuations that occur due to the distortion of the velocity disturbance, or gust, by the potential flow near the obstacle. AGI noise is an important wind turbine noise source since wind turbine blades are constantly subjected to atmospheric wind gust and turbulent wake from other wind turbines in a wind farm. The other important wind turbine noise is aerofoil self-noise, which is produced in the wind turbine blade surface boundary layer and in the wake region aft of the blade trailing edges. Aerofoil self-noise has been studied extensively [1–7]. From these studies, the dependence of various types of aerofoil self-noise on parameters such as flow speed, angle of attack and aerofoil shape was characterised. In contrast, AGI noise has received much less attention. Hence AGI noise is the focus of the current research.

The largest type of wind turbine has a hub height and a rotor *diameter* of around 120m and a maximum generated power of 5MW [8]. Wind turbine noise is one of the major obstacles to the more widespread use of wind energy. In a Dutch survey regarding the perception of wind farm acoustic and visual impacts by a selected group of nearby residents, it was found that noise was the most annoying aspect of wind turbines [9]. The survey also found that the most common description of wind turbine noise by the residents were swishing or lashing [9]. Wind turbine noise can be divided into two main types: mechanical and aerodynamic noise. Mechanical noise originates from the relative motion of the mechanical components and the dynamic responses among them; aerodynamic noise comes from the interaction of the wind turbine structures with the flow around them. AGI noise and aerofoil self-noise are examples of aerodynamic noise. Nowadays, mechanical noise can be reduced efficiently by using better gearbox and generator designs. Hence aerodynamic noise is the dominant noise emitted from a modern wind turbine. Some types of aerodynamic noise can be reduced or avoided without any special design of the wind turbine components. For example, by using upwind machines, some low frequency noise and impulsive noise can be avoided. Also, since the blade tips have the highest translational velocity due to rotation, noise can be reduced by lowering the tip speed ratios. Variable speed operation allows lower rotational speed in low winds, which leads to much lower noise levels in low winds than comparable constant speed turbines. Pitch control of the rotor blades can also reduce the noise level through the reduction of the local angle of attack and blade loading [6]. However, noise reduction by these operational means are limited. For instance, the lower the rotor rotational speed, the lower the power produced.

To further reduce wind turbine noise without sacrificing the power output, the aerodynamic shapes of the various wind turbine components have to be refined. The aim of the current study is to investigate the effect of aerofoil leading-edge geometries on AGI noise. It is well known that owl's silent flight is attributed to their tiny saw-tooth-shaped serrations on the leading edges of the main flight feathers [10, 11]. Soderman [10] conducted experiments using rotor blades with tiny saw-tooth serrations (0.1 to 0.5cm in height) attached to the lower surface of the leading edge. He found that

the serrated leading edge was effective in reducing the high-frequency noise at low tip speeds (between 48 and 135m/s). However, the aerodynamic effect was highly sensitive to the attachment location of the serrations. Small deviation from the ideal location could lead to an overall degradation in aerodynamic performance. A more recent experimental study on owl wings by Ito [11] reported that the post-stall aerodynamic benefit brought about by serrated leading edges was only observed at a low Reynolds number of 2.1×10^4.

Another type of leading-edge geometry can be found on the pectoral flippers of humpback whales, which have tubercles. Several studies showed that leading-edge tubercles may lead to a more gradual stall and better post-stall performance than straight leading edges at the expense of marginal reduction in pre-stall performance [12–20]. The aerodynamic benefits of leading-edge tubercles have been observed over a wide range of Reynolds numbers. While most of the work has focused on the aerodynamic aspects, Hansen et al. [21] recently studied experimentally the aeroacoustic effect (tonal noise) and found that leading-edge tubercles, particularly those with the smallest wavelength and the largest amplitude tested, reduced the tonal noise significantly.

In light of these studies, the current study investigates a spanwise sinusoidal profile of leading edges, which is referred to as *wavy leading edges* herein. Unlike the aforementioned serrations and tubercles, the proposed wavy leading edges preserve the same aerofoil section and planform area with those of the original straight leading-edge counterparts. It was recently shown that wavy leading edges produce similar aerodynamic benefits that were obtained by using the tubercles [20]. It is envisaged that wavy leading edges may also be beneficial in reducing AGI noise in the presence of incident gust, which has not been extensively investigated to this date. A contemporary study by Clair et al. [22] showed that wavy leading edges could reduce AGI noise. The current study aims to deliver a fundamental understanding of the effects of wavy leading edges on AGI noise by considering velocity disturbances predominantly in streamwise and vertical directions using high-fidelity numerical simulations.

Wind turbine noise has been investigated theoretically, experimentally and numerically. A popular theoretical approach is acoustic analogy, especially in the form of the Ffowcs-Williams Hawkings (FW-H) equation, which was derived from the continuity and the Navier-Stokes (N-S) equations. FW-H equation has been used for the prediction of rotor noise in both time and frequency domains [2]. Another theoretical approach particularly for the study of AGI noise was developed by Goldstein [23] utilizing the rapid distortion theory. By assuming the flow to be inviscid and non-heat-conducting, he linearised the governing equations and rewrote them into a linear inhomogeneous equation in terms of a perturbation potential. For a compressible flow, the inhomogeneous wave equation derived by Goldstein has variable coefficients and functions within the source term and boundary conditions. Hence the equation has to be solved numerically. Myers and Kerschen [24, 25] developed approximate close-form expressions of the equation. They considered a two dimensional (2D) irrotational compressible mean flow, which was assumed to be a small perturbation to a uniform flow. Superposition of small-amplitude harmonic components was used to

represent the upstream divergence-free vortical velocity. They further assumed small angle of attack and high frequency of converted disturbances. With these assumptions, a simplified form of the Goldstein's equation was derived. Flat plate aerofoils with and without camber have been analysed by Myers and Kerschen [24, 25]. The theoretical models by Goldstein and Myers and Kerschen are useful for the study of AGI noise. However, they are restricted to 2D problems.

Based on the results of some experimental and theoretical studies, some semi-empirical models of AGI noise have been developed. One of these semi-empirical models was proposed by Lowson [26]. Lowson's AGI noise model was based on the theoretical model by Amiet [27], who considered the response of an infinitely thin flat plate with high aspect ratio to incident gusts. The various empirical parameters were chosen to reflect the test conditions of a certain set of experimental data. The major advantages of semi-empirical models are that they are computationally inexpensive, easy to use, and fast to return results. However, the validity of using these models in various flow conditions is questionable since they are restricted by many constraints.

Computational aeroacoustics (CAA) has made significant advancement in recent years. However, the computational cost needed to numerically simulate the whole range of wind turbine noise sources accurately and in reasonable time remains prohibitively high. Hence, it is sensible to study each type of noise generation mechanism separately. Aerofoil self-noise, which originates within the boundary layer and the wake regions, is avoided in the current simulations by using the Euler equations. There exists some fundamental work done on AGI noise based on CAA approaches and they are mostly limited in 2D domains [28–30]. Recent three-dimensional (3D) simulations were performed by Atassi et al. [31] and Hixon et al. [32]. The current research employs an accurate and efficient high-order method [33] for the direct computation of AGI noise in 3D domain. The efficiency and accuracy of the current numerical methodology has been demonstrated in a previous study [33] concerning 2D problems. A unique sponge technique, which utilises a sponge zone around the physical computational domain, is used to embed the incident vortical gust. Together with generalised characteristic non-reflecting boundary conditions (BC) [34, 35], the current boundary treatment technique has been shown to produce minimal reflections of the out-going quasi-linear characteristic waves [33]. As a result, the domain size required by the current methodology is small and high computational efficiency can be achieved. High-order numerical discretisations are used. Fourth-order optimised compact finite difference (FD) schemes [36, 37], in conjunction with sixth-order compact filters [37, 38], are used for the spatial discretisation. For time integration, a standard fourth-order four-stage Runge-Kutta (R-K) time marching scheme is used to advance the solution.

The current study considers an inviscid, non-heat-conducting and compressible incident flow. The upstream velocity consists of a uniform portion and a small-amplitude unsteady motion superposed on it. The nature of such flow is well understood [23]. This type of flow can be decomposed into the sum of three modes of motion. First, the vortical mode, often referred to as *gust*, is a velocity disturbance. The incident vortical mode is purely convected, or frozen in the flow, divergence-free

and produce no pressure nor any other thermodynamic property fluctuation. The second mode is the acoustic mode. It is an irrotational disturbance that produces no entropy fluctuations, and is directly related to the pressure fluctuation. The third mode is fluctuations in entropy, that are decoupled from the velocity and pressure fluctuations, but produce density fluctuations, and is also purely convected. Each of these modes of motion is a solution to the governing equations, which are the Euler equations in the current research, and hence can be imposed independently of one another. The incident flow employed in the current study is purely vortical and divergence-free. So there is no incident acoustic field.

In summary, the principal objectives of the current research are

- to investigate the effects of wavy leading edges, particularly their peak-to-peak amplitude and wavelength, on AGI noise;
- to study the effects of angle of attack and aerofoil thickness on AGI noise and the noise-reducing capability of wavy leading edges;
- to explore the effects of multiple constituent gust frequency components on AGI noise and the noise-reducing capability of wavy leading edges;
- to validate the current numerical methodology;
- to generate a high-quality grid which encompasses half a low aspect ratio wing with a tip;
- to demonstrate the capability of the current methodology for applications with more complicated incident gusts and grid structure.

The structure of the current thesis is as follows: in Chapter 2, wind turbine aeroacoustic researches, including experimental, theoretical and numerical studies, and the aerodynamic and aeroacoustic researches related to wavy leading edges will be reviewed. Then, the details of the current numerical methodology will be explained in Chapter 3. After that, in Chapter 4, four validation studies will be shown. Then the current method and code can be used, with confidence, for the investigation of the effects of wavy leading edges on AGI noise in Chapter 5. All the simulations in this chapter employ 3D aerofoils. In Chapter 6, the aeroacoustic effects of wavy leading edges on a low aspect ratio wing with tips will be studied. Finally, the conclusions of the current research will be summarised in Chapter 7.

2 Literature Review

Wind energy has become more widespread and important in recent years. As a result, wind turbine aeroacoustic research has received more attention. However, wind turbine AGI noise remains a largely untouched research topic. This chapter presents a review of the recent wind turbine aeroacoustic research activities. First, some experimental and theoretical studies will be reviewed in Sections 2.1 and 2.2 respectively. Then, a brief review of some wind turbine aeroacoustic prediction models developed from the results of some experimental and theoretical studies will be made in Section 2.3. After that, some CAA methodologies for wind turbine aeroacoustic research will be discussed in Section 2.4, which also includes a brief summary of the current CAA methodology used in this study. In Sections 2.5 and 2.6, detailed reviews of the experimental and numerical studies on the aerodynamic effects of leading-edge modifications, such as leading-edge tubercles and wavy leading edges, will be given respectively. Finally in Section 2.7, the published works to-date on the aeroacoustic effects of leading-edge modifications will be reviewed.

2.1 Experimental Wind Turbine Aeroacoustic Studies

Experimental wind turbine aeroacoustic studies include field and wind tunnel experiments. Basic ideas regarding the noise level and some features of the noise, such as the frequency range and dominant frequencies, can be obtained readily. Qualitative comparisons can also be made without many difficulties. However, experimental measurements can only provide a general picture, for example the overall sound level and the total sound spectra, rather than the specific data regarding a particular source of noise. The relative importance of different noise generation mechanisms is determined by predictions, based on various assumptions and judgements depending on the experimental conditions, and is different from one study to another. Also, field measurements are subjected to variable weather conditions, which can significantly change the relative importance of different sources of noise. Hence it is not easy to judge the effectiveness of a new blade design in suppressing a particular source of noise experimentally. In this section, some experimental studies of wind turbine aeroacoustics will be discussed.

One of the most important aspects of wind turbine blade design is the aerofoil shape. Migliore and Oerlemans [39] conducted a wind tunnel aeroacoustic experiment for aerofoils used on small wind turbines, which usually have a rated power of less than 20kW and operate at a $Re = 10^6$ or less. The aim of their study was to obtain a relative comparison of the prominent noise sources for the six aerofoils tested. The measured data were used to build up an aerofoil aeroacoustic performance database, which would be useful for wind turbine design and computational code validation. A small open-circuit wind tunnel with a semi-open test section was used for the experiment. A microphone array mounted in an open grid and placed outside the tunnel flow to one side of the test section was used to record the noise. The aerofoil models were short-span wings mounted between endplates. Hence extraneous noise could be generated by the interaction between the endplate boundary layer and the aerofoil model-endplate juncture. The incident turbulence was generated by a turbulence

grid mesh installed in the nozzle of the wind tunnel. The grid also generated background noise. The method used to distinguish the extraneous noise from the noise generated by the aerofoils were discussed by Migliore and Oerlemans [39].

The experimental results of Migliore and Oerlemans showed that when the turbulence grid was installed, AGI noise became dominant for all the aerofoils tested. The source of AGI noise was found to be at the leading edge. It was also found that the tripped and un-tripped aerofoils produced identical results when the turbulence grid was installed. Migliore and Oerlemans warned that, since the level of turbulence used in their wind tunnel experiment was much greater than what wind turbines would encounter in the atmosphere at typical rotor speed, one should not conclude that the presence of atmospheric turbulence would lead to AGI noise being totally dominant. They suggested that more research was needed for wind turbine AGI noise. Hence, the results of experimental studies like that by Migliore and Oerlemans [39] should only be used as a rough estimate and guildline in determining wind turbine noise. Nevertheless, by comparing the six aerofoils tested, Migliore and Oerlemans suggested that the thinner the aerofoil, the higher the AGI noise [39]. This trend was also suggested by other studies [6, 40].

To understand the mechanisms of wind turbine noise, an idea of the approximate location and nature of the noise sources is required. This was the aim of the study by Oerlemans et al. [5]. The goal of their study was to characterise the noise sources on a three-bladed GAMESA G58 wind turbine with a rotor diameter of 58m and a tower height of 53.5m. Field measurements on a wind farm edge were taken by a large horizontal microphone array positioned one rotor diameter upwind of the rotor. Their results showed that practically all downward radiated noise was produced during the downward movement of the blades. Additionally the blade noise was found to be significantly higher than the hub noise. The difference between these two sources of noise increased with increasing wind speed. An effort was made to verify whether trailing-edge noise was dominant. Oerlemans et al. [5] made use of a directivity function, which incorporated a convective amplification factor for trailing-edge noise. The directivity function was derived analytically for semi-infinite flat plate and was found to be valid for finite aerofoils under some conditions. However, experimental validation of the amplification factor was very limited. By assuming the source to be located at the trailing edge of the blade at a radius of 25m, which was the location observed from the measured results, and using the typical number of revolutions per minute (rpm) and wind speed values in the experiment, the directivity function was calculated and plotted as a function of rotor azimuth. The plot showed good qualitative agreement with the experimental results. To further show the dominance of trailing-edge noise in the field measurements, the measured and normalised noise spectra were compared. For the normalised spectra, the reference sound pressure level (SPL) was subtracted from the measured SPL. In the derivation of the reference SPL, the common approximation of the sound power being in proportion to the 5^{th} power of the flow velocity for trailing-edge noise was used. The flow velocity was assumed to be the undisturbed flow speed perceived by the blade at a radius of 25m. The normalised SPL was plotted as a function of the Strouhal number, which was derived using the same flow velocity. By normalizing in this way, the scatter in the spectral data was reduced by roughly 50%. The measured

SPL was simply plotted against the frequency of the measured spectra. Oerlemans et al. [5] argued that these results were convincing evidence that broadband trailing-edge noise was dominant in this specific study. It is important to note that the field measurements were taken in calm atmospheric conditions. Hence the wind gust effect was small and it is not surprising that AGI noise was not dominant.

Similar techniques can be used to assess whether AGI noise is dominant in other studies, even numerical ones. For example, the directivity function for AGI noise [5] can be used instead; the numerical SPL can be used for a spectral analysis similar to the one mentioned above. The 6^{th} power of the flow velocity, which relates to AGI noise [5, 39], can be used to derive the reference SPL.

Experiments can also be used to verify the overall noise-reduction capability of new rotor blades. An acoustic field measurement on a three-bladed wind turbine with a diameter of 94m and tower height of 100m was conducted by Oerlemans et al. [6] The turbine was specially modified, with one standard blade used as the baseline for comparisons, one blade with an optimised aerofoil shape for the outer 30% spanwise section, and one standard blade with serrations mounted to the outer 12.5m section along the trailing edge. The length of the serrations was about 20% of the local chord. A horizontal microphone array situated one rotor diameter from the turbine was used for taking the acoustic measurements.

From the upwind measurements, average noise reductions of 0.5dB and 3.2dB were observed for the blades with optimised aerofoil and serrated trailing edge respectively. Power and load measurements were also taken, and it was found that the aerodynamic performance of the modified blades were similar to the baseline blade. This study by Oerlemans et al. [6] is a good example of a potential noise-reducing blade design that does not compromise wind turbine power production capability. However, the measurements used for the analysis were chosen such that any large atmospheric gust was avoided. Hence the effect of AGI noise was small compared to the trailing-edge noise and tip noise in their study.

Many of the field studies of wind turbine noise are performed when large atmospheric gust is absent. Also, it is not easy to isolate the effect of AGI noise experimentally. Hence there is a clear need for more specific researches on AGI noise before any conclusion about its relative importance can be drawn. In the next section, a review of the development and applications of theoretical aeroacoustics for wind turbines is given.

2.2 Theoretical Wind Turbine Aeroacoustic Studies

The pioneer in theoretical aeroacoustics was Lighthill [41], who proposed an acoustic analogy in the 1950s. The analogy relates the full non-linear fluid flow theory to the linear theory of classical wave acoustics. It became widely used, especially for jet noise analysis [42]. Curle [43] extended the theory to include the influence of static boundaries. Then, the Ffowcs-Williams Hawkings (FW-H)

equation [44], which was the most general form of the original Lighthill's theory, was derived to include the effect of a moving solid object in the fluid. These analogies are all in the form of an inhomogeneous wave equation. Once the flow parameters are estimated, the source terms can be computed and the equation can be integrated to give a prediction of the sound field.

The FW-H equation can be derived from the continuity and the Navier-Stokes (N-S) equations. A control surface is defined. Inside this surface, the flow parameters have the same fluid states as the undisturbed medium. Hence such surface represents a discontinuity for the flow parameters. The aim is to compute the sound field in the exterior of the control surface. There are three source terms in the FW-H equation, of which two exist on the control surface only. One of these surface sources is the monopole source. Depending on the location of the control surface, the monopole source either represents the noise generated by the unsteady mass flux through the control surface or by the displacement of fluid as the body passes. This source is usually known as the thickness source. The other surface source is the dipole source, which represents the noise generated by the unsteady force on the fluid on the control surface location and is commonly referred to as the loading noise. The remaining source is the quadrupole noise source, which is a volume source and represents the noise generated by the flow alone outside the control surface. The noise sources due to shock waves, wakes and other discontinuities can be derived from this quadrupole source term. By analysing the quadrupole source term of Lighthill, it was shown by Farassat [45] that the jump across a shock produced monopole and dipole sources on the shock surface. He also stated that ideally, the control surface should be located where the contribution of the quadrupole source outside the surface to the noise was small. Depending on the aeroacoustic problem considered, such an ideal location might not be possible. For example, in high-speed helicopter rotor noise prediction, the accuracy of the computational fluid dynamics (CFD) data at the ideal surface location might not be good enough and renders this approach impossible. Farassat further commented that the quadrupole source strength computation had high requirement on storage space and computational time. Approximate solutions of this noise source have been derived for use in helicopter rotor design [45]. Due to the complexity of volume integral calculation, it is common to neglect the volume distribution of quadrupole sources in numerical implementations of the FW-H equation.

The control surface can coincide with the blade surface, this approach is referred to as the solid FW-H formulation herein. Alternatively, the control surface can be an imaginary surface in the flow field that contains all the desired physical noise sources [2,45]. Such approach is commonly known as the permeable FW-H formulation. An advantage of the permeable formulation stems from the fact that any physical acoustic sources enclosed within the $f = 0$ control surface only contribute through the surface source terms. Therefore, if all the physical sources are enclosed within the permeable control surface, the complicated and computationally expensive quadrupole source outside the surface becomes negligible, and can be neglected without any loss of accuracy. Moreover, compared to volume integration, much less flow-field data is required for surface integration. Regardless of the type of formulation, the source strength is determined by the outputs of a coupled flow solver, which can be anything from inviscid to direct numerical simulation (DNS) solvers. Once the source strength

is determined, the solution of the FW-H equation can be found by using the free space Green's function.

The FW-H equation is appropriate for the prediction of rotating blade noise in either the time or frequency domain [2]. Fillos et al. [46] investigated the broadband noise emitted from a three-bladed downwind horizontal axis wind turbine ($HAWT$) rotor with a radius of about 5m in the time domain using a coupled method. The aeroacoustic modelling was based on the FW-H equation, and the quadrupole source term was neglected. The control surface was set to coincide with the rotor blades, and the inflow was assumed to be uniform; the aerodynamic part was based on a three dimensional low-order panel method. The effect of compressibility was taken into account by correction factors. The panel method was also coupled with an integral boundary layer model to account for viscous effects. 40 and 45 panels were used in the blade chordwise and spanwise direction respectively. A helical shape panel grid was used for the wake region. The low-order panel method, albeit with some corrections, is a crude way to model the complicated flow around a wind turbine rotor. Together with the various other assumptions made, the accuracy of such methodology is low, and the results can only be used as a crude estimation of wind turbine noise.

A more advanced compressible time-accurate numerical flow simulation can be coupled directly to a FW-H noise prediction code. An example was the study of wind turbine blade tip noise by Fleig et al. [3] and Arakawa et al. [4], who were in the same group of researchers. Two different blade tips: the original *WINDMELIII* wind turbine blade tip and the so-called *ogee* tip, were compared. These authors used compressible LES in the near-field to compute the flow and the noise directly. The permeable FW-H formulation by Brentner and Farassat was used to compute the noise in the far-field region, which stretched to 200 chord-lengths away from the blade. The fictitious permeable control surface, which consisted of actual grid points used by the LES, was located one reference chord-length away from the blade and encircling the blade. The near-field time-accurate pressure, density and velocity components computed by the LES were fed into the FW-H equation for integration on the control surface. The intense quadrupole source in the near-field due to the strong velocity gradient and non-linearity close to the blade was taken into account by the LES. Moreover, the surface source terms on the control surface accounted for the sound generated in the region between the solid surface and the control surface [4]. Hence the quadrupole volume source outside the control surface could be neglected without sacrificing accuracy. Furthermore, with the control surface placed some distance away from the blade, the mean flow could be considered reasonably uniform [4]. Hence, this permeable FW-H formulation could provide accurate far-field noise predictions. The other part of their research and the results will be discussed later in Section 2.4.

Another recent study of a coupled FW-H wind turbine noise prediction code was conducted by Tadamasa and Zangeneh [47]. The commercial CFD package *ANSYS CFX 11.0* was used for the flow simulation, which was based on RANS, to compute the FW-H inputs in the near-field. This approach was less accurate than the LES used by Fleig et al. [3] and Arakawa et al. [4], but the computational cost was smaller. Two FW-H codes, one based on the solid FW-H formulation and the other on the permeable FW-H formulation, were tested. The computed results were

validated using the measured acoustic data of a scaled helicopter rotor model in hover mode with two different tip Mach numbers: 0.8 and 0.85; and an aircraft propeller with a tip Mach number of 0.87. The helicopter rotor and the aircraft propeller were both two-bladed. Hence only one blade was simulated. For both validations, the control surface for the permeable FW-H formulation encircled the whole span of the blade, extended by certain spanwise distance from the blade tip and had the same cross-sectional shapes, but with twice the chord-length, as the blade along the span. The permeable FW-H code of Tadamasa and Zangeneh was able to predict the negative peaks of the acoustic pressure time series results well for both validation cases. However, differences were observed for the positive part of the series, particularly for the aircraft propeller case. The authors attributed this to the high rotational speed of the propeller and the location of the control surface, which was only able to encircle part of the volume distribution of quadrupole source at high Mach number [47]. The inability of the RANS flow solver to resolve the separated flow region on parts of the blade was also a factor. Tadamasa and Zangeneh then used their FW-H codes to analyse the composition of the noise emitted from the two-bladed NREL Phase VI wind turbine at various operating conditions. They found that the loading noise was the major noise source at lower rotational speeds, while at higher rotational speeds the thickness noise became dominant [47].

In general, accurate aeroacoustic predictions by FW-H formulations are possible provided that the unsteady blade loading is accurately predicted by the flow solver [2]. Alternatively, measured blade pressure data from experiment can be used as the input for the FW-H equation for noise prediction. The FW-H equation has been used extensively to predict rotorcraft noise.

The acoustic analogy is not the only theoretical approach that can be used to study wind turbine noise. Goldstein developed a theoretical approach utilizing the rapid distortion theory. His study of the unsteady inviscid compressible and vortical flow round obstacles shows insight into the mechanism of AGI noise generation [23]. Goldstein extended the generalised rapid distortion theory of turbulence by considering the most general type of incident disturbance that did not include incident acoustic field. Such incident disturbance consisted of both entropic and vortical modes. By assuming the flow to be inviscid and non-heat-conducting, he linearised the governing equations and rewrote them into a linear inhomogeneous equation in terms of a perturbation potential ϕ, i.e.

$$\frac{D_0}{Dt}\left(\frac{1}{c_0^2}\frac{D_0\phi}{Dt}\right) - \frac{1}{\rho_0}\nabla\cdot(\rho_0\nabla\phi) = \frac{1}{\rho_0}\nabla\cdot\rho\mathbf{u}^{(I)}, \tag{1}$$

where suffix 0 denotes background mean potential flow properties; D_0/Dt is the convective derivative based on the mean flow velocity; c is the speed of sound; ρ is the density; and $\mathbf{u}^{(I)} = \mathbf{u}^{(I)}(\mathbf{x}, t)$ is the known portion of the unsteady compressible and vortical velocity field at any point $\mathbf{x}$. At upstream infinity, $\mathbf{u}^{(I)}$ approaches the imposed vortical velocity field $\mathbf{u}_\infty$. Hence, ϕ, $\mathbf{u}^{(I)}$ and $\mathbf{u}$ are related by

$$\mathbf{u} = \nabla\phi + \mathbf{u}^{(I)}.$$

The L.H.S. of equation (1) is the wave equation for a slightly unsteady potential flow; while the strength of the dipole source term on the R.H.S. is effectively the known incident velocity field. The

perturbation potential is related directly to pressure fluctuations by

$$\frac{p'}{\rho_0} = -\frac{D_0\phi}{Dt}.$$

Since the incident velocity disturbance is divergence-free, the source term of the inhomogeneous wave equation goes to zero at upstream infinity. Hence the potential becomes zero and no pressure fluctuation is produced. Near the obstacle, the mean potential flow is able to distort the incident velocity disturbance field such that the initial divergence-free condition is destroyed locally. Therefore, the source term of the inhomogeneous wave equation is non-zero. As a consequence, the perturbation potential becomes non-zero and hence pressure fluctuations are produced near the obstacle. Physically, pressure fluctuations are generated to balance the momentum fluctuations that occur due to the distortion of the velocity disturbance, or gust, by the potential flow near the obstacle. Hence AGI noise can be generated even the flow is inviscid.

The theoretical approach of Goldstein is applicable to both thin and blunt bodies. However, when dealing with thin bodies, one has to assume that either the freestream Mach number is sufficiently large or that the characteristic frequency of the imposed unsteady motion is large.

Myers and Kerschen [24, 25] developed a theoretical model for the sound generated when a convected gust encounters an aerofoil. Their theory is based on that developed by Goldstein. For a compressible flow, the inhomogeneous wave equation derived by Goldstein has variable coefficients as well as functions within the source term and boundary conditions. Hence the equation has to be solved numerically. Myers and Kerschen developed approximate close-form expressions of the equation. They considered a two dimensional irrotational compressible mean flow, which was assumed to be a small perturbation to a uniform flow. Also, since the mean flow was uniform far upstream, the upstream unsteady disturbances satisfied linear equations whose coefficients were constant. Hence superposition of harmonic components could be used to represent the upstream disturbances, which consisted of small amplitude vortical and entropic disturbances. The vortical velocity at far upstream was divergence-free. Myers and Kerschen further assumed that the frequency of the convected disturbance was high, i.e. its wavelength was short compared to the aerofoil chord, and the angle of attack was small. Flat plate aerofoils with and without camber have been analysed by Myers and Kerschen [24, 25]. With these assumptions, a simplified form of the Goldstein's inhomogeneous wave equation was derived. Perturbation terms of small magnitude were neglected and asymptotic solutions in each of the four asymptotic regions around the aerofoil were derived. Far-field pressure directivity patterns and total acoustic power were computed for a few combinations of mean flow and disturbance parameters. For a flat plate without camber at a small angle of attack, Myers and Kerschen found that at a higher gust frequency, a larger increase in the acoustic pressure level could be caused by the same increase in angle of attack compared to a lower gust frequency. They suggested that the effect of angle of attack scaled with $O(\alpha k^{1/2})$, where α is the angle of attack and k is the dimensionless gust frequency. They concluded that the radiated sound field for high frequency gust interaction is quite sensitive to changes in α.

Myers and Kerschen further showed that for a low Mach number, in the local leading-edge region, identical equations governing certain components of the pressure fields could be derived using the acoustic analogy and the rapid distortion approach. The major difference between the acoustic analogy and the rapid distortion approach was in the treatment of the variable flow properties. In the acoustic analogy, the quadrupole source term on the R.H.S. of the inhomogeneous wave equation was expressed in terms of the variable flow properties, whose values were not known and needed to be determined by heuristic models; while for the rapid distortion approach, the source term on the R.H.S. was explicitly written in terms of the imposed upstream convected disturbance and mean flow field quantities, which did not require source modelling. However, Goldstein's rapid distortion approach is only applicable to the prediction of noise generated by the interaction of unsteady convected disturbances with steady potential flows. Acoustic analogy, on the other hand, is a much more general formulation [24]. The theoretical results of AGI noise by Myers and Kerschen will be used to validate the 2D results of the current code later in Chapter 4.

2.3 Wind Turbine Noise Prediction Models

Theoretical and experimental studies of wind turbine aeroacoustics can be used to develop noise prediction models, which are inexpensive computationally and can give wind turbine designers a rough idea of the relative importance of the different noise sources quickly. These models can be divided into three categories according to their accuracy and range of applicability [48]:

Category 1 Models
They are the simplest models based on simple algebraic relations, also the least accurate and have the narrowest range of applications. They relate the emitted sound power level to the main geometrical and operational parameters of the wind turbines. The only advantage is that these models are very fast to run. However, this advantage is more than offset by their poor accuracy and applicability, and they have been supplanted by the category 2 models.

Category 2 Models
These are semi-empirical models deduced from the empirical relations observed in theoretical and experimental aeroacoustic studies. They are more complicated than category 1 models. They predict the emitted sound pressure level as well as the sound spectra. Over the years, there are many different semi-empirical models developed for each sound generation mechanism. Depending on the degree of empiricism as well as the deviation from the conditions of the field measurements used for their validations, these models provide predictions of various accuracies.

An early example of the use of semi-empirical models for wind turbine noise prediction was that by Lowson [26] mentioned in the introduction. Dassen et al. [49] employed a somewhat more advanced AGI noise model, which took the aerofoil thickness into account, in their AGI noise and aerofoil trailing-edge self-noise prediction code. Later, Moriarty and Migliore [50] used Lowson's AGI

noise model and five other self-noise semi-empirical models in their wind turbine noise prediction code. They assumed that the overall noise spectra emitted from the rotor could be obtained by superposing the results of each of the models. Correction factors, which took into account the convective amplification of non-stationary sources and Doppler effects relative to the observer, were also incorporated into the models. The semi-empirical code was then validated by comparing with measurements from 2D aerofoil and full-scale wind turbine tests. Results from the validations were mixed. There were many reasons for the observed discrepancies. For instance, only six semi-empirical noise models were used. Hence some noise-producing mechanisms were neglected. Also, each of these models was based on measurements for a NACA 0012 aerofoil only. Moreover, the flow over rotating blades could have a significant spanwise component, which undermined the local 2D flow assumption. Furthermore, the unsteadiness in real turbulent flow was not taken into account. This prediction code by Moriarty and Migliore has been continuously updated over the past few years. Moriarty et al. [40] simplified the AGI noise model so that it could be run more quickly on a normal personal computer (PC). The simplified model was shown to produce similar SPL to the original model. Leloudas et al. [51] used similar models to the study by Moriarty and Migliore [50] in their semi-empirical wind turbine noise prediction code. Oerlemans and Schepers [7] used a semi-empirical method for the prediction of the trailing-edge noise emitted from modern large wind turbines. According to their method, the blades were first divided into radial sections. Then they estimated the sectional aerodynamics using a model, which was based on the blade element momentum (BEM) theory and the measured 2D aerofoil characteristics provided by the turbine manufacturer. The only inputs needed were the blade geometry parameters and the turbine operating conditions. The AGI noise was assumed to be negligible based on some previous studies [5, 6]. Then the trailing-edge source strength was predicted by using the semi-empirical model by Brooks et al. [52] and the estimated sectional aerodynamics. General good agreement was found between the predicted and the measured field results.

These codes based on semi-empirical models are easy to use and can give quick predictions of noise level. Hence they are very useful design tools for wind turbine designers. However, their accuracy reduces as the flow environment deviates from their designed conditions. It is also difficult to prove the effectiveness of new blade geometric designs in suppressing noise by using these codes. Therefore, if one wants to reduce the AGI noise by introducing changes to the blade geometry, more sophisticated models are required. And this is only possible through the appropriate simulation of the physics of the flow, which is the aim of the category 3 models.

Category 3 Models

These are the most accurate and most computationally expensive models in the three categories. They take into account the complex 3D and time-dependent distribution of the acoustic sources [48]. These models are based on the fact that at *low* Mach number, the amplitude of the acoustic fluctuation is several order smaller than that of the hydrodynamic fluctuation [48]. Hence the problem can be split into the flow and the acoustic parts due to this scale difference. The set of equations for the flow part only needs to be solved in the part of the domain where significant noise

is generated. From the flow solutions, the acoustic source terms can be computed. Then the set of acoustic equations can be solved. These models are commonly referred to as the hybrid methods. In essence, the Lighthill analogy and the FW-H equation can be classified as hybrid methods. In the case of the FW-H equation, once the acoustic source terms are computed from the flow solutions, the inhomogeneous wave equation can be integrated analytically using a Green's function. An example of this type of hybrid method is the coupled method by Fillos et al. [46] mentioned in the previous section. In many hybrid methods, the acoustic part is solved numerically. These methods can also be classified as CAA methods. Hence they will be discussed in the next section, which gives a review of the development and applications of CAA methods for wind turbine aeroacoustics.

2.4 Wind Turbine Computational Aeroacoustics

The compressible N-S equations describe both sound generation and propagation at all flow conditions. Hence, it is natural to try to devise numerical strategies to solve them to compute the entire sound field. Due to the nature of sound generation and propagation, ordinary CFD strategies are not suitable for CAA applications. As a sound wave propagates, it disturbs the fluid from its mean state. These disturbances in pressure, density and velocity are nearly always very small compared to the mean state [44]. For example, the threshold of pain for human ear is about 130 - 140dB, which corresponds to a pressure perturbation of approximately 10^{-3} of the ambient atmospheric pressure. Since the flow perturbations involved in acoustic waves are always very small, their products are negligible. Hence the radiated sound field is typically linear [44, 53]. However, the flows that generate sound are usually non-linear, unsteady and turbulent. The sound radiation from these flows is usually weak, except for high Mach number flows. But the presence of solid objects, like a wind turbine, in these flows can result in a transfer of disturbance energy from the otherwise non-radiating convected modes to those that radiate [44]. Examples of non-linear sound generation commonly found on a wind turbine include AGI noise and aerofoil self-noise. The high-frequency small-amplitude pressure perturbation involved has to be resolved accurately. Therefore, only the spatial and temporal discretisation schemes with high-order truncation accuracy and high spectral resolution are suitable. Moreover, acoustic waves are inviscid [44, 53]. Hence the artificial dissipation and dispersion level acceptable for other CFD problems might lead to unacceptable attenuation of sound waves. Furthermore, numerical errors introduced by artificial BC can easily contaminate the computed sound field. Therefore, different BC to those used in other CFD problems are required for CAA. The issues of choosing the appropriate discretisation schemes, numerical stabilizing techniques and BC will be discussed in more detail later in Chapter 3. Now we will look at some examples of CAA research on wind turbine noise.

As mentioned in the previous section, many hybrid methods require the use of numerical discretisations to solve the set of acoustic equations. These hybrid methods, in which the acoustic pressure fluctuation is computed indirectly, are examples of CAA methods. Scott [54] provided the first reference solution to the category 3 problem 1 from the Third [55] and Fourth [56] CAA

Workshops. This problem investigated numerically the acoustic responses of a Joukowski aerofoil to an impinging small-amplitude 2D periodic vortical gust. Since the gust amplitude was small, Scott used the linearised Euler equations to model the problem. By defining a velocity potential Φ, whose gradient was the velocity, the linearised Euler equations were reduced to a convective wave equation in Φ [54]. The unsteady pressure perturbation was then found by its relation to Φ. An unsteady aerodynamic code called *GUST3D*, which utilised a frequency domain approach with second-order central differences and a far-field pressure radiation BC, was used to solve the wave equation in Φ. The mean flow quantities required by *GUST3D* were calculated separately by a potential flow solver. There are other reference solutions to this CAA benchmark problem. Two such solutions, which were based on the full Euler equations similar to the current study, will be used for validating the current numerical results later in Chapter 4.

Another type of hybrid methods is the acoustic/viscous splitting method (also referred to as incompressible/acoustic splitting in some studies) first proposed by Hardin and Pope [57]. An advantage of their approach over the acoustic analogy is that the source strength is obtained directly without the need of heuristic models.

Shen and Sorensen [58] later proposed a new formulation which avoided the inconsistency regarding the absence of source term in the rearranged acoustic equations in the original formulation of Hardin and Pope. In their approach, the viscous incompressible flow was first computed by solving the incompressible N-S equations. The pressure fluctuation in time was assumed to be isentropic. Then it was shown that the energy equation was not required to describe the acoustics, and hence was replaced by the isentropic pressure-density relation equation. In order to derive the acoustic equations, the compressible flow variables were decomposed into two parts: the incompressible mean flow and the perturbations. Then by substituting the decomposed variables into the governing compressible continuity, momentum and isentropic pressure-density relation equations, and ignoring the viscous terms, the acoustic equations were derived. The sound field was computed by solving the inviscid acoustic equations. Shen and Sorensen used this approach to analyse the vortex shedding noise due to the laminar flow past a circular cylinder at low Mach numbers [59]. Second-order finite volume/finite difference (FV/FD) methods were used to solve the flow and acoustic equations. Tam and Webb acoustic BC and slip conditions were used for the far field and the solid surfaces respectively. The results were reasonable. They extended their algorithm and investigated the noise due to a turbulent flow past an aerofoil at 20° angle of attack with a flow Mach number of 0.2. RANS [60] and later LES [61] were used for the flow part of the calculations. General agreement with experimental noise spectrum was observed.

Zhu [62] used the same acoustic/viscous splitting method as Shen and Sorensen in his study of wind turbine aeroacoustics. However, high-order optimised compact FD scheme and high-order dispersion-relation-preserving (DRP) scheme were used to discretise the acoustic equations. These schemes were optimised to capture the high-frequency small-amplitude acoustic waves. The methodology was validated with the analytical solutions of acoustic wave scattering from a circular cylinder

and sound generation due to a spinning vortex pair. An attempt was made to simulate the noise emitted from a large wind turbine rotor. However, possibly due to the limited number of grid points and the use of RANS turbulence model, only some general trends of wind turbine noise were observed and the solution was limited to the low-frequency range.

Another similar type of hybrid method was developed by Ewert to investigate an aircraft slat noise problem [63]. The acoustic part was based on the acoustic perturbation equations (APE), which were derived from the linearised Euler equations (LEE). This system of equations, with source term assumed to be a type of turbulence-related vortex noise source [63], was solved by using the fourth-order DRP scheme of Tam and Webb for spatial discretisation and a fourth-order Runge-Kutta (RK) method for time integration [63]. The source term in the APE was evaluated by using the turbulent velocity fluctuation computed by Ewert's random particle-mesh (RPM) method, which was based on the digital filtering (DF) of random data first developed by Klein et al. [64] for synthesizing pseudo-turbulent incident velocity field. The RPM synthesised stream-function on a source patch where vortex sound originated within the CAA domain. Hence the generated velocity field was divergence-free. A steady state RANS simulation was needed to determine the mean-flow streamlines and the filter kernel parameters required by the RPM method, as well as the mean-flow quantities required by the APE. The computed pressure spectra showed general good agreement with experimental data [63]. A fast RPM (FRPM) discretisation approach had been developed by Ewert [65,66]. This approach utilised a background mesh to store the mean-flow quantities computed by the RANS simulation and the source strength. Instead of using distinct streamlines, the particles were evenly distributed over the background mesh. Ewert's methods were more computationally inexpensive compared to the direct source computations by using LES or DNS. More details of the DF method of Klein et al. [64] and the RPM/FRPM method of Ewert [65,66] for generating pseudo-turbulence will be discussed later in Section 3.4. Other than aircraft slat noise, some examples of the applications of Ewert's methods included jet noise [65,66] and broadband fan interaction noise [67,68].

In contrast to the hybrid methods, the other main type of CAA methods involves computing the unsteady flow and the acoustic field directly in one step by solving the compressible N-S or Euler equations. These methods are known as the direct methods. Compared to direct methods, hybrid methods allow the accuracy of the numerical methods employed for the flow part to be relaxed. High-order numerical schemes with high spectral resolution are only required for the acoustic part. The time step size of acoustic simulations are usually smaller than flow simulations. Also, the computation of the sound spectrum requires long time series of solution. Hence the saving in computational cost by the use of numerical schemes with different order of accuracy in hybrid methods is usually significant. Hybrid methods are also advantageous since the flow computation is only required in the region where significant noise is produced. Relatively more computational power can be used to solve the acoustic equations, which are simpler than the compressible N-S or Euler equations. Hence, sound can be computed over a larger acoustic grid, which does not need to coincide with the flow grid. Moreover, the flow part of many hybrid methods is incompressible, which can be solved faster than a compressible flow field.

Although more computationally expensive, direct methods are used in many CAA researches. Hybrid methods are based on the assumption that the problem can be separated into the flow and the acoustic parts. Direct methods require no such assumption. Also with ever advancing high-performance computing technology, flow configurations of increasing complexity are gradually being studied by direct methods. Through these direct studies, insight into the fundamental noise generating mechanisms of more complex flow configurations might be deduced.

An example of direct method is the study of blade tip noise by Fleig et al. [3] mentioned before. They used compressible LES in the near-field (one to two chord-lengths away from the rotor blade) to compute the flow and the noise directly. An acoustic analogy, in the form of a permeable surface FW-H formulation, was used for the far-field region, which stretched to 200 chord-lengths away from the blade. For the spatial and temporal discretisations, a third-order FD upwind scheme and a second-order implicit approximate factorization Beam-Warming scheme were used respectively. Convective BC were used along the domain outer boundaries. The grid became coarser towards the outer boundaries so that non-reflecting conditions could be achieved. The subgrid model used was the Smagorinsky model. To test the accuracy of the third-order upwind scheme, Fleig et al. performed a numerical test of the propagation of a small acoustic perturbation in a uniform flow with Mach number 0.5. It was found that as long as the number of grid points per wavelength was sufficiently large $(25 - 30)$, the numerical result was accurate.

A blade of a two-bladed upwind *WINDMELIII* wind turbine with a rotor diameter of 15m and a rated power of 16.5kW was modelled in the study. The tip speed ratio was 7.5 and the tip speed was 53.3m/s, corresponding to a Mach number of 0.16. The Re based on the reference chord length was 1.0×10^6. Since the study focused on the tip region, an extremely fine grid was used there to provide the very high resolution required. The total number of grid points was about 300 millions. The physical time step was about 2.0×10^{-7} seconds. Due to the limitation in computational time, the blade only rotated by 20.4° in the 50ms of the simulation. Hence the tip vortex was still in the transient state. In addition to the original *WINDMELIII* tip geometry, which had a curved and backward swept leading edge and a straight trailing edge in the outermost 95% of the span, a so-called *ogee* tip was also simulated. The *ogee* tip was found in various wind tunnel experiments and field measurements to be noise-reducing [3]. The difference in tip shape had little effect on the aerodynamic performance of the blade, since the tip shape only changed beyond 95% distance from the root. When compared to the reference experimental measurement, Fleig et al. found that the LES under-predicted the power coefficient. They suggested that it was possibly due to the lack of inflow turbulence in the simulation. By analysing the streamwise voricity, Fleig et al. found that for the *ogee* tip, the tip vortex shed was reduced and the tip vortical structure was smoother and spread further inboard. This weaker and more widespread streamwise vorticity in the tip region led to reduced interaction with the blade trailing edge. Consequently, the sound pressure level due to the *ogee* tip was also reduced - as much as 5dB for frequencies above 4kHz [3]. Fleig et al. attributed the reduced tip vortex and the reduced tip vortex and trailing edge interaction to the curved trailing edge of the *ogee* tip. Arakawa et al. [4] further showed that the original *WINDMELIII* tip had stronger

surface distributions of monopole and dipole terms of acoustic pressure.

2.4.1 The Current CAA Strategy for AGI Noise Investigation

In the previous sections, we have discussed wind turbine aeroacoustic studies by using experimental, theoretical and semi-empirical methods. For the study of AGI noise, these approaches have some drawbacks. It is hard to isolate the effect of AGI noise from other noise-producing mechanisms under various flow conditions by using experimental or field studies. The accuracy of the semi-empirical wind turbine noise prediction codes is questionable in many flow conditions. The theoretical approaches based on rapid distortion theory by Goldstein, Myers and Kerschen are restricted to 2D space.

Using CAA methodology, it is possible to isolate the effect of AGI noise from other wind turbine noise sources by using the Euler equations as the governing equations. In this case, aerofoil self-noise, which originates within the boundary layer and the wake regions, cannot develop. The current study employs the sponge layer technique and the characteristic non-reflecting BC, to introduce the non-uniform unsteady incident flow while minimising the reflections of the out-going quasi-linear characteristic waves at the domain boundaries. The current BC has been shown to be able to provide a *clean* environment for AGI noise to develop [33].

Fourth-order optimised compact FD schemes [36, 37], in conjunction with sixth-order compact filters [37, 38], are used for the spatial discretisation. For time integration, a standard fourth-order four-stage R-K time marching scheme is used to advance the solution. A type of multi-block structured grid with a H-topology is used. The upstream velocity consists of a uniform portion and a small-amplitude unsteady motion superposed on it. Since the incident disturbance is purely vortical and divergence-free, there is no incident acoustic field.

2.5 Experimental Studies on the Aerodynamic Effects of Leading-Edge Modifications

It has been suggested that leading-edge tubercles on the pectoral flippers of humpback whales acted like vortex generators, which helped maintaining lift at high angle of attack during turning maneuvers [14, 15, 69, 70]. This improved aerodynamic performance at high α is important to the humpback whales, whose feeding method involves performing tight turning maneuvers around a school of prey. At about 28% of the total length of the animal, the flippers of the Humpback whales are the longest among all the species of whales [14]. Their flippers are wing-like and have high aspect ratio. There is a slight sweep-back towards the tip of a flipper. The inter-tubercular distance in general decreases towards the tip and is fairly constant over the mid-span. The cross sectional shape of their flippers are typical of lifting aerofoils. It has a large, blunt and rounded leading edge and thin and tapering trailing edge. The mid-span aerofoil is similar in design to NACA $63_4 - 021$.

A typical flipper has an averaged thickness to chord ratio of 23% local chord, and its location of maximum thickness varies from 49% chord at tip to 19% at mid-span [14]. Fish and Battle [14] observed that barnacles were always absent between tubercles. This indirectly indicated the existence of high-velocity water flows between the tubercles since barnacle larvae could not attach to areas with high water velocity or velocity gradient.

Miklosovic et al. [12] conducted wind tunnel experiment using idealised humpback whale flipper models, which were constructed based on NACA 0020 section. The models were mounted vertically in the wind tunnel with the roots attached to a rotating yaw table, which changed the angle of attack. Leading-edge sinusoidal tubercles with decreasing inter-tubercular spacing towards the tip were used for the outer two-thirds span of one of the models, while the other model had a smooth leading edge. The planform area of the two models were the same. However, for the flipper model with tubercles, the aerofoil shape varied along the span. Re used was about 5×10^5. They found that leading-edge sinusoidal tubercles were able to delay stall angle and increase total lift without increasing drag. The performance of the two models below about $\alpha = 8.5°$ was near identical. Stanway [17] performed water tunnel tests using scaled down versions of the flipper models of Miklosovic et al. [12]. Four values of Re between 4.4×10^4 and 1.2×10^5 were tested. The result showed that the flipper model with smooth leading edge showed more rugged lift curves as α approached the stall angle. The model with tubercles had smoother lift curves and more gradual stall. However, except for the highest Re case, the model with tubercles reached lower maximum lift. Only the case with the highest Re showed the all-round performance improvement observed by Miklosovic et al. [12].

In a later work, Miklosovic et al. [71] investigated experimentally the effect of leading-edge tubercles on 3D aerofoils. Similar flipper models to those used in their earlier study mentioned before were also tested. The cross-sectional shapes of the 3D aerofoils and the flipper models were based on NACA 0020 aerofoil. The 3D aerofoils were tested in a smaller wind tunnel with the tunnel walls very close to the ends of the models. Hence the tunnel walls acted like end-plates and helped restricting the flow in the spanwise direction. Unlike the flipper models, the tubercle amplitude, wavelength and inter-tubercular distance were constant along the whole span of the 3D aerofoils. For the 3D aerofoils tests, Re used was about 2.74×10^5 and the freestream Mach number $M_\infty = 0.13$; for the flipper models tests, Re was approximately 5.34×10^5 and $M_\infty = 0.21$. Miklosovic et al. found that leading-edge tubercles led to localised leading-edge separation and the onset of vortical lift dominance at an α below the original stall angle of the unmodified models with straight leading edges. Their results also showed that relative to the respective unmodified models, the 3D aerofoils with tubercles caused a much larger loss of pre-stall lift, smaller gain in post-stall lift and bigger pre-stall drag penalty. The flipper models with tubercles showed significant drag reduction in the post-stall regime. They attributed this difference in aerodynamic performance to the ability of the leading-edge tubercles in inhibiting spanwise stall progression on the flipper models.

Weber et al. [72] conducted a water tunnel experiment to investigate the effect of leading-edge tubercles on the hydrodynamics of rudder models. The baseline aerofoil used was NACA 0016.

Similar to the studies by Miklosovic et al. [12, 71], the aerofoil shape varied along the span due to the leading-edge tubercles. The rudder models had low aspect ratios, unswept leading edges and swept trailing edges with the chords reducing towards the tips. Two models with leading-edge tubercles along the whole span and one without were tested. The two models with tubercles had different tubercle wavelengths. The Re ranged between 2×10^5 and 8.8×10^5. Weber et al. found that tubercles led to earlier onset of stall, lower maximum lift, less abrupt stall behaviour and a flatter post-stall lift curve. Compared to the model with straight leading edge, the post-stall lift of the rudders with tubercles was only higher for the lower Re tested. No pre-stall lift penalty was observed for the rudders with tubercles. Weber et al. found that at low Re, leading-edge tubercles did not lead to any drag penalty. However, at the higher Re of 8×10^5, higher drag was observed for the modified rudder model with smaller tubercle wavelength. By analysing the lift to drag ratio at different Re, Weber et al. suggested that leading-edge tubercles led to the greatest improvement in hydrofoil performance at low Re ($< 7\times10^5$). However, the all-round performance improvement suggested by Miklosovic et al. [12] and Stanway [17], observed at $Re = 5\times10^5$ and $Re = 1.2\times10^5$ respectively, was never seen in the experiment by Weber et al. This difference is to be expected since models with totally different geometry were used by Miklosovic et al./Stanway and Weber et al. An interesting aspect of the experiment by Weber et al. was the study of cavitation, which is an unsteady flow phenomenon that occurs in high speed liquid flow over a surface where local flow velocity is high and pressure is low. Hence cavitation bubbles can appear on the suction side of a lifting surface and in region where vortices exist. Weber et al. found that the three models tested had different cavitation onset characteristics. However, tip vortex cavitation was always the first form of cavitation observed. For the models with tubercles, cavitations were restricted to the troughs; for the model with a straight leading edge, sheet cavitation could be observed along much of the leading edge. This observation showed that, along the leading-edge tubercles, the highest suction exists in the troughs.

Johari et al. [16] investigated the effect of leading-edge sinusoidal tubercles in a water tunnel experiment. 3D aerofoils based on NACA 63_4-021 with and without tubercles of equal planform area were used. They tested a range of tubercle amplitude and wavelength corresponded to the morphology of the humpback whale flippers. Their results showed that at $Re = 1.83\times10^5$, the modified aerofoils with tubercles in general had lower maximum lift, and stall occurred at an α smaller than the NACA 63_4-021 stall angle. However, the modified aerofoils stalled more gradually and had higher post-stall lift level. Since the modified aerofoils stalled earlier compared to NACA 63_4-021, they also showed higher level of drag between their respective stall angles and the NACA 63_4-021 stall angle. Johari et al. also found that a smaller tubercle amplitude led to relatively higher maximum lift and stall angle. Although their results also showed that larger tubercle amplitudes helped maintain higher lift up to $\alpha = 30°$, hence resulted in more plateau-like post-stall lift curves. This softer stall behaviour of 3D aerofoils with leading-edge tubercles was also observed by Miklosovic et al. [71]. Johari et al. suggested that varying the wavelength had negligible effect, although only two different wavelengths were tested. Johari et al. also performed flow visualization by tufts. They found that the baseline NACA 63_4-021 aerofoil exhibited trailing-edge stall. For the modified 3D aerofoils with tubercles, separated flows were first observed behind the troughs. At high α, the flow

remained attached on the peaks of the leading-edge tubercles [16]. This led to the higher post-stall lift observed for the modified 3D aerofoils. In a very similar follow-on study, the flow over the models were visualised by using dye [18]. The visualization indicated the formation of counter-rotating streamwise vortex pairs in the troughs between the tubercles at low Re.

Hansen et al. [13] investigated the effect of leading-edge sinusoidal tubercles in a wind tunnel experiment with 3D aerofoils based on NACA 0021 and NACA $65-021$. Both aerofoils had a thickness to chord ratio of 21%, similar to a typical humpback whale flipper. The location of the maximum thickness for NACA 0021 and NACA $65-021$ were at 30% and 50% chord respectively. NACA $65-021$ had a lower maximum lift, larger stall angle and more gradual stall than NACA 0021. The Re used for the tests was 1.2×10^5. Only two configurations of modified NACA $65-021$ were tested, both with the same tubercle wavelength. Most results were for NACA 0021. Hansen et al. suggested that the modified NACA $65-021$ with tubercles led to smaller reductions in maximum lift and stall angle compared to the modified NACA 0021. They attributed this to the further aft position of maximum thickness of NACA $65-021$ [13]. The general effects of reduced maximum lift and stall angle, more gradual stall and higher post-stall lift were observed for the 3D aerofoils with tubercles. Hansen et al. [13] agreed with Johari et al. [16] that the smallest tubercle amplitude led to the highest maximum lift. Hansen et al. found that for the modified NACA 0021 with tubercles, there appeared to be an optimal tubercle wavelength which could lead to all-round lift and drag performance improvements. However, the largest tubercle wavelength resulted in poorer lift performance throughout [13]. Another difference to the results by Johari et al. was that beyond the stall angles of the unmodified aerofoils, the 3D aerofoils with tubercles always showed slightly lower drag levels. Hansen et al. also performed a hydrogen-bubble visualization, which showed the formation of streamwise vortices in the troughs between tubercles [13].

There are several reasons for the varying degree of observed aerodynamic benefits due to leading-edge tubercles suggested by these experimental studies. First, some of these studies used flipper models with planform shapes based on real-life humpback whale flippers; while others used 3D aerofoils. Test results with and without wing-tip effect are obviously different. The second factor is the effect of Re. It can be seen from the studies by Miklosovic et al. [12] and Stanway [17] that using similar idealised whale flipper models, the all-round lift and drag performance improvements found by Miklosovic et al. at a Re of 5×10^5 were not observed at the lower Re range ($< 1.2\times10^5$) by Stanway [17]. Third, different aerofoils were used in these studies. Even when the same or similar aerofoils were used as the baseline, none of these studies employed a single aerofoil shape along the span for the models with leading-edge tubercles. The cross-sectional shapes at different spanwise locations are deformed or stretched non-uniformly and differently by the leading-edge tubercles. Hence, even within one study, aerofoils or flipper models with different tubercle wavelength and amplitude would have different spanwise variation of aerofoil shape. This variation might contribute to the different observations made by Johari et al. [16] and Hansen et al. [13].

Nevertheless, these experimental studies have shown that leading-edge tubercles can lead to a

more gradual stall characteristic and better post-stall performance than straight leading edges at the expense of marginal reduction in pre-stall performance [12–18]. The degree of performance enhancement further depends on the Re, the tip effect and the tubercle wavelength and amplitude. It may therefore be possible to achieve all-round lift and drag performance improvements with careful designs. Hence potentially, leading edge tubercles, or similarly wavy leading edges, could improve the aerodynamic performance of wind turbine blades [70, 73]. Howle [73, 74] designed a pair of modified wind turbine blades with leading-edge tubercles based on the humpback whale flippers along the outer two-thirds of the span, and fitted them to a two-bladed *Wenvor* upwind wind turbine with a rated power of 25kW. The diameter of the turbine was 10.2m. A field study was conducted to measure the electrical output power of the modified turbine [74]. Howle then compared the measured data with the published data of the original *Wenvor* wind turbine. From the plot of output power versus wind speed at hub-height, he found that the modified blades led to greater positive gradient, i.e. the same output power was reached at a lower wind speed for the modified blades. Murray et al. [75] investigated experimentally the effect of leading-edge tubercles on marine tidal turbine blades. They found that the modified blades with tubercles on the outer portion of the leading edges significantly out-performed the baseline blades with straight leading edge at low flow speeds, while the higher-speed performance was not degraded. Hence leading-edge tubercles can potentially be used to overcome the difficulty of extracting useful power from low-speed tidal flow encountered by current designs.

Wavy leading edges were also found to be useful in suppressing flow separation over a delta wing with moderate sweep angle by Goruney and Rockwell in a water channel experiment [76]. The delta wing models were held at $\alpha = 25°$ and $Re = 15,000$ for all the tests. Stereoscopic particle image velocimetry (PIV) was used to observe the change in the near-surface flow topology due to a wavy leading edge. Goruney and Rockwell suggested that for small ratios of leading-edge wavelength to amplitude, when the amplitude was increased to certain value, flow separation could be eradicated [76]. Ozen and Rockwell conducted a water channel experiment on the effect of a wavy leading edge on a flapping rectangular flat-plate wing [77]. The models were mounted at $\alpha = 8°$ and $Re = 1,300$. Only one combination of leading-edge wavelength and amplitude was tested. They found by using PIV that the wavy leading edge led to drastic changes to the flow vortical structure inboard from the tip [77].

To understand further the finer details of the flow features that make leading-edge tubercles and wavy leading edges very useful, numerical simulations, which will be discussed in the next section, are required.

2.6 Numerical Studies on the Aerodynamic Effects of Leading-Edge Modifications

Watts and Fish [78] used a 3D panel code based on a first-order vortex method to study the influence of wavy leading edges on a rectangular wing at $\alpha = 10°$. They found that wavy leading edges led to an increase in lift and a reduction in induced drag, hence reduced wing tip vorticity. They also found no penalty in aerodynamic performance at $\alpha = 0°$.

Van Nierop et al. [79] developed an aerodynamic model in their study of leading-edge tubercles. In contrast to most other studies, they opposed the idea that tubercles act like vortex generators since both the wavelength and amplitude of the tubercles were much larger than the boundary layer thickness [79]. Their model was developed for elliptical wings with and without leading-edge tubercles, and was based on the idea of wing circulation for a potential flow. The wing was assumed to be thin. Downwash was taken into account by using the lifting line theory. Although there was a spanwise variation of the flow, no actual spanwise flow was modelled. The sectional circulations were summed along the span to estimate the lift. An empirical separation criterion originally developed for flat plates was used to estimate the sectional stall angles. The stalled sections did not contribute to the total lift. Based on the results of Johari et al. [16], the fully-stall lift coefficient was simply set to 0.6 for all the wings tested in their model. Their model predicted lowest pressure in the troughs of the leading-edge tubercles on the wing top surface. In addition to this, the shorter chord and similar thickness compared to the sections behind the peaks caused a more adverse pressure gradient behind the troughs. Therefore, separation happened behind the troughs first. Their computed lift curves suggested that tubercle wavelength had nearly no effect on the lift. This might be due to the 2D nature of the wing sectional flow in their model. They also found that larger tubercle amplitude led to lower maximum lift and more gradual stall. This observation was due to the earlier onset of stall behind the troughs. Van Nierop et al. attributed the stall-delaying capability of leading-edge tubercles to the non-uniform downwash along the span. More specifically, the stronger downwash behind the peaks delayed the overall wing stall [79].

The model developed by van Nierop et al. was subjected to a lot of assumptions and simplifications. A more detailed numerical study was that by Pedro and Kobayashi [19], who simulated numerically the wind tunnel experiment on whale flipper models by Miklosovic et al. [12]. They employed a detached eddy simulation (DES) method to simulate the incompressible flow around the flippers by using the commercial CFD package *Fluent*. The Re used was $5{\times}10^5$ and the freestream Mach number was 0.18. Their results showed the formulation of streamwise vortices behind the tubercles. (On close examination of the vorticity magnitude plots in their paper, one can see these vortices in the troughs.) Pedro and Kobayashi suggested that the streamwise vortices re-energised the boundary-layer flow, particularly in the outboard region, and this delayed flow separation. Since their flipper models had reducing chord along the span from root to tip, the local Re at the tip was much smaller than that in the root region. Their results showed that this spanwise variation of Re led to different types of separations: leading-edge separation at the tip and trailing-edge separation along

the rest of the flipper span. Pedro and Kobayashi suggested that this separation pattern encouraged the spread of fully-separated flow from the tip towards the inboard section observed on the wing with straight leading edge. They further suggested that the vortices generated by the leading-edge tubercles also acted like wing fences, which served as physical barriers to the spanwise motion and prevented the inboard spread of fully separated flow from the tip.

Weber et al. [80] also conducted a numerical study of the wind tunnel experiment by Miklosovic et al. [12]. They employed two different commercial CFD codes: *STAR-CCM+* and *SolidWorks Flow Simulation (SFS)*. Their simulations were based on the RANS equations. As a natural consequence of using RANS simulations, good agreement of the predicted and measured lift and drag coefficients were only observed for the pre-stall regime. Nevertheless, some qualitative observations from their numerical results were similar to previous findings by other researchers. Weber et al. also noted trailing-edge separation occurred along much of the span of the flippers, and the presence of leading-edge tubercles prevented the spread of the fully-separated flow from the stall regions. This led to the greater post-stall lift observed for the flipper with tubercles in the experiment by Miklosovic et al. [12]. Weber et al. suggested that each tubercle acted like a small delta wing with 45° sweep and a rounded apex. A leading-edge vortex then formed on the suction side of each tubercle [80]. They further suggested that the vortices led to downwash over the peaks and upwash in the troughs.

A numerical study on wavy leading edges was conducted recently by Yoon et al. [20]. They investigated the 3D steady incompressible viscous flow around a low aspect ratio rectangular wing with a tip and varying extent of leading-edge waviness from the tip. They used *Fluent* and their simulations were based on the RANS equations. They defined a waviness ratio S_w, which was the ratio of the spanwise length covered by the leading-edge waviness to the wing full-span. Six different S_w: 0.0, 0.2, 0.4, 0.6, 0.8 and 1.0 were investigated. The wing with a straight leading edge, i.e. $S_w = 0.0$, will be referred to as the unmodified wing. NACA 0020 aerofoil was the sole wing cross-sectional profile. The wavy leading edges did not change the wing aerofoil shape. Fixed values of leading-edge wavelength and amplitude were used. The simulations were performed at $Re = 10^6$ for $0° \leqslant \alpha \leqslant 40°$. Yoon et al. [20] found that for α between 0° and 12°, the effect of wavy leading edges with different waviness ratios on the lift coefficient was negligible. The wing with a waviness ratio of 0.2 had essentially the same lift curve as the unmodified wing, which stalled at $\alpha = 20°$. For $S_w = 0.4$, 0.8 and 1.0, stall happened at $\alpha = 16°$. The wing with $S_w = 1.0$ showed the most gentle stall with the smallest loss of lift compared to its maximum lift, and it had $10 - 15\%$ more post-stall lift compared to the unmodified wing. For $S_w = 0.4$ and 0.8, the stalls were somewhat more gentle than that of the unmodified wing. The post-stall lift for $S_w = 0.4$ increased to a slightly higher level than the unmodified wing. For $S_w = 0.8$, the post-stall lift eventually increased to the same level as that of $S_w = 1.0$ for $\alpha \geqslant 32°$. For the wing with $S_w = 0.6$, stall occured the earliest at $\alpha = 12°$. Hence the lowest lift coefficient amongst all the cases was achieved at this waviness ratio at $\alpha = 16°$ soon after stall. The lift eventually increased and recovered to a level in between $S_w = 0.4$ and 0.8 for $\alpha \geqslant 32°$. In general, the enhanced post-stall lift and more gradual stall observed for the wings

with more significant waviness, i.e. $S_w = 0.4$, 0.6, 0.8 and 1.0, relative to the wings with insignificant waviness, i.e. $S_w = 0.0$ and 0.2, were consistent with the findings from the experimental studies mentioned earlier.

The variations of drag with α for the unmodified wing and the wing with $S_w = 0.2$ were nearly identical. For $S_w = 0.4$, 0.6, 0.8 and 1.0, due to the earlier onset of stall, especially for $S_w = 0.6$, a higher level of drag between their respective stall angles and the stall angle of the wings with $S_w = 0.0$ and 0.2 was observed. As the α increased further, the drag of the wings with $S_w = 0.4$, 0.6, 0.8 and 1.0 reduced and eventually became nearly identical to that of the unmodified wing.

By studying the pressure coefficient distribution, the limiting streamlines and the spanwise vorticity on the wing top surfaces, Yoon et al. [20] further identified some flow features. They found the pressure coefficient on the wavy leading-edge peaks was similar to that of the straight leading edge, while that in the troughs was lower. This led to greater adverse pressure gradient and hence local onset of stall behind the troughs. On the other hand, the greater suction maintained in the troughs soon after stall occurred for the wing with $S_w = 1.0$ reduced the lift loss and led to the most gentle stall. Yoon et al. also found the formation of spanwise vortical structures near the wavy leading-edge troughs. For wings with $S_w > 0.2$, non-localised widespread flow separation first developed from the first trough on the inboard side. At high α, such as $\alpha = 32°$, the unmodified wing showed flow separation from the leading edge. However, the wavy leading edges were able to retain flow attachment on its peaks. This effect is the most pronounced for the wing with $S_w = 1.0$, which had the highest post-stall lift as a result. The attached flow on the peaks at high α was also observed by Johari et al. [16].

Hence, most observations from the numerical studies were consistent to those from the experimental investigations. Also, wavy leading edges show the same aerodynamic benefits as leading-edge tubercles. The formation of vortical structures in the troughs of wavy leading edges is well supported by many researches. The higher suction in the troughs leads to a much more gentle stall behaviour. The ability of the peaks to maintain attached flow at high α results in higher post-stall lift. In the next section, the published works to-date on the aeroacoustic effect of leading-edge modifications will be reviewed.

2.7 Studies on the Aeroacoustic Effects of Leading-Edge Modifications

Most studies of leading-edge modifications so far focused on the aerodynamic performance. However, it is obvious that the aeroacoustic performance will also be affected. Hansen et al. [21] investigated experimentally the effect of leading-edge sinusoidal tubercles on aerofoil tonal noise. This type of tonal noise originates from the trailing edge of the aerofoil and can only be generated when laminar boundary layer exists on the aerofoil surface. A few studies proposed a self-excited acoustic feedback

loop as opposed to vortex shedding as the generation mechanism of aerofoil tonal noise [21]. Hansen et al. measured the sound by using microphones. Two sets of measurements were taken: one from the low-speed wind tunnel without any form of acoustic wall treatment, referred to as the hard-walled wind tunnel; the other from an anechoic wind tunnel. The Re based on the freestream velocity of 25m/s and mean chord length was 1.2×10^5. The incident flow in the low-speed wind tunnel had a turbulence intensity of 0.8%, so AGI noise was not a significant source of noise. Hansen et al. [21] found that trailing-edge tonal noise only occurred for $\alpha < 8°$, i.e. before the aerofoils stalled, and that no tone was present at $\alpha = 0°$. The absence of tone at $\alpha = 0°$ might be due to the flow symmetry about the symmetrical NACA 0021 and the modified aerofoils based on it. Their results further showed that the tonal frequency measured in the anechoic wind tunnel was higher than that in the hard-walled wind tunnel. The tonal noise also occurred over a much wider range of α in the hard-walled wind tunnel. The anechoic tunnel results showed that the presence of tubercles in most cases eliminated tonal noise altogether, and there was a small reduction of broadband noise around the peak tone frequency of the unmodified aerofoil. Hansen et al. also found that tubercles with smallest wavelength and largest amplitude were in general the most effective at reducing tonal and broadband trailing-edge noise.

A contemporary experimental and numerical study by Clair et al. [22] showed that wavy leading edges could reduce AGI noise without degrading aerodynamic performance. The aim of their study was to reduce the AGI noise generated by turbofan blades. The experimental work of Clair et al. was conducted in an anechoic open jet wind tunnel. An upstream turbulence grid was used to generate the incident turbulence that impinged upon a 3D NACA aerofoil model. Several flow speeds and angles of attack were tested. Three wavy leading-edge geometries were analysed and compared to the baseline model with a straight leading edge. Clair et al. found that among the three wavy leading-edge geometries tested, the one with the largest leading-edge amplitude led to the biggest AGI noise reduction. They further found that wavy leading edges remained efficient in reducing AGI noise up to an angle of attack of 15°, and wavy leading edges are the most efficient in reducing the mid-frequency (about 3kHz) noise. In general, wavy leading edges could lead to a noise reduction of 3 to 5dB.

Clair et al. [22] also numerically assessed their wind tunnel results. Their numerical method was based on a CAA code which solved the non-linear Euler equations by splitting the conservative variables into the mean and the perturbed components. High-order methods were used for the numerical discretisations. Multi-block structured grid was employed. Their code was parallelised using the MPI library. Clair et al. employed Tam's inflow and outflow boundary conditions, which were derived from the asymptotic solutions of the linearised Euler equations. For 3D calculations, spanwise periodic boundary condition was applied. The divergence-free incident pseudo-turbulent velocity was synthesised from a stochastic model, which simulated part of the Von Karman energy spectrum using a number of discrete frequency modes. The streamwise and spanwise perturbed velocity components were set to zero, only the vertical perturbed velocity was generally non-zero. The CAA code only directly computed a narrow strip of the desired span, and one wavy leading-edge

wavelength was simulated. The near-field solutions computed by the CAA code were fed into a FW-H equation solver for integration on a control surface to evaluate the far-field noise radiation. The numerical solutions of Clair et al. for 2D and 3D flat plates agreed very well with the theoretical results of Amiet. Clair et al. then applied their coupled CAA/FW-H code to 3D NACA aerofoils with and without wavy leading edges. In order to reduce the computational cost to an acceptable level, the incident gusts employed by Clair et al. only varied in the streamwise direction. The perturbed velocity was convected by a uniform mean flow. The numerical and experimental results of Clair et al. showed good agreement in terms of noise reduction due to the wavy leading edge up to about 3.5kHz. Their numerical results over-predicted the noise reduction in the higher-frequency range compared to the experimental measurements. Clair et al. attributed this over-prediction to the lack of spanwise variation in the incident gust [22]. The effect of convecting the incident gust by a more realistic sheared mean flow around the aerofoil computed by a separate RANS calculation was also investigated. From their numerical results, Clair et al. suggested that the interaction between the perturbed velocity and the sheared mean flow near the aerofoil surface caused strong pressure fluctuations, which were further amplified when passing over the trailing edge. However, the leading edge remained the most dominant sound-producing region [22]. Clair et al. found that the use of a more realistic sheared mean flow improved the agreement between the numerical and the experimentally-measured sound power spectra.

Wind turbine blades are constantly subjected to atmospheric wind gust and turbulent wake from other wind turbines in a wind farm. Hence wind turbines almost always generate AGI noise. The current study is among the first to investigate the effect of wavy leading edges on AGI noise. The current study aims to deliver a fundamental understanding of the effects of wavy leading edges on AGI noise by considering velocity disturbances predominantly in streamwise and vertical directions using high-fidelity numerical simulations. Synthetic unsteady incident gust similar to that used by Clair et al. [22] will be incorporated into the current code in the future so that the current results could be more directly applicable for wind turbine aeroacoustic research. In the next chapter, the current numerical methodology will be explained in detail.

3 Numerical Methodology

In this chapter, the numerical methodology used in the current research will be explained. The aim of the current study is to investigate the effect of wavy leading edges on AGI noise. Since the generation of AGI noise does not require viscosity, and other types of noise source are not of interest to the current study, the fully compressible 2D and 3D Euler equations are used as the governing equations. The current methodology is based on the 3D Euler equations written in the conservation-form as a compact vector equation, i.e.

$$\frac{\partial \mathbf{Q}}{\partial t} + \frac{\partial \mathbf{E}}{\partial x} + \frac{\partial \mathbf{F}}{\partial y} + \frac{\partial \mathbf{G}}{\partial z} = 0, \tag{2}$$

where $\mathbf{Q} = (\rho, \rho u, \rho v, \rho w, \rho e)^T$ is the 3D conservative variables vector, with ρ, u, v, w *and* e the density, x-velocity component, y-velocity component, z-velocity component and total energy per unit mass respectively; t is time; $\mathbf{E}$, $\mathbf{F}$, $\mathbf{G}$ are the inviscid flux terms, which are functions of $\mathbf{Q}$ and are defined as

$$\mathbf{E} = \left[\rho u, \rho u^2 + p, \rho uv, \rho uw, (\rho e + p)u\right]^T;$$
$$\mathbf{F} = \left[\rho v, \rho uv, \rho v^2 + p, \rho vw, (\rho e + p)v\right]^T;$$
$$\mathbf{G} = \left[\rho w, \rho uw, \rho vw, \rho w^2 + p, (\rho e + p)w\right]^T,$$

where p is the pressure.

The spatial and temporal discretisations employed will be explained in Sections 3.1 and 3.2 respectively. Then in Section 3.3, the BC including the sponge zone technique used to introduce the unsteady incident flow will be discussed. Finally in Section 3.5, the grid generation method used will be shown.

3.1 Spatial Discretisation

In the current study, a fourth-order optimised compact central FD scheme developed by Kim [36] is used for the numerical spatial differentiation. The scheme is optimised to achieve the highest spectral resolution. It uses a seven-point stencil, i.e.

$$\beta \bar{f}'_{i-2} + \alpha \bar{f}'_{i-1} + \bar{f}'_i + \alpha \bar{f}'_{i+1} + \beta \bar{f}'_{i+2} = \frac{1}{\Delta x} \sum_{m=1}^{3} a_m (f_{i+m} - f_{i-m}), \tag{3}$$

where f_i is the target function $f(x)$ at the i^{th} point of interest, located at x_i; and $\bar{f}'_i$ is the numerical approximation of the spatial derivative $\partial f(x)/\partial x$ at the same location. All quantities with overbar are numerical approximations. Note that the matrix on the *L.H.S.* of the scheme is penta-diagonal, which can be inverted easily by using techniques such as LU decomposition.

Since a structured grid with a H-topology is used in the current study for 2D and 3D aerofoils, the computational domain is divided into six natural sub-domains or blocks. The grid metrics between these natural blocks are discontinuous. A boundary between any of these two blocks will be referred to as a block interface from now on. It is obvious that the scheme of equation (3) can only be applied directly to grid points in the interior of a block away from any computational boundary, which is either a part of the domain boundary or a block interface. Hence in the current thesis, the scheme of equation (3) is referred to as the *interior scheme*. Special treatments are needed for the grid points near a computational boundary. For example, consider a one-dimensional domain with $N+1$ points designated by $i = 0, 1, \ldots, N-1, N$. For the boundary and near-boundary points $i = 0, 1, 2$ and $i = N-2, N-1, N$, values at points outside the domain are required based on the interior scheme. In the current study, two approaches are used to close the penta-diagonal matrix system depending on the nature of the grid metrics across a computational boundary. For the grid points near the domain boundaries, wall surfaces and block interfaces across which the grid metrics are discontinuous, sophisticated extrapolations of functions beyond the boundary are used to derive the *boundary scheme* [36]. This boundary scheme is compact but non-central, and is optimised to achieve the highest spectral resolution and to maintain fourth-order accuracy up to the boundary. Since the current study requires high computational power, parallel computing based on the MPI library is used. The six natural blocks are further divided into sub-blocks. An interface between any of these two sub-blocks is different to a block interface in that across which the grid metrics are continuous. For the grid points near these sub-block interfaces, a newly developed compact FD scheme [37] is used. This FD scheme is also fourth-order accurate and is optimised for the highest spectral resolution. It is referred to as the *halo boundary scheme* in the current thesis.

When the Euler or the N-S equations are discretised by high-order compact centred FD schemes, they are non-dissipative. If untreated, numerical instabilities can lead to large errors or even solution failure. Hence a sixth-order optimised compact low-pass filter [38] is used in the current study. In conjunction with the new halo boundary scheme, a new sixth-order compact optimised filter is used. Similar to the halo boundary scheme, halo point values are exchanged between adjacent sub-blocks and a predictor-corrector type implementation is used to compute the difference between the unfiltered and the filtered solutions [37]. Before discussing the FD schemes and the compact filters further, we will first explain the reasons of choosing this type of FD schemes in the next sub-section.

3.1.1 Reasons for Using the Current FD Schemes

For CAA, FD methods are the most widely used for spatial discretisation. The major advantage that sets FD methods apart from other methods is that FD formulation can be extended to high-order accuracy easily. Structured grids, which are challenging to construct around complex objects, are required. Lower-order FD schemes have higher dissipation and dispersion errors. For CAA, due to the usually very weak acoustic waves which propagate with very little attenuation over long distances, these large errors might mask the small pressure fluctuation that we are trying to simulate. A common

practice to overcome the large errors of these schemes is to reduce the grid spacing between the grid points, i.e. to increase the grid point density, so that the number of grid points per wavelength of a single Fourier component of the simulated function is increased. Hence a prohibitively huge number of grid points might be needed for lower-order schemes. Therefore, although higher-order FD schemes would require more operations per grid point, due to their inherent higher-order accuracy, much smaller numbers of grid points are required and it is more efficient computationally to use higher-order schemes for CAA.

In a study by Colonius and Lele [53], the dispersive and dissipative characteristics of wave solutions of FD schemes were analysed. They found that the maximum resolvable wavenumbers of compact schemes, which are implicit, were far higher than those of explicit schemes. Hence compact FD schemes are of particular interest for CAA applications. Colonius and Lele [53] also showed that when centred schemes were used for hyperbolic systems of linear first-order partial differential equation (PDE), they disperse and are non-dissipative. This dispersion error can be minimised by performing Fourier analysis [36, 81]. Hence a compact centred FD scheme can be optimised. Upwind FD schemes are numerically stable since they are all dissipative. However, they are not as suitable for CAA as compact centred FD scheme since they lead to significant dissipation error of the highest resolved wavenumbers. Hence, high-order optimised compact centred FD schemes are very suitable for CAA problems, which demand long time precision of the numerical solution.

There are compact FD schemes with higher-order accuracy available. However, it was shown by Kim [36] that increasing the resolution capability rather than the truncation order could enhance the overall accuracy more effectively. Hence, as long as the compact scheme is optimised for the highest spectral resolution, the difference between tenth-order and fourth-order compact schemes is negligible. In the next sub-section, some issues of using high-order compact FD schemes will be discussed briefly.

3.1.2 Issues of High-order Compact FD Schemes

Colonius and Lele [53] conducted an analysis of the wave solutions of FD schemes and showed that for all centred schemes at a given frequency, there were two solutions to the dispersion relation. The long-wavelength solution was well resolved, it was called the *smooth* solution, and it approached the solution to the original PDE. The short-wavelength solution was poorly resolved, and it propagated with a group velocity of the wrong sign. The short wavelength solution was commonly known as the *spurious* solution. On the contours of numerical results, these spurious solutions showed up with a sawtooth or zigzag appearance since the Fourier component varied rapidly between the grid points [53].

Practical CAA problems have many features that can trigger the growth of the short-wavelength spurious solution. For example the body-fitted grids are always non-uniform. Even for problems without any solid surface, it is desirable to have a finer mesh in the source region than in the acoustic field since the sound wavelength is large compared to the source spatial scale [53]. Hence it is common

that meshes are non-smooth and contain regions of stretching, in which spurious waves can develop. BC can also lead to a similar growth of the spurious solution.

When the Euler or N-S equations are discretised by high-order compact centred FD schemes, they are non-dissipative. The non-linear instabilities due to the spurious solution can grow without bound if untreated, and lead to large errors or even solution failure. Hence stabilising techniques such as filtering, artificial viscosity and artificial dissipation are crucial in enforcing stability while retaining the advantages of high-order FD schemes over low-order ones. The current study employs sixth-order low-pass filters to enforce numerical stability. Before discussing the filters used in more details, the optimisation strategy for the interior and boundary schemes will first be explained briefly in the next sub-section.

3.1.3 Optimisation of the Interior and Boundary FD Schemes

The truncation order and the resolution of the schemes are analysed by the use of Taylor series expansion and Fourier Transform respectively. We will first look at the interior scheme and then the boundary scheme and the halo boundary scheme.

To derive the five coefficients, which are α, β and a_m for $m = 1, 2, 3$, in equation (3) of the interior scheme, Taylor series expansions are used to expand both sides of equation (3) about $x = x_i$. For a fourth-order accuracy, we need

$$1 + 2(\alpha + \beta) = 2\sum_{m=1}^{3} m a_m \tag{4}$$

$$3(\alpha + 2^2\beta) = \sum_{m=1}^{3} m^3 a_m. \tag{5}$$

Three more equations are required for the five unknown coefficients. To derive the remaining equations, first consider the continuous form of the equation of the interior scheme

$$\beta\bar{f}'(x-2\Delta x)+\alpha\bar{f}'(x-\Delta x)+\bar{f}'(x)+\alpha\bar{f}'(x+\Delta x)+\beta\bar{f}'(x+2\Delta x) = \frac{1}{\Delta x}\sum_{m=1}^{3} a_m \left[f(x+m\Delta x) - f(x-m\Delta x)\right].$$

By taking the Fourier Transform of this continuous equation, we obtain

$$j\bar{\kappa}\widetilde{f}(k)\left\{1 + 2\alpha\cos\kappa + 2\beta\cos(2\kappa)\right\} = 2j\widetilde{f}(k)\sum_{m=1}^{3} a_m \sin(\kappa m), \tag{6}$$

where $j = \sqrt{-1}$; k is the wavenumber; $\widetilde{f}(k)$ is the Fourier transform of $f(x)$; $\kappa = k\Delta x$ is the scaled wavenumber; and $\bar{\kappa} = \bar{k}\Delta x$ is the scaled pseudo-wavenumber, with $\bar{k}$ being the numerical wavenumber. Note that since the minimum solution wavelength that can be captured is $2\Delta x$, the maximum possible solution wavenumber is $\pi/\Delta x$. Hence the maximum possible range of κ for any

grid is $0 \leq \kappa \leq \pi$. $\bar{\kappa}$ is identical to κ up to certain value. The higher the spectral resolution of the scheme, the higher that value. Note that the L.H.S. of equation (6) represents the approximation made in the interior scheme; while the R.H.S. includes the Fourier transform of the exact objective function $f(x)$ and the exact scaled wavenumber. Now write $\bar{\kappa} = (1+\theta)\kappa$, where θ is some carefully chosen constant. Then the integrated error Φ, over a scaled wavenumber range of $0 \leq \kappa \leq r$, where r is certain value less than π, can be defined as

$$\Phi = \int_0^r \left\{ (1+\theta)\kappa \left[1 + 2\alpha\cos\kappa + 2\beta\cos 2\kappa\right] - 2\sum_{m=1}^{3} a_m \sin(\kappa m) \right\}^2 (\frac{\kappa}{r})^n d\kappa. \tag{7}$$

The minimum of Φ occurs when $d\Phi/d\sigma = 0$, where σ can be any of the five coefficients α, β and a_m for $m = 1, 2, 3$. Any three of the five $d\Phi/d\sigma = 0$ equations and equations (4) and (5) provide the five equations required to find the five coefficients. The optimisation of the differencing coefficients is driven by the minimisation of the resolution error, ϵ, defined as

$$\epsilon(\kappa) = \left| \frac{\bar{\kappa}(\kappa) - \kappa}{\kappa} \right|.$$

Kim [36] showed that the resolution error of the resulting scheme was insensitive to the choices of σ used in $d\Phi/d\sigma = 0$. Also, he showed that the current interior scheme had better spectral resolution characteristics than previous schemes which were optimised differently. Details of the calculation steps for the optimisation of the interior scheme can be found in a study by Kim [36].

The boundary closure strategy is very important to the current numerical strategy. There are many different kinds of boundary closure methods for FD schemes. Upwind/downwind FD schemes can be used at or near a computational boundary. However, these schemes are dissipative and will lead to loss of accuracy at a boundary. High-order one-sided difference closures can lead to instability. There are two important types of stability which should be considered when deriving FD boundary closures: the first is the Lax stability, which determines whether the solution remains bounded as the grid spacing $\Delta x \to 0$ at a fixed time; the second is the asymptotic stability, which requires that the error does not grow without bound [53]. It has been shown that clustering of grid points near computational boundaries could eliminate the instabilities associated with high-order one-sided schemes [53]. However, such approach would lead to a reduction in time step size due to the CFL stability condition, and hence a loss in computational efficiency.

For the current research, the boundary closure strategy is based on sophisticated extrapolation of the solutions beyond a boundary. Both the boundary and the halo boundary schemes use spline functions that are linear combinations of polynomials and trigonometric series. For the boundary scheme, from equation (3), it can be seen that extrapolation is required for the points $i = 0, 1, 2$ and $i = N-2, N-1, N$. For each of these points, the spline functions used is given by

$$g_i(x^*) = f_i + \sum_{m=1}^{N_A} p_m (x^*)^m + \sum_{m=1}^{N_B} \left[q_m \cos(\phi_m x^*) + r_m \sin(\phi_m x^*) \right],$$

and its derivative

$$g_i'(x^*) = \frac{dg_i(x^*)}{dx} = \frac{1}{\Delta x}\left\{\sum_{m=1}^{N_A} m p_m (x^*)^{m-1} - \sum_{m=1}^{N_B} \phi_m \left[q_m \sin(\phi_m x^*) - r_m \cos(\phi_m x^*)\right]\right\},$$

where $x^* = (x - x_i)/\Delta x$ is the non-dimensional coordinate from the point of interest x_i. The values of p_m, q_m and r_m are chosen such that the spline functions describe the interior profile of the objective function correctly. ϕ_m is used to optimise the resolution characteristics of the boundary scheme. To maintain fourth-order accuracy, $N_A = 4$ is required for the polynomials in the spline functions. The details of the optimisation procedure can be found in a study by Kim [36]. Seven-point stencils are also maintained for the boundary scheme, for example for the points $i = 0, 1, 2$,

$$\begin{aligned}
i = 0: &\quad \bar{f}_0' + \gamma_{01}\bar{f}_1' + \gamma_{02}\bar{f}_2' = \frac{1}{\Delta x}\sum_{m=0,\neq 0}^{6} b_{0m}(f_m - f_0) \\
i = 1: &\quad \gamma_{10}\bar{f}_0' + \bar{f}_1' + \gamma_{12}\bar{f}_2' + \gamma_{13}\bar{f}_3' = \frac{1}{\Delta x}\sum_{m=0,\neq 1}^{6} b_{1m}(f_m - f_1) \\
i = 2: &\quad \gamma_{20}\bar{f}_0' + \gamma_{21}\bar{f}_1' + \bar{f}_2' + \gamma_{23}\bar{f}_3' + \gamma_{24}\bar{f}_4' = \frac{1}{\Delta x}\sum_{m=0,\neq 2}^{6} b_{2m}(f_m - f_2).
\end{aligned}$$

It can be seen that the boundary scheme is non-central. For the halo boundary scheme, since halo point values are available, extrapolation is only required for the points $i = 0, 1$ and $i = N - 1, N$. Only one spline function

$$g(x^*) = \sum_{m=0}^{N_A} p_m (x^*)^m + \sum_{m=1}^{N_B} \left[q_m \cos(\phi_m x^*) + r_m \sin(\phi_m x^*)\right],$$

and its derivative

$$g'(x^*) = \frac{dg(x^*)}{dx} = \frac{1}{\Delta x}\left\{\sum_{m=1}^{N_A} m p_m (x^*)^{m-1} - \sum_{m=1}^{N_B} \phi_m \left[q_m \sin(\phi_m x^*) - r_m \cos(\phi_m x^*)\right]\right\},$$

is needed for the extrapolation. Note that $x^* = (x - x_0)/\Delta x$ and is the non-dimensional distance from a boundary. The spline function needs to match the halo and interior profile of the objective function. This constraint provides the equations needed to solve for the unknown coefficients p_m, q_m and r_m. Again, ϕ_m is used to optimise the resolution characteristics of the scheme and $N_A = 4$ to achieve fourth-order accuracy. The details of the optimisation procedure can be found in the study by Kim and Sandberg [37]. The resulting scheme is non-central and is based on eight-point stencils, for example the points $i = 0, 1$,

$$\begin{aligned}
i = 0: &\quad \bar{f}_0' + \gamma_{01}\bar{f}_1' + \gamma_{02}\bar{f}_2' = \frac{1}{\Delta x}\sum_{m=-3,\neq 0}^{4} b_{0m}(f_m - f_0) \\
i = 1: &\quad \gamma_{10}\bar{f}_0' + \bar{f}_1' + \gamma_{12}\bar{f}_2' + \gamma_{13}\bar{f}_3' = \frac{1}{\Delta x}\sum_{m=-3,\neq 1}^{4} b_{1m}(f_m - f_1).
\end{aligned}$$

Note that although the same letters are used for the designation of the coefficients of the boundary and

halo boundary schemes, the two sets of coefficients (each consists of γ's and b's) are totally different for the two schemes. In the next sub-section, the filters used in the current study will be explained briefly.

3.1.4 Compact Filters

In order to ensure numerical stability, compact discrete filters are used in the current study. Typically, the filter accuracy is chosen to be at least two orders higher than the FD schemes used [82]. Hence the use of sixth-order filters in the current study is appropriate. The basic filter applicable to the points away from any computational boundary is based on seven-point stencils and have a penta-diagonal matrix formulation similar to the interior FD scheme employed. It is called the *interior filter* in this thesis and is given by

$$\beta\widehat{\Delta}f_{i-2} + \alpha\widehat{\Delta}f_{i-1} + \widehat{\Delta}f_i + \alpha\widehat{\Delta}f_{i+1} + \beta\widehat{\Delta}f_{i+2} = \sum_{m=1}^{3} a_m(f_{i-m} - 2f_i + f_{i+m}), \tag{8}$$

where $\widehat{\Delta}f_i = \widehat{f_i} - f_i$ is the difference between the filtered objective function $\widehat{f_i}$ and the original objective function f_i. Equation (8) is in a fully differential form, which has some advantage in computational efficiency and numerical stability over an equation in terms of $\widehat{f_i}$ [38]. There are five unknown coefficients in equation (8). By using the Taylor's series expansion and the requirement of a sixth-order accuracy, two equations are derived. A filter transfer function, which represents the ratio of the filtered to the original value at a wavenumber k, is formed by using Fourier transform. The transfer function, $T(\kappa)$, is a function of the scaled wavenumber $\kappa = k\Delta x$. $T(\kappa) = 1$ means no filtering; while $T(\kappa) = 0$ is complete filtering. By considering the requirement of removing the irresolvable highest wavenumbers and the filtering performance in the high wavenumber regime, another two equations are derived. The last equation required is obtained by introducing a cut-off wavenumber, κ_C, at which $T(\kappa_C) = 0.5$. Then each of the five unknown filter coefficients can be written as a trigonometric function of κ_C, which can be chosen to suit different numerical and computational requirements. For the current differencing-filtering system, Kim showed that κ_C between 0.5π and 0.88π would ensure numerical stability [38].

The filter equation (8) cannot be applied directly to the points $i = 0, 1, 2$ and $i = N-2, N-1, N$. Hence boundary closure treatment is needed. Similar to the strategy applied to the boundary FD schemes, spline functions are used for the extrapolation of the original and the filtered functions beyond the boundaries. Details of the extrapolation procedure can be found in a study by Kim [38]. The resulting boundary filters for the points $i = 0, 1, 2$ are

$$\begin{aligned}
i = 0: &\quad \widehat{\Delta}f_0 + \gamma_{01}\widehat{\Delta}f_1 + \gamma_{02}\widehat{\Delta}f_2 = 0 \\
i = 1: &\quad \gamma_{10}\widehat{\Delta}f_0 + \widehat{\Delta}f_1 + \gamma_{12}\widehat{\Delta}f_2 + \gamma_{13}\widehat{\Delta}f_3 = 0 \\
i = 2: &\quad \gamma_{20}\widehat{\Delta}f_0 + \gamma_{21}\widehat{\Delta}f_1 + \widehat{\Delta}f_2 + \gamma_{23}\widehat{\Delta}f_3 + \gamma_{24}\widehat{\Delta}f_4 = \sum_{m=0,\neq 2}^{5} b_{2m}(f_m - f_2).
\end{aligned}$$

This type of boundary filter is non-central and is used for the domain boundaries, wall surfaces and block interfaces. Note also that the filter coefficients γ's and b's are completely different to the boundary FD scheme coefficients, which are designated by the same letters for convenience only in this thesis. All the filter coefficients are functions of the cut-off wavenumber κ_C only and can be adjusted easily for different problems.

Since the boundary FD schemes are non-central, the solution resolution at the boundary points ($i = 0, 1, 2$ and $i = N-2, N-1, N$) is lower than at the interior points, which use central FD scheme. Hence Kim [38] suggested a weighting factor ϵ, which reduced the cut-off wavenumber κ_C to lower values κ_{Ci} for the boundary points, i.e.

$$\kappa_{Ci} \quad = \quad \begin{cases} \kappa_C & \text{for} \quad 3 \leqslant i \leqslant N-3\,; \\ (1-\epsilon)\,\kappa_C & \text{for} \quad i = 2 \;\&\; N-2\,; \\ (1-2\epsilon)\,\kappa_C & \text{for} \quad i = 1 \;\&\; N-1\,; \\ (1-3\epsilon)\,\kappa_C & \text{for} \quad i = 0 \;\&\; N\,. \end{cases}$$

The introduction of ϵ has an effect on numerical stability. Kim showed that for the current FD-filtering system, the range of κ_C which led to stable numerical solutions reduced when ϵ was greater than about 0.085. Kim suggested $\epsilon = 0.085$ as the optimal value for the current schemes. This optimal value, which corresponds to the stability range $0.5\pi \leqslant \kappa_C \leqslant 0.88\pi$ mentioned before, is used in the current study.

For the sub-block interfaces across which the grid metrics are continuous, Kim and Sandberg [37] found that by applying the interior filters of equation (8) at the boundary points, the acoustic reflections at sub-block interfaces that would otherwise appear if non-central filters were used would be suppressed. To avoid a substantial increase in computational time, they suggested implementing the interior filters at the boundary points by using a predictor-corrector technique with the minimal, i.e. two, iterations. The predictor-corrector procedure starts at $n = 0$ with the initial guess of $\widehat{\Delta} f_i{}^{(n=0)} = 0$ at the halo points $i = -1, -2$ and $i = N+1, N+2$. Then by solving the penta-diagonal matrix system of equation (8), $\widehat{\Delta} f_i{}^{(n)}$ at the predictor and corrector steps, $n = 1$ and $n = 2$ respectively, can be found. The filtered solutions are then given by $\widehat{f}_i = f_i + \widehat{\Delta} f_i{}^{(2)}$. This filter is referred to as the *halo filter* in this thesis. Again, due to the lower resolution of the halo boundary scheme, lower cut-off wavenumbers κ_C should be used for the boundary points $i = 0, 1, 2$ and $i = N-2, N-1, N$. Kim and Sandberg suggested a smooth profile of the cut-off wavenumber about the sub-block interfaces. The wavenumber reduced from κ_C at the interior points smoothly to some value close to κ_C^* at points $i = 0$ and $i = N$. This smooth profile of cut-off wavenumber through the points $i = 0, 1, 2$ is

$$\begin{aligned} i = 0: \quad & \kappa_C = \kappa_C + (\kappa_C^* - \kappa_C)\,\sin^2(3\pi/7); \\ i = 1: \quad & \kappa_C = \kappa_C + (\kappa_C^* - \kappa_C)\,\sin^2(2\pi/7); \\ i = 2: \quad & \kappa_C = \kappa_C + (\kappa_C^* - \kappa_C)\,\sin^2(pi/7). \end{aligned}$$

Hence, there are three input parameters to the compact discrete filters used in the current study. They are the cut-off wavenumbers κ_C and κ_C^*, and the boundary weighting factor ϵ. The discrete filters are implemented only at the final stage of the fourth-order four-stage R-K time marching scheme, which is described in the next section.

3.2 Temporal Discretisation

An explicit fourth-order four-stage R-K time marching scheme is used to advance the solution in time in the current study. R-K time marching schemes have a semi-discrete formulation since the governing equations are discretised in space first, then the system of non-linear ordinary differential equation (ODE) obtained is integrated numerically. The general form of the ODE is

$$\frac{d\mathbf{Q}}{dt} = \mathbf{F}(\mathbf{Q}, t), \tag{9}$$

where $\mathbf{Q}$ is the solution vector, which is the discretised conservative variable vector for the current study. $\mathbf{F}$ contains the discretised spatial derivatives, which are the inviscid flux derivative vectors. These derivative vectors are non-linear vector function of $\mathbf{Q}$. t denotes time. To advance equation (9) in time, one can use implicit or explicit time marching methods. For implicit methods, the *R.H.S.* of equation (9) contains $\mathbf{Q}$ at the new time level. Hence additional iterations are required to solve the equation and the computational cost is higher. Hence for non-linear problem such as the current one, explicit time marching schemes are desirable. A family of widely used explicit semi-discrete formulation is the multi-stage R-K method. The current study uses an explicit fourth-order four-stage R-K scheme

$$\begin{aligned} \mathbf{Q}^a &= \mathbf{Q}^n + \mathbf{F}(\mathbf{Q}^0, t)dt/4; \\ \mathbf{Q}^b &= \mathbf{Q}^n + \mathbf{F}(\mathbf{Q}^a, t)dt/3; \\ \mathbf{Q}^c &= \mathbf{Q}^n + \mathbf{F}(\mathbf{Q}^b, t)dt/2; \\ \mathbf{Q}^{n+1} &= \mathbf{Q}^n + \mathbf{F}(\mathbf{Q}^c, t)dt/1, \end{aligned} \tag{10}$$

where n is an integer denoting the time level; $\mathbf{Q}^{n+1}$ and $\mathbf{Q}^n$ denote the solution at time $t = (n+1)\Delta t$ and $t = (n)\Delta t$ respectively, with Δt being the time step size; a, b and c indicate intermediate estimate of $\mathbf{Q}$ at the end of the first, second and third stage of the scheme respectively. A fourth-order R-K scheme is used since the FD schemes used are also fourth-order accurate. It is required since difference in the order of accuracy in the spatial and temporal discretisations can lead to dispersion error [82]. The time step size of the current simulation is determined by the Courant-Friedrichs-Lewy (CFL) condition

$$CFL = \Delta t U_\xi + \Delta t U_\eta + \Delta t U_\zeta,$$

where CFL is a dimensionless constant called the CFL number; Δt is the time step size; U_ξ, U_η and

U_ζ are the maximum phase speed of the characteristic wave propagation normal to the $\eta - \zeta$, $\xi - \zeta$ and $\xi - \eta$ planes in generalised coordinates respectively. Now the spatial and temporal discretisations have been explained. The BC used in the current study will be discussed in the next section.

3.3 Boundary Conditions

BC are required on the solid wall surfaces, domain boundaries and block and sub-block interfaces. The use of inappropriate BC can lead to the unbounded growth of spurious solution, which results in unacceptably large errors and even solution failure. Hence the application of proper BC is of tremendous importance to CAA. For the current study, an unsteady non-uniform incident flow has to be introduced into the computational domain. This poses a challenge as the BC must allow the mean velocity profile and the incident disturbances to be specified, and at the same time allowing the outgoing characteristic waves to exit the domain without producing non-physical reflections.

There is a class of BC based on the Euler equations linearised about a relatively uniform flow. These BC are known as the linearised BC. For the computational domain boundaries, linearised BC such as the radiation BC might be used. The radiation BC is based on the assumption that the domain boundaries are located far away from the source region. Hence, asymptotic solutions of the linearised Euler equations for the propagating vortical, entropic and acoustic disturbances at large distance from their source can be used to specify the BC. Some inflow and outflow BC based on this approach have been derived [53, 83]. However, the accuracy reduces when the domain is not large enough. Large domain might require a much larger number of grid points, particularly for cases that involve high-frequency gusts. A general problem of these linearised BC is that their accuracy degrades significantly whenever non-linearity presents in the flow due to excessive non-linear reflections [53].

In an one dimensional flow, accurate non-linear and non-reflecting BC can be derived from the classical method of characteristic solution [53]. By writing the governing equations in terms of the characteristic variables, characteristic waves on the $x - t$ plane can be identified. BC are applied to the incoming waves, which can be identified by the sign of the convection velocity of the waves through the boundaries. Thompson [84] proposed that this approach could be used as an approximation in a multi-dimensional flow. He wrote the conservative form of the Euler equations in the characteristic form. BC were derived by specifying values to the characteristic convection term $\mathbf{L}$ corresponding to the fluxes normal to the boundaries. The challenge is in the specification of $\mathbf{L}$. One way is to use the local one-dimensional inviscid (LODI) approach. In this approach, the source terms of the characteristic wave equations, which consist of the transverse and viscous terms of the N-S equations, are ignored. The LODI system of equations can be used to specify inflow and outflow conditions. However, problems arise when strong vortices pass through the boundaries [34]. Moreover, the drifting of time-averaged pressure from the freestream value is also an issue. [34, 53].

The current study uses a form of characteristic BC called the generalised characteristic BC

(GCBC) based on the works of Kim and Lee [34, 35]. GCBC does not use the LODI assumption. All the source terms of the governing equations are included. Even with non-reflecting GCBC, there would still be acoustic reflections from the boundaries. To attenuate these non-physical reflections, sponge zone (also referred to as buffer zone/layer in some publications) BC is used in conjuction to GCBC along the edges of the computational domain. In the next sub-section, the sponge zone technique used will be discussed.

3.3.1 Sponge Zone BC

Sponge zone techniques can be used to derive both inflow and outflow BC [53]. They are efficient for both inflow forcing and outflow damping. For this type of BC, the computational domain is divided into two parts: the physical domain, in which the physical phenomena are simulated; and the surrounding sponge zone, where a special treatment such as artificial dissipation, increased physical viscosity, modified convection speeds or artificial damping is applied. The simplest treatment is the use of artificial linear damping. In the conventional sponge technique, this involves an additional source term, $\sigma(q - q_{\text{ref}})$, to the R.H.S. of the governing equations. Here σ is a free parameter to control the strength of forcing/damping; q is a flow variable and q_{ref} is the reference solution desired in the sponge zone. Usually σ blends smoothly from zero in the physical domain to some positive value at the outer boundaries of the sponge zone, where the damped disturbances interact with an artificial BC. Even with the use of non-reflecting BC, there would still be reflected disturbances. The sponge zone provides damping to these reflected disturbances as they propagate back towards the physical domain. In this way, the sponge zone BC helps in further minimising the error caused by the reflected disturbances.

The sponge zone technique discussed here is similar to the perfectly matched layer (PML) BC in that they both require a layer of grid points adjacent to the edge of the computational domain. However, the PML BC are based on the analytical solutions of the linearised Euler equations. For the PML approach, the fluid properties within the layer are altered such that waves propagating in all directions are forced to decay [53]. Hence a perfect transmission with no reflection is ensured [85]. Variable/eigenvalue splitting, which increases the computational cost, is required to accomplish this. Furthermore, there are known stability problems with the PML BC [53], and the range of applications of this type of BC is limited.

The use of the conventional sponge zone BC, in contrast to the PML approach, is widespread. Freund proposed the use of sponge zone for the inflow and outflow regions, and has tested his outflow condition by simulating the translation of a zero circulation vortex across a 2D domain [86]. He compared the performance of the sponge zone technique against the local characteristic BC of Thompson, and showed that the sponge zone BC was vastly superior. Freund later used the sponge technique in the inflow zone to drive the solution towards the target in his study of noise source in a low-Re turbulent jet [87]. Bodony [85] analysed the convergence rate, the reflected wave absorption capability and the forcing properties of the sponge zone technique. His investigation considered the

introduction of acoustic waves and instability waves into the computational domain. Bodony and Lele [88] utilised sponge zone around all boundaries to absorb the outgoing disturbances and to introduce controlled disturbance at the inflow boundary to investigate the noise from cold and heated turbulent jets. These existing publications, however, are limited to unbounded domains with no solid body included. The present work aims to utilise sponge zone BC in the direct computation of AGI noise on a body-fitted structured multi-block grid around a 2D or 3D aerofoil. A newly modified form of the sponge technique, referred to as the *new sponge BC* herein, is utilised in the current study.

The difference between the conventional and the new sponge BC will now be discussed. If the conventional sponge zone technique is used to impose the gust velocity, the additional source term to the R.H.S. of the governing equation (2) is given by

$$\mathbf{S}_{\text{old}} \quad = \quad \sigma(\mathbf{Q}-\mathbf{Q}_{\text{ref}}) \quad = \quad \sigma \begin{pmatrix} \rho-\rho_\infty \\ \rho u-\rho_\infty u_{\text{gust}} \\ \rho v-\rho_\infty v_{\text{gust}} \\ \rho w-\rho_\infty w_{\text{gust}} \\ \rho e-\rho_\infty e_{\text{gust}} \end{pmatrix},$$

with

$$e_{\text{gust}} = \frac{p_\infty}{(\gamma-1)\rho_\infty} + \frac{{u_{\text{gust}}}^2+{v_{\text{gust}}}^2+{w_{\text{gust}}}^2}{2},$$

where $\sigma=\sigma(x,y,z)$ is the sponge damping coefficient; suffices ∞ and *gust* indicate freestream values and the imposed gust properties respectively. The aims of the additional source term are to force the density and pressure to their ambient values, and to force the velocity to some user-defined gust velocity function within the sponge zone. For 2D and 3D cases with spanwise periodic BC, $\sigma=\sigma(x,y)$ and its spatial variation, with smooth blending over the corners, is given by

$$\sigma(x,y) = \sigma_0 \frac{1+\cos[\pi A(x)B(y)]}{2},$$

for

$$x\in[x_{\min},x_{\max}] \quad \& \quad y\in[y_{\min},y_{\max}];$$

with

$$\begin{cases} A(x) = 1-\max[1-(x-x_{\min})/L_S,0]-\max[1-(x_{\max}-x)/L_S,0], \\ B(y) = 1-\max[1-(y-y_{\min})/L_S,0]-\max[1-(y_{\max}-y)/L_S,0]. \end{cases}$$

σ is zero in the physical domain and grows smoothly within the sponge zone to some specified maximum, denoted by σ_0, at the domain outer boundaries. σ_0 and the width of the sponge zone, denoted by L_S, are free parameters and have to be determined by parametric studies. A typical profile of $\sigma(x,y)/\sigma_0$ for the conventional sponge zone is plotted in Figure 1. The black dashed lines indicate the approximate boundaries between the physical domain and the sponge zone.

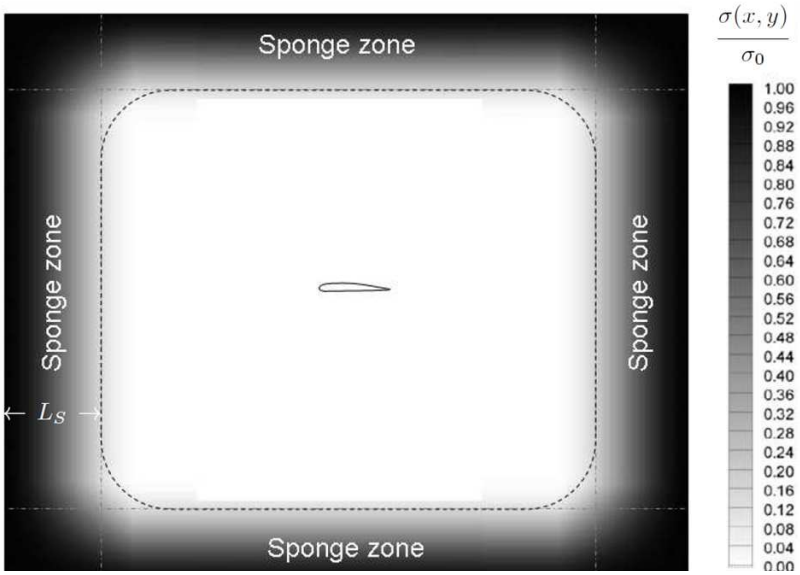

Figure 1: Conventional sponge BC damping coefficient ratio profile

The *new* sponge BC used in the current study is different to the conventional ones in two ways [33]. First, the last forcing term replaces total energy with pressure, which is one of the flow variable vector elements q. This modification is made since the total energy forcing in the conventional sponge BC overrides the density and velocity forcings that have already been specified by the other equations. Second, a weighting factor W has been applied to the velocity forcing terms *only*, while the density and pressure forcings maintain the original profile. W modifies the profile for velocity forcings such that the damping strength is the strongest at the upstream inflow boundary and diminishes smoothly to zero at a specified x location downstream of the inflow boundary. This modification is motivated by the consideration that the velocity distribution downstream of the aerofoil no longer follows the imposed gust function. Hence excessive constraint on the outflow condition is avoided. The new sponge BC forcing term in this study is represented by

$$\mathbf{S}_{\text{new}} = \sigma \begin{pmatrix} \rho - \rho_\infty \\ W(\rho u - \rho_\infty u_{\text{gust}}) \\ W(\rho v - \rho_\infty v_{\text{gust}}) \\ W(\rho w - \rho_\infty w_{\text{gust}}) \\ p - p_\infty \end{pmatrix},$$

with

$$W = \begin{cases} W(x) & \text{for} \quad x_{\min} \leqslant x \leqslant x_{\min} + \phi L_{\text{d}}\,; \\ 0 & \text{otherwise,} \end{cases} \tag{11}$$

where

$$W(x) = \frac{1}{2}\left\{\cos\left[\frac{\pi(x - x_{\min})}{\phi L_{\text{d}}}\right] + 1\right\},$$

where $x_{\min}$ is the minimum x, at which the inflow boundary is situated; L_{d} is the length of the

domain along the x direction; ϕ is a free parameter and $0 \leqslant \phi \leqslant 1$. Different $W(x)$ can be used as long as it varies smoothly from unity at the inflow boundary to 0 at some x location downstream. σ blends smoothly from zero in the physical domain to some positive value σ_0 at the outer boundaries of the sponge zone, where non-reflecting GCBC [34, 35] are applied. The sponge zone combined with the non-reflecting GCBC effectively removes unwanted wave reflections. Figure 2 shows an example of the profile of $W(x)\sigma(x, y)/\sigma_0$ for the velocity forcings with $\phi = 0.5$.

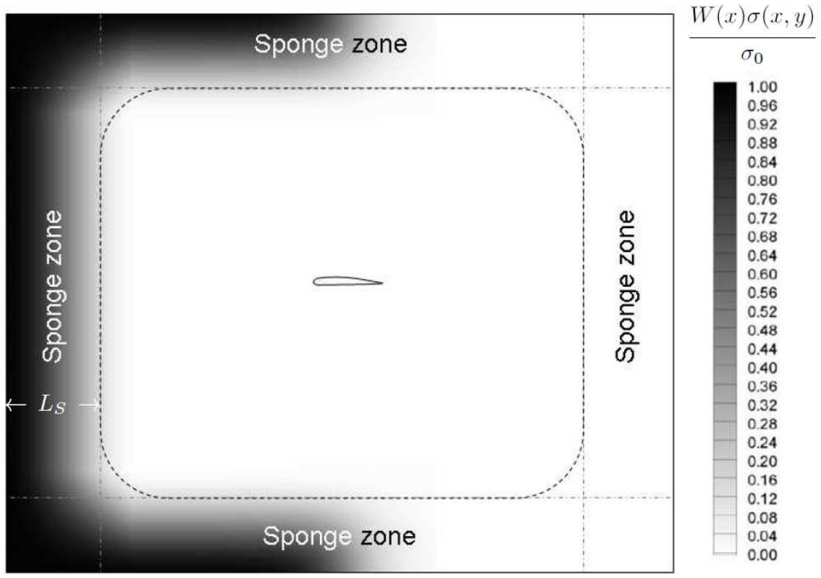

Figure 2: New sponge BC damping coefficient profile for velocity forcing

As a summary, the new sponge BC requires three free parameters: the maximum damping coefficient σ_0, the sponge zone thickness L_S and the velocity forcing length ratio parameter ϕ. The values of these three parameters were determined in the previous study [33]. In the next sub-section, the GCBC used in the current study will be discussed.

3.3.2 Generalised Characteristic BC

The artificial BC applied along the outside edges of the sponge zone is the GCBC [34]. This type of BC is also used for the solid wall surfaces [35] and the block interfaces across which the grid metrics are discontinuous. The GCBC is based on transforming the governing Euler or N-S equations, which are written in strong conservative form in generalised coordinates (ξ, η, ζ), into a generalised characteristic form in the direction normal to the boundary concerned. This generalised characteristic equation is in the form of a quasi-linear wave equation with a source term. The BC can be derived by considering the direction of propagation of the characteristic waves. To derive the GCBC, the governing equation (2) first needs to be written in generalised coordinates

$$\frac{\partial \mathbf{Q}}{\partial t} + \left(\frac{\partial \mathbf{E}}{\partial \xi}\xi_x + \frac{\partial \mathbf{F}}{\partial \xi}\xi_y + \frac{\partial \mathbf{G}}{\partial \xi}\xi_z\right) + \left(\frac{\partial \mathbf{E}}{\partial \eta}\eta_x + \frac{\partial \mathbf{F}}{\partial \eta}\eta_y + \frac{\partial \mathbf{G}}{\partial \eta}\eta_z\right) + \left(\frac{\partial \mathbf{E}}{\partial \zeta}\zeta_x + \frac{\partial \mathbf{F}}{\partial \zeta}\zeta_y + \frac{\partial \mathbf{G}}{\partial \zeta}\zeta_z\right) = 0.$$

Then, rearrange this equation and divide both sides by the transformation Jacobian J

$$\frac{1}{J}\frac{\partial \mathbf{Q}}{\partial t}+\frac{1}{J}\left(\frac{\partial \mathbf{E}}{\partial \xi}\xi_x+\frac{\partial \mathbf{F}}{\partial \xi}\xi_y+\frac{\partial \mathbf{G}}{\partial \xi}\xi_z\right)+\frac{1}{J}\left(\frac{\partial \mathbf{E}}{\partial \eta}\eta_x+\frac{\partial \mathbf{F}}{\partial \eta}\eta_y+\frac{\partial \mathbf{G}}{\partial \eta}\eta_z\right)+\frac{1}{J}\left(\frac{\partial \mathbf{E}}{\partial \zeta}\zeta_x+\frac{\partial \mathbf{F}}{\partial \zeta}\zeta_y+\frac{\partial \mathbf{G}}{\partial \zeta}\zeta_z\right)=0,$$

with

$$J \quad = \quad |\partial(\xi,\eta,\zeta)/\partial(x,y,z)| \quad = \quad x_\xi(y_\eta z_\zeta - y_\zeta z_\eta)+x_\eta(y_\zeta z_\xi - y_\xi z_\zeta)+z_\xi(y_\xi z_\eta - y_\eta z_\xi).$$

Now, consider

$$\frac{\partial \widehat{\mathbf{E}}}{\partial \xi}+\frac{\partial \widehat{\mathbf{F}}}{\partial \eta}+\frac{\partial \widehat{\mathbf{G}}}{\partial \zeta},$$

where $\widehat{\ }$ indicates division by J, and $\widehat{\mathbf{E}}$, $\widehat{\mathbf{F}}$ and $\widehat{\mathbf{G}}$ are defined as

$$\begin{aligned}\widehat{\mathbf{E}} &= (\xi_x E+\xi_y F+\xi_z G)/J;\\ \widehat{\mathbf{F}} &= (\eta_x E+\eta_y F+\eta_z G)/J;\\ \widehat{\mathbf{G}} &= (\zeta_x E+\zeta_y F+\zeta_z G)/J.\end{aligned} \tag{12}$$

By using the metric identities

$$\begin{aligned}(\widehat{\xi_x})_\xi+(\widehat{\eta_x})_\eta+(\widehat{\zeta_x})_\zeta &= 0;\\ (\widehat{\xi_y})_\xi+(\widehat{\eta_y})_\eta+(\widehat{\zeta_y})_\zeta &= 0;\\ (\widehat{\xi_z})_\xi+(\widehat{\eta_z})_\eta+(\widehat{\zeta_z})_\zeta &= 0,\end{aligned}$$

and expending equations (12), it can be shown that

$$\frac{\partial \widehat{\mathbf{E}}}{\partial \xi}+\frac{\partial \widehat{\mathbf{F}}}{\partial \eta}+\frac{\partial \widehat{\mathbf{G}}}{\partial \zeta}=\frac{1}{J}\left(\frac{\partial \mathbf{E}}{\partial \xi}\xi_x+\frac{\partial \mathbf{F}}{\partial \xi}\xi_y+\frac{\partial \mathbf{G}}{\partial \xi}\xi_z\right)+\frac{1}{J}\left(\frac{\partial \mathbf{E}}{\partial \eta}\eta_x+\frac{\partial \mathbf{F}}{\partial \eta}\eta_y+\frac{\partial \mathbf{G}}{\partial \eta}\eta_z\right)+\frac{1}{J}\left(\frac{\partial \mathbf{E}}{\partial \zeta}\zeta_x+\frac{\partial \mathbf{F}}{\partial \zeta}\zeta_y+\frac{\partial \mathbf{G}}{\partial \zeta}\zeta_z\right).$$

For non-moving grid, J is constant in time. Hence the governing Euler equation can be written in strong-conservative form in the generalised coordinates as

$$\frac{\partial \widehat{\mathbf{Q}}}{\partial t}+\frac{\partial \widehat{\mathbf{E}}}{\partial \xi}+\frac{\partial \widehat{\mathbf{F}}}{\partial \eta}+\frac{\partial \widehat{\mathbf{G}}}{\partial \zeta}=0. \tag{13}$$

Now, consider ξ as the direction normal to a computational boundary. First, the transverse generalised inviscid flux derivatives are moved to the R.H.S. of equation (13). Then, expanding the normal flux derivative, we get

$$\frac{\partial \widehat{\mathbf{Q}}}{\partial t}+\frac{1}{J}\left(\xi_x\frac{\partial \mathbf{E}}{\partial \xi}+\xi_y\frac{\partial \mathbf{F}}{\partial \xi}+\xi_z\frac{\partial \mathbf{G}}{\partial \xi}\right)=-\left[E\frac{\partial}{\partial \xi}\left(\widehat{\xi_x}\right)+F\frac{\partial}{\partial \xi}\left(\widehat{\xi_y}\right)+G\frac{\partial}{\partial \xi}\left(\widehat{\xi_z}\right)+\frac{\partial \widehat{\mathbf{F}}}{\partial \eta}+\frac{\partial \widehat{\mathbf{G}}}{\partial \zeta}\right]$$

The R.H.S. terms can be denoted by $\mathbf{S}_{c1}$. The flux term on the L.H.S. of this equation is then re-written as

$$\frac{1}{J}\frac{\partial \mathbf{Q}}{\partial t} + \frac{1}{J}\left(\xi_x \frac{\partial \mathbf{E}}{\partial \mathbf{Q}} + \xi_y \frac{\partial \mathbf{F}}{\partial \mathbf{Q}} + \xi_z \frac{\partial \mathbf{G}}{\partial \mathbf{Q}}\right)\frac{\partial \mathbf{Q}}{\partial \xi} = \mathbf{S}_{c1}.$$

Note that $(\xi_x \partial \mathbf{E}/\partial \mathbf{Q} + \xi_y \partial \mathbf{F}/\partial \mathbf{Q} + \xi_z \partial \mathbf{G}/\partial \mathbf{Q})$ is the *Flux Jacobian matrix*, denoted by K here. We then multiply this equation through by J and pre-multiply the equation by the transformation matrix from conservative to characteristic variables, P^{-1}, we obtain

$$P^{-1}\frac{\partial \mathbf{Q}}{\partial t} + P^{-1}KPP^{-1}\frac{\partial \mathbf{Q}}{\partial \xi} = P^{-1}J\mathbf{S}_{c1},$$

with

$$\delta \mathbf{R} = P^{-1}\delta \mathbf{Q},$$

where $\delta \mathbf{R}$ is the 3D characteristic variables vector. Finally, $P^{-1}KP = \Lambda$, where Λ is a 5×5 diagonal matrix whose diagonal elements are the eigenvalues of the Flux Jacobian matrix K, and write $P^{-1}J\mathbf{S}_{c1} = \mathbf{S}_c$, we get

$$\frac{\partial \mathbf{R}}{\partial t} + \Lambda \frac{\partial \mathbf{R}}{\partial \xi} = \mathbf{S}_c. \tag{14}$$

Equation (14) is the quasi-linear characteristic wave equation, which can be used to derive the GCBC for the boundary normal to the ξ direction. The idea behind the GCBC is to update the incoming characteristic waves. Hence, one would need to identify the direction of propagation of the characteristic waves in order to assign the BC. For that, we need to look at the diagonal elements of Λ, which can be written as a vector

$$\mathbf{\Lambda}_{diagonal} = \left[U, U, U, U + c\sqrt{{\xi_x}^2 + {\xi_y}^2 + {\xi_z}^2}, U - c\sqrt{{\xi_x}^2 + {\xi_y}^2 + {\xi_z}^2}\right]^T,$$

where c is the speed of sound; $U = \xi_x u + \xi_y v + \xi_z w$ is the normal velocity along the ξ direction, with u, v and w being the flow velocity components in the Cartesian x, y and z directions respectively. It can be seen that the entropic (first) and the vortical (second and third) wave-modes are propagating at the normal velocity U with the flow. For supersonic cases, the two acoustic modes (fourth and fifth modes) are propagating along the same direction as the flow. For subsonic cases, however, the convection speed of the fifth mode $(U - c({\xi_x}^2 + {\xi_y}^2 + {\xi_z}^2)^{1/2})$ is negative. Hence, it is propagating in the opposite direction to the flow.

Now the implementation procedure of the GCBC is explained. We concentrate on the characteristic convection term $\mathbf{L}$ on the L.H.S. of equation (14), since it is this term that needs to be updated at the boundaries. During the simulation, this term can be calculated by

$$\mathbf{L} = JP^{-1}\left\{\frac{\partial\widehat{\mathbf{E}}}{\partial\xi} - \left[E\frac{\partial}{\partial\xi}\left(\frac{\xi_x}{J}\right) + F\frac{\partial}{\partial\xi}\left(\frac{\xi_y}{J}\right) + G\frac{\partial}{\partial\xi}\left(\frac{\xi_z}{J}\right)\right]\right\},$$

with

$$\mathbf{L} = \Lambda\frac{\partial\mathbf{R}}{\partial\xi}.$$

The values of L_i, with $i = 1, 2, 3, 4, 5$ for each of the five modes, are updated according to the nature of the propagation of the wave-modes. Then the updated L, denoted by L^*, is used to re-calculate the normal flux derivative term $\partial\widehat{\mathbf{E}}/\partial\xi$, we obtain

$$\left(\frac{\partial\widehat{\mathbf{E}}}{\partial\xi}\right)^* = \frac{1}{J}PL^* + \left[E\frac{\partial}{\partial\xi}\left(\frac{\xi_x}{J}\right) + F\frac{\partial}{\partial\xi}\left(\frac{\xi_y}{J}\right) + G\frac{\partial}{\partial\xi}\left(\frac{\xi_z}{J}\right)\right].$$

The normal velocity U to the boundaries needs to be calculated for each R-K stage of the simulation. Then, depending on the sign of U, at the inflow and outflow boundaries, one can identify which of the first three modes, represented by L_1, L_2 and L_3 respectively, are incoming. Since the flow is subsonic in the current study, at the inflow boundaries, the fourth mode, which is an acoustic mode represented by L_4, is incoming; while the fifth mode, also an acoustic mode and is represented by L_5, is outgoing. At the outflow boundaries, L_5 is incoming and L_4 is outgoing. For the outer domain boundaries surrounding the sponge zone, L_i of all the incoming wave-modes are set to zero. Hence a type of non-reflecting GCBC is obtained. As explained before, there would still be reflected waves at the computational boundaries. These reflected waves are damped by the sponge zone. For the block interfaces across which the grid metrics are discontinuous, L_i of the incoming modes are updated using

$${L_i}^* = (L_i - S_{ci})|_{\text{neighbour}} + S_{\text{ci}},$$

where ${L_i}^*$ is the updated value of L_i; S_{ci} are the elements of the source term vector $\mathbf{S}_c$ in the quasi-linear characteristic wave equation (14); and suffix *neighbour* indicates values from the neighbouring block on the other side of the interface considered.

For the wall boundaries, the GCBC is based on the study by Kim and Lee [35]. This BC is derived by writing the quasi-linear characteristic wave equation (14) in primitive variables (u, v, w, ρ and p). The resulting equations in terms of the normal and transverse velocity are used to derive the equations for the wall BC, which imposes the no-penetration condition of flow through the solid wall and the slip/no-slip condition. Since the flow is inviscid in the current study, no-penetration of flow and slip condition are needed. Hence only the equation in terms of the normal velocity U is required. This equation only involves L_4 and L_5. Hence there is no need to update L_1, L_2 and L_3 for the inviscid wall BC. For the inflow boundaries, e.g. a left-sided wall, L_4 is updated by

$${L_4}^* = L_5 + S_{\text{c4}} - S_{\text{c5}} - 2\left.\frac{dU}{dt}\right|_{\text{wall}}. \tag{15}$$

While for the outflow boundaries, e.g. a right-sided wall, L_5 is updated by

$$L_5{}^* = L_4 - S_{c4} + S_{c5} + 2\frac{dU}{dt}\bigg|_{\text{wall}} . \tag{16}$$

S_{c4} and S_{c5} in these two equations are the source terms for the fourth and fifth acoustic modes respectively. $dU/dt|_{\text{wall}}$ is the wall pulsation term and is zero if the wall is stationary. Up to this point, the spatial and the temporal discretisations and the BC used in the current study have been explained. In the next section, some relevant inflow generation methods which can be incorporated eventually will be discussed.

3.4 The Inflow Generation Method

The aim of the current research is to investigate the effects of wavy leading edges on AGI noise. Hence eventually an unsteady non-uniform incident flow with certain physical features needs to be generated. There are many inflow generation methods, which can be divided into two categories: synthetic methods and recycling/rescaling methods [89]. In the recycling/rescaling approach, a velocity profile somewhere downstream of the inflow boundary is recycled and rescaled. Then, the resulting profile is reintroduced as the inflow. This act of recycling will introduce non-physical correlations associated with the recycling period. Nevertheless, this method is useful for many purposes. For example, it can be used to investigate the effects of upstream wings on the acoustic response of the downstream ones. One might also use the recycling/rescaling method to model the atmospheric boundary layer in an auxiliary simulation. Then store the flow field and prescribe it as the velocity profile in the inflow region via the sponge zone technique. However, this approach is computationally expensive.

Synthetic methods require the use of some model to prescribe the velocity fluctuation about a mean flow profile [89]. One popular example of synthetic method is based on the digital filtering (DF) of random data, which was first developed by Klein et al. [64]. Their DF method of inflow generation aims to reproduce the first- and second-order one-point statistics and a locally given autocorrelation function. However, the full autocorrelation function is often unknown. Hence Klein et al. assumed the autocorrelation to be of a Gaussian shape, and that only the length scale needed to be prescribed. The filter coefficients were then derived by using their relation with the autocorrelation function [64]. At each time step, a 3D digital filter was applied to three sets of 3D random data, one set for each velocity component. Then, a slice of 2D filtered data for each velocity component was produced. These were then imposed on the inflow $y-z$ plane. Cross correlations between different velocity components might be introduced by using a transformation proposed by Lund et al. [64, 90]. Each set of random data was then updated by removing the first $y-z$ plane of data at the most negative x-location, then shifting the remaining data in the negative x-direction, and introducing a new $y-z$ plane of random data to the last plane. Then the filtering process was repeated for each time step.

Xie and Castro [91] further improved the efficiency of the DF method of Klein et al.. They

applied a 2D digital filter to three sets of 2D random data. A slice of 2D filtered data was produced for each velocity component at each time step. By correlating the new 2D field with the old one from the previous time step, a new slice of 2D data, whose space and time correlation functions were both of exponential form, was produced.

Since only a slice of $y - z$ plane velocity field is generated at each time step, the generated velocity fields by using the approaches of Klien et al. and Xie and Castro are not divergence-free. Ewert [63] used the DF approach in his random particle-mesh (RPM) method to produce divergence-free pseudo-turbulent velocity field for the study of aircraft slat noise. Instead of synthesizing velocity directly, stream-function which satisfied the divergence-free condition was generated. In his approach, a bundle of mean flow streamlines was introduced to a part of the domain known as the source patch, in which turbulence-related vortex sound sources originated. The streamlines started equidistantly in the most upstream location of the source patch. They then propagated downstream according to the local mean flow computed by a steady RANS simulation. Random values were assigned to discrete points, known as particles, along these streamlines. Digital filtering was applied to these points to achieve the desired statistics. Note that the filter kernel parameters had to be determined by a steady RANS computation as well. At each CAA time step, the particles convected downstream along the streamlines. Once the particles reached the end of the streamlines, they would be discarded. New particles with new random values were then added at the most upstream locations. Since the particles on the streamlines were not necessary the actual points on the CAA mesh, interpolations were required for the CAA calculations. The filtering and interpolations happened simultaneously. The velocity field were then obtained by computing the gradient of the resulting stream-function. A fast RPM (FRPM) approach had been developed by Ewert [65, 66]. In the FRPM, a Cartesian background mesh was used to store the mean flow quantities computed by the RANS simulation and the source strength. Instead of distinct streamlines, a cloud of evenly distributed particles over the background mesh was used. Linear interpolations were used to compute the particle velocity from the stored values at the vertices of the background cells which contained the particles. The particles were convected according to the local mean velocity. The RPM and FRPM methods have been applied directly to 2D simulations only [66, 68]. Work is still on-going for its direct applications to more complicated 3D geometries, which obviously will lead to a much more complicated and potentially costly implementation procedure.

The current study requires the inflow velocity field to be divergence-free. Hence the recent DF based approaches, although sophisticated, are not applicable. Therefore, attention is turned to the other main type of synthetic methods. These methods prescribe a form for the inflow structure but not its statistics. In this aspect, they are the opposite to the DF based methods. These methods are based on the superposition of harmonic or waveform functions. An example is the inflow generation method devised by Smirnov et al. [92], who aimed to produce a spatially developing inhomogeneous, anisotropic turbulent flows for particle tracking applications using LES. In their study, a flow field was generated as a superposition of harmonic functions. Independent numbers selected from normal distributions were used as the angular frequency and wavenumbers of each

harmonic. The amplitude of each mode was also constructed by these normally distributed numbers. Hence the flow field is not periodic in space and time. Then an orthogonal transformation tensor, which was used to transform the velocity correlation tensor to a diagonal matrix, and the diagonal elements of the transformed matrix were used to transform and scale the velocity field respectively. In this way, a flow field with the desired velocity correlation was produced. By the way the amplitudes of the modes were constructed, the velocity field produced was divergence-free for homogeneous turbulence. For inhomogeneous turbulence, it was nearly divergence-free since the correlation tensor was slowly varying in space in this case.

The current inflow generation method is based on the superposition of wave-modes. Each wave-mode is in the form of a general trigonometric function. For the j^{th} mode

$$u'_{ij} = A_{ij}\cos(k_{1j}x + k_{2j}y + \omega_j t) + B_{ij}\sin(k_{1j}x + k_{2j}y + \omega_j t), \tag{17}$$

where $i = 1, 2$ for the Cartesian x- and y-directions respectively; u'_{ij} represents the velocity perturbation along the i^{th} direction; k_{1j} and k_{2j} are the non-dimensional wavenumbers; $\omega_j = -k_{1j}M_\infty$ is the angular frequency for a wave travelling in the positive x-direction (from left to right), with M_∞ being the freestream Mach number; A_{ij} and B_{ij} are the amplitudes for the cosine and sine parts respectively. Note that the the x-direction is the streamwise direction, and the y-direction is vertical direction in the current study. The spanwise u'_{3j} component of the perturbed velocity is such that it cancels the generally non-zero divergence at every stage of the R-K time marching, i.e.

$$u'_{3j} = -\left(\frac{\partial u'_{1j}}{\partial x} + \frac{\partial u'_{2j}}{\partial y}\right) z. \tag{18}$$

This approach of imposing velocity perturbations will be referred to as the *first* approach herein. Note that the u'_{1j} and u'_{2j} components of the perturbed velocity only vary in the x- and y-directions. An alternative approach to impose the incident flow has perturbed velocity components that vary in the z-direction as well, i.e.

$$u'_{ij} = A_{ij}\cos(k_{1j}x + k_{2j}y + k_{3j}z + \omega_j t) + B_{ij}\sin(k_{1j}x + k_{2j}y + k_{3j}z + \omega_j t), \tag{19}$$

for $i = 1, 2$; with non-zero k_{3j} in general. Then for maintaining the divergence-free condition, the u'_{3j} component has to be

$$u'_{3j} = -\left(\frac{k_{1j}A_{1j} + k_{2j}A_{2j}}{k_{3j}}\right)\cos\Omega - \left(\frac{k_{1j}B_{1j} + k_{2j}B_{2j}}{k_{3j}}\right)\sin\Omega, \tag{20}$$

with $\Omega = (k_{1j}x + k_{2j}y + k_{3j}z + \omega_j t)$. This alternative approach will be known as the *alternative* approach from now on. At a first glance, the alternative approach is advantageous in that it is more general than the first approach. However, it will be shown later that when a gust prescribed by the alternative approach impinges upon a 3D aerofoil with straight leading edge, the AGI noise produced

within the computational domain reduces as the spanwise length of the domain increases. This might be the result of the spanwise variation of AGI noise due to the inclined wavefronts of $|u'|$ to the leading edge as seen on the $x - z$ plane. This apparent reduction of AGI noise due to increasing spanwise length of the domain can be avoided by using the first approach to prescribe gust. More regarding this will be shown and discussed in Chapter 5. Examples of the instantaneous contours of $|u'|$ of gusts due to the first and the alternative approaches are shown in Figure 3. In the next section, the grid generation method used will be explained.

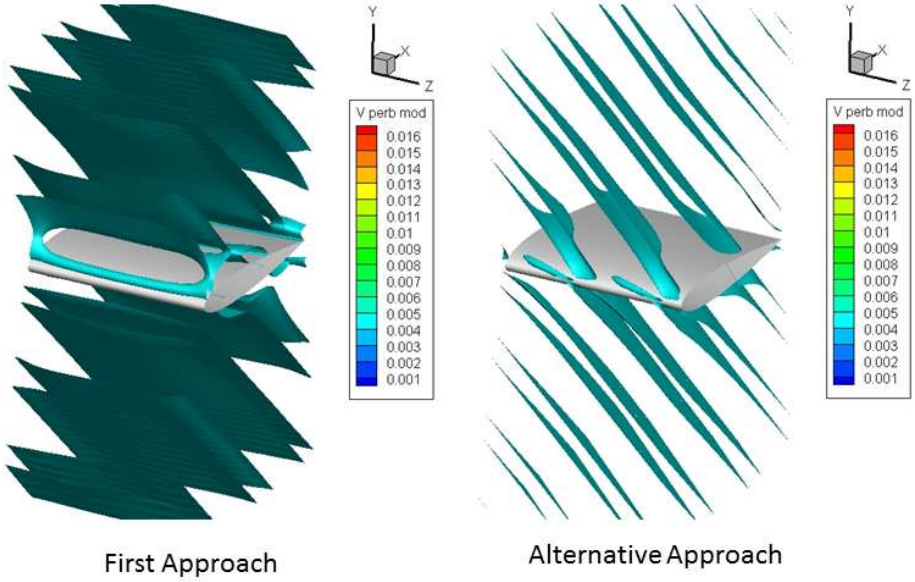

Figure 3: Examples of instantaneous contours of $|u'|$

3.5 The Grid Generation Method

The generation of structured grid around a complex geometry for the use of high-order compact FD schemes in CAA is one of the most challenging parts of the whole computational process. The first type of grid generation method for numerical studies were the coordinate transformation techniques, such as conformal mappings, shearings and stretchings [93]. However, these transformation techniques could not meet the demand as the complexity of the modelled geometries increased. Numerical grid generations, which involved solving a set of PDE [93], and multi-block technique were then developed to bypass this bottleneck. A multi-block strategy divides the domain into several smaller blocks or sub-domains. The grid metrics can be discontinuous about the block interfaces. Separate grids are generated in each of the blocks. The grid of a block is much simpler and can be generated by algebraic methods, such as transfinite interpolation [94]. It is common to use an algebraic method to generate the grid in a block, then smooth the grid by using an elliptic PDE solver. Such a strategy is utilised by commercial grid generation software like *Gridgen*. Much effort has been put into automatic grid generation, and a typical commercial grid generation software usually provides some automation. However, because of the difficulties in changing the interface positions and the arrangement and

connectivity of the blocks automatically without human input, the grid generation for structured multi-block grids remains a largely manual process.

There are many commercial software packages available for grid generation, such as *Gridgen*. They provide an interactive graphical user interface for researchers and engineers who are not specialised in grid generation. For conventional lower-order numerical methods used in other CFD areas, these commercial software packages provide a quick way to generate the grid. However, for CAA purposes, particularly when the governing equations are discretised by high-order compact centred FD schemes as in the current study, problems can arise. The discretised equations by such schemes are non-dissipative. As discussed in Section 3.1, it is common in CAA that grids are non-smooth and contain regions of stretching. Hence non-physical spurious waves can develop in these regions. If the quality of the grid is bad, for example part of the grid contains cells that are too skewed or have extreme aspect ratios, detrimental spread of spurious waves can occur even with the use of stabilizing techniques such as high-order compact filters. The main problem with the commercial packages is that even if the generated grid looks 'good' on the graphical user interface, it is very likely that there exist some undetectable 'bad' features that could lead to the spread of spurious solutions. Because of this, an 'in-house' algebraic grid generation method is used in the current study.

In the current study, a type of multi-block structured grid is used. In 2D, the grid around the modelled aerofoil consists of six blocks, which are arranged in a *H-topology*. This type of grid, shown in Figure 4, is often referred to as the *H-grid* or *H-mesh*, and can be deformed into a set of Cartesian grid lines. The mesh lines across the block interfaces are in general discontinuous.

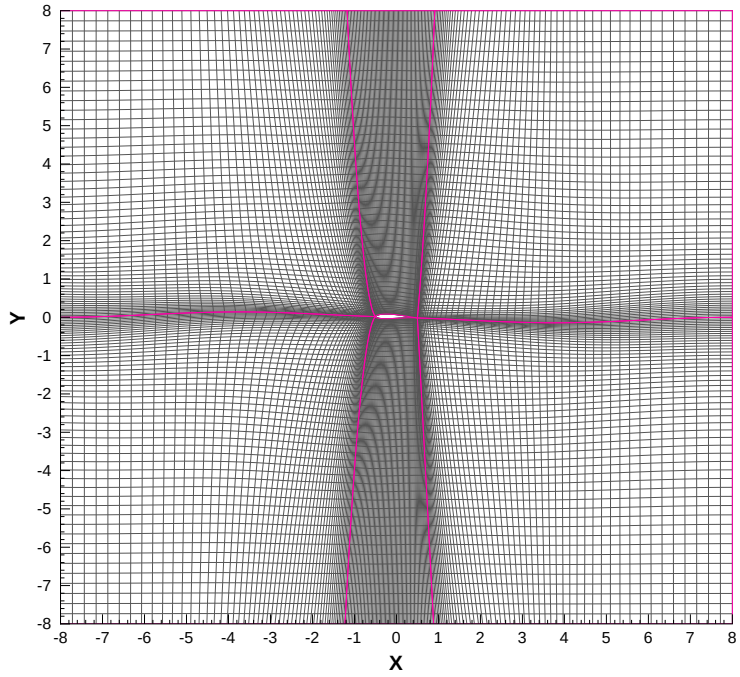

Figure 4: An example of the 2D grid used

The Cartesian coordinates of the points in a block can be written as functions of the generalised coordinates, for example $x(\xi)$. These functions are referred to as *grid functions* in this thesis. The motivation behind the current algebraic approach is to have smooth second derivatives of the grid functions, such as $d^2x/d\xi^2$, between all the points within each block. This requirement arises from the fact that in the governing Euler equations (13), there are derivatives such as $d(\xi_x)/d\xi$ in the inviscid flux terms. These derivatives are related to the second derivatives of grid functions by the way the metrics are defined. Hence if the second derivatives of grid functions are non-smooth between some points, spurious solutions will grow and spread from these points. Therefore, in addition to the basic requirement of smooth grid functions and their first derivatives, for example $dx/d\xi$, their second derivatives are required to be smooth as well.

Now, consider generating an 1D grid with $n+1$ grid points, so that $\xi = 0, 1, ..., n-1, n$. Two polynomials $x_1(\xi)$ and $x_2(\xi)$ are used to determine the grid points distribution. This allows the method to be more flexible in controlling the grid point spacing near the two ends of the domain. The first derivatives $dx/d\xi$ rather than the grid functions $x(\xi)$ are considered. The method can be illustrated more easily by plotting the first derivatives against ξ, as shown in Figure 5. Polynomials $x_1(\xi)$ and $x_2(\xi)$ are used to decide the grid point distribution from point 0 to m and m to n respectively. $dx/d\xi$ of the two polynomials are matched at point m. The value of $dx/d\xi$ where the two polynomials match, represented by c in Figure 5, are used to ensure that $d^2x/d\xi^2$ of the two polynomials at point m are the same. The grid point spacing at the two ends of the domain are calculated such that the two polynomials are connected at the same physical location $x(\xi = m)$. In this way, high quality grid point distribution along the block interfaces can be ensured. The mesh of a block can then be filled by interpolations. Adjustments of other variations such as grid cell skewness and aspect ratio are required after the provisional grid is generated. This usually involves changing the value of n and the grid spacings at the ends of the block boundary lines.

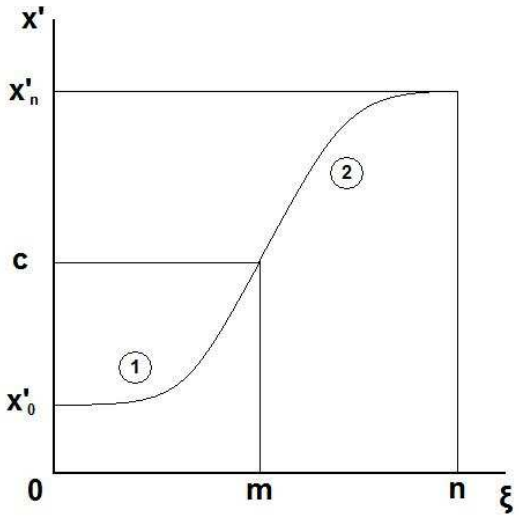

Figure 5: The two polynomials considered in the current algebraic grid generation method

By using the current grid generation strategy, the grid for a 3D aerofoil with a wavy leading edge can be generated. Note that the aerofoil shape is not changed by the changing chord length along the

span. An example of such grid is shown in Figure 6. The real challenge in terms of grid generation for the current study is the generation of a half low aspect ratio wing with a tip. For this purpose, using the current grid generation method as the basis, a *Fortran 90* code was written. The tip geometry needs to change smoothly in all parts of the grid. This is particularly challenging to achieve for the transition from the rounded leading edge to the sharp trailing edge, and the change of thickness from the main span to the edge of the tip. Any non-smooth feature will definitely lead to computational failure. The planform shape of the tip is elliptical. The organization of the natural blocks needs to be changed to achieve a smooth grid with high quality. Figure 7 shows the grid structure of the tip. The special block which is crucial to the success of the grid is also shown in the figure. Any aerofoil can be used for the wing main span. Figure 8 shows the smooth transition from the leading edge to trailing edge at the tip. NACA 0005 is the aerofoil used in this example.

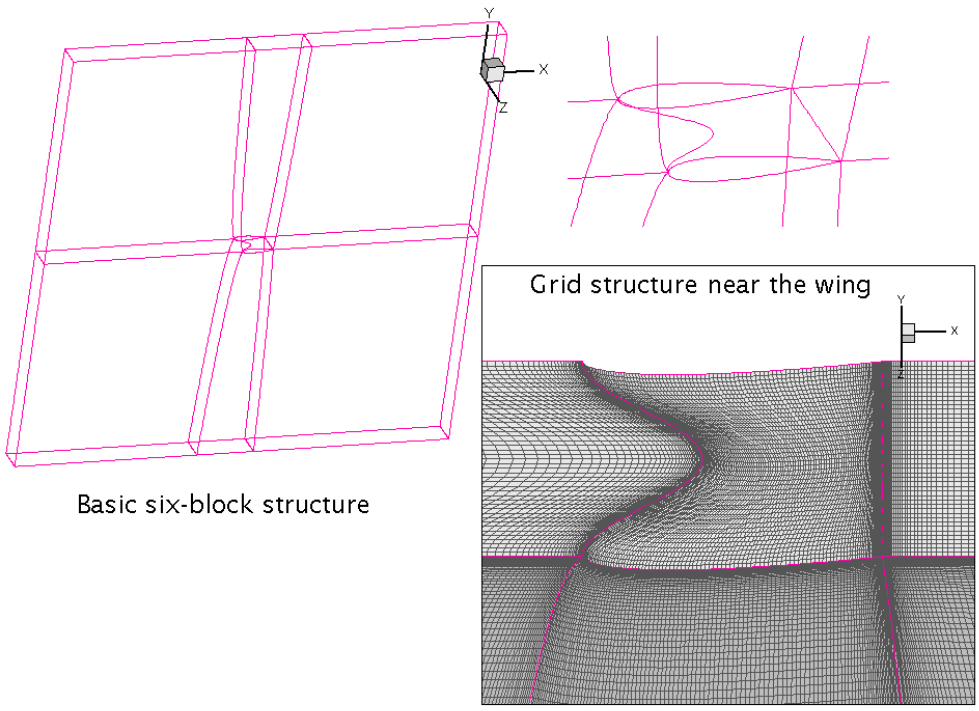

Figure 6: An example of the infinite-span wing grid with wavy leading edge

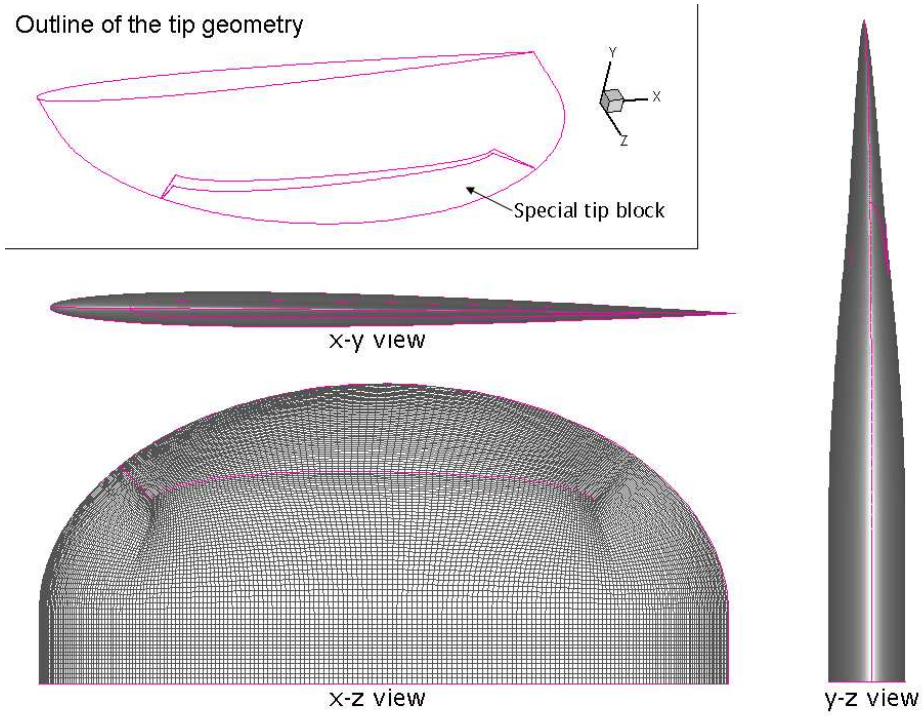

Figure 7: Tip grid structure

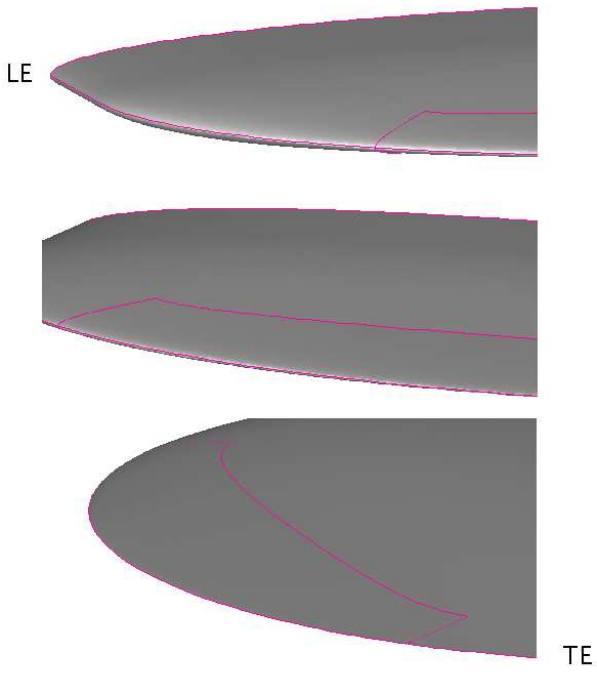

Figure 8: Smooth transition from the leading edge to the trailing edge at the tip

4 Code Validations

In this chapter, the results computed by the current *Fortran 90* code, parallelised with the use of the MPI library, will be validated. Four validation studies will be presented. In Section 4.1, a benchmark problem regarding the acoustic responses of Joukowski aerofoils under a simple periodic gust is chosen from the Third [55] and the Fourth [56] CAA Workshops for comparison purposes. Then in Section 4.2, the theoretical results proposed by Myers and Kerschen [24] on AGI noise will be compared with the current numerical results. These two validation studies involve 2D aerofoils. The last two validation cases presented in this chapter involve 3D aerofoils. In Section 4.3, the computed lift curves, which are plots of the total lift coefficient C_L versus *alpha*, for 3D NACA 0015 aerofoils are compared to those measured by Sheldahl and Klimas [95] experimentally. Finally in Section 4.4, qualitative comparisons of the computed 3D aerofoil surface mean pressure and velocity distributions with the mean aerodynamic features reported in the literature for wavy leading edges are made.

4.1 Validations by a CAA Benchmark Problem

The first validation study employs two published sets of solutions to category 3 problem 1 of the Third [55] and the Fourth [56] CAA Workshops as references. This problem investigates numerically the acoustic response of a Joukowski aerofoil to an impinging 2D periodic vortical gust. Two cases are studied: *case 1* with a symmetric Joukowski aerofoil at zero α; and *case 2* with a Joukowski aerofoil with 2% camber to chord ratio at 2° α. All the Joukowski aerofoils considered in this problem have 12% thickness to chord ratio. The mean flow at ∞ is defined as

$$\begin{aligned}
&\rho_\infty = 1.0;\\
&p_\infty = \rho_\infty^\gamma/\gamma = 1/1.4;\\
&a_\infty = \sqrt{(\gamma p_\infty)/\rho_\infty} = 1.0;\\
&u_\infty = M_\infty a_\infty = 0.5;\\
&v_\infty = 0.
\end{aligned}$$

The form of the gust imposed is given by

$$\begin{aligned}
u_{\text{gust}} &= -\epsilon u_\infty \frac{\sqrt{2}}{2} \cos\left[k(x+y-u_\infty t)\right];\\
v_{\text{gust}} &= \epsilon u_\infty \frac{\sqrt{2}}{2} \cos\left[k(x+y-u_\infty t)\right],
\end{aligned} \tag{21}$$

where $\epsilon = 0.02$; and k is the reduced frequency, which is defined in the original benchmark problem by

$$k = \frac{\omega L}{2u_\infty}, \tag{22}$$

where ω is the angular frequency; L is the aerofoil chord-length. All lengths are non-dimensionalised by the semi-chord in the CAA benchmark problem. In the current computation, the lengths are non-dimensionalised by the chord length L. Hence to maintain the same *gust wavelength to chord ratio*,

the wavenumbers or reduced frequencies used in the current study are twice as large as those in the original benchmark problem, i.e. $k = 0.2,\ and\ 2.0$. Also, there is a factor of a half in equations (21) in the CAA benchmark problem. This factor is not required in the current computation as L is used to non-dimensionalise u_∞. The results to be compared are: the root mean square perturbed pressure P_{RMS} on the aerofoil surface; and the mean square perturbed pressure P_{MS} calculated at a certain radial distance from the centre of the aerofoil, denoted by R. P_{RMS} and P_{MS} are defined as

$$P_{RMS} = \sqrt{\left[\sum_{n=1}^{N} (p'^2) dt_n\right] / t_{sample}}; \tag{23}$$

$$P_{MS} = (P_{RMS})^2,$$

where p' is the pressure fluctuation about the mean value; dt_n is the time step size at the n^{th} time step; t_{sample} is the duration of time of the sample, taken as one time period. For the benchmark problem, the time period of the 2D periodic vortical gust is simply $2\pi/(ku_\infty)$. For all the subsequent calculations in this thesis, the P_{MS} results are presented as directivity patterns which are plots that show the angular variation of P_{MS} at $R = 4L$.

4.1.1 The Current Solution Method

The current code is written in *Fortran 90* and parallelised by using the MPI library. High-order spatial and temporal discretisation schemes described before in Chapters 3.1 and 3.2 are used to solve the governing 2D/3D compressible Euler equations. The CFL number used is 0.95. The three filter parameters, whose values are based on the studies by Kim [38] and Kim and Sandberg [37], are

$$\kappa_C = 0.87\pi;$$
$$\kappa_C^* = 0.80\pi;$$
$$\epsilon = 0.085.$$

The sponge zone thickness L_S, the maximum damping coefficient σ_0 and the velocity forcing length ratio parameter ϕ described in Chapter 3.3 need to be determined by parametric studies. Similar parametric studies can be found in two previous publications [33, 96]. The parametric studies for the 3D code are presented here. The CAA benchmark problem category 3 problem 1 case 2 with $k = 2.0$ is solved in these parametric studies. The grid used is a natural extension of the basic 2D grid in the spanwise or z-direction. The current multi-block structured grid has an H-topology around the 3D aerofoil. The computational domain spans from $-9L$ to $9L$ in the x- and y-directions, and $-0.5L$ to $0.5L$ in the z-direction. There are 65 grid points on each of the aerofoil surfaces; 71 points upstream and downstream of, and 75 points above and below the wing. The total number of grid points on a (x, y) plane is 31,050. Seven grid points are used in the spanwise direction. Hence the total number of grid points used is 217,350. The 3D aerofoil is located at the centre of the domain. $L_S = 3$, $\sigma_0 = 4$ and $\phi = 1.0$ is the basic combination of parameters used in the parametric study. For each of the three tests, only one parameter is changed and the other two are kept constant. Table 1 shows the

range of each of the three parameters tested. The results of the parametric study are presented in the form of sound or P_{MS} directivity patterns at $R = 4L$. The patterns for the L_S, σ_0 and ϕ tests are shown in Figures 9, 10 and 11 respectively.

L_S	σ_0	ϕ
$1L$, $2L$, $3L$, $4L$	1, 2, 3, 4, 5	0.25, 0.50, 0.75, 1.00, 1.25

Table 1: Range of the sponge zone parameters tested

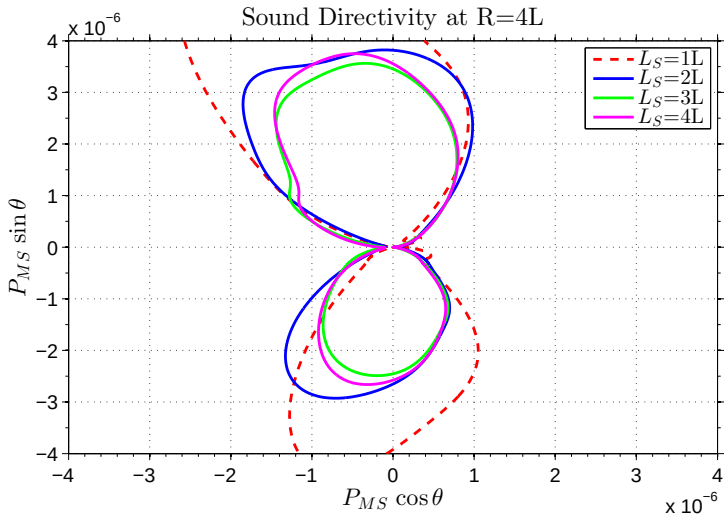

Figure 9: L_S test

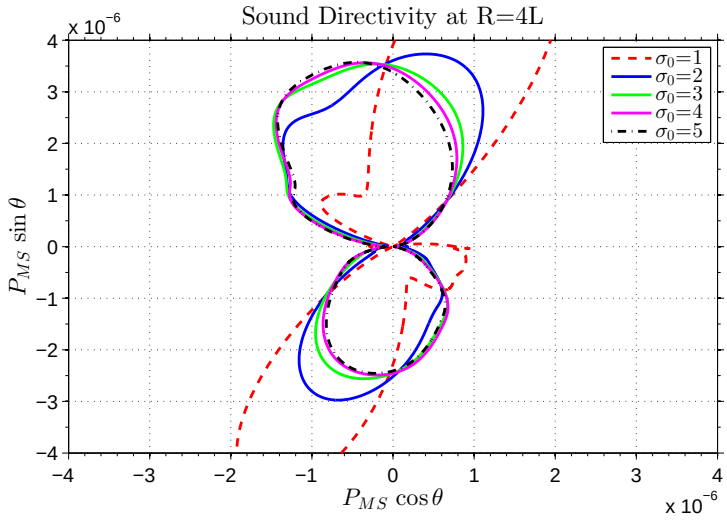

Figure 10: σ_0 test

It can be seen from Figure 9 that the solution converges when $L_S \geqslant 3L$. $L_S = 3L$ is chosen because it is advantageous to have a larger physical domain, which allows the sound at larger radial distance from the centre of the aerofoil to be computed directly. For the σ_0 test, it can be seen from Figure 10 that the solution converges when $\sigma_0 \geqslant 4$. The lower value of $\sigma_0 = 4$ is chosen since excessive damping should be avoided. Finally, Figure 11 shows that for the ϕ test, the solution converges when $\phi \geqslant 0.75$.

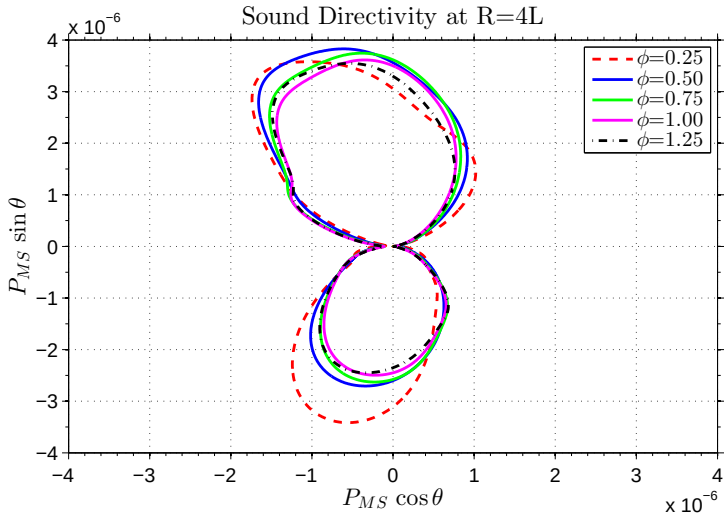

Figure 11: ϕ test

$\phi = 1.0$ is chosen. Therefore, the new sponge BC parameters for the current 3D code are

$$\sigma_0 = 4.0;$$

$$L_S = 3L;$$

$$\phi = 1.0.$$

This combination of sponge zone parameters will be used for all the subsequent calculations in this thesis. The sound directivity patterns computed by the current 2D and 3D codes for case 2 using this combination of sponge zone parameters are plotted in Figure 12. It can be seen from the figure that the current 2D and 3D results are nearly identical. Since this CAA benchmark problem involves 2D aerofoils, the 2D code will be used for this validation study.

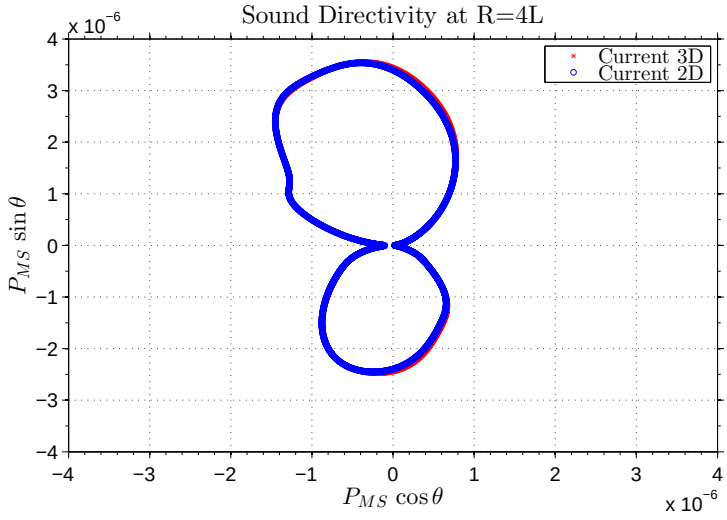

Figure 12: Current solutions computed by 3D and 2D codes

A grid convergence test is performed to check if the current grid point density is enough to achieve a converged solution. Three 2D grids with different grid density are used. The numbers of grid points used for the three grids are shown on Table 2. The resulting sound directivity patterns at $R = 4L$

are plotted in Figure 13. It can be seen from Figure 13 that all three grids produce near-identical results. Hence the current numerical solution has already converged and the current grid point density is sufficient.

Grid	Up-/down-stream	Above/below	Aerofoil upper/lower surface	Total
1	70	70	65	28,700
2	71	75	65	31,050[1]
3	121	121	121	87,846

[1] The same grid density as used in the parametric study

Table 2: The grid convergence test details

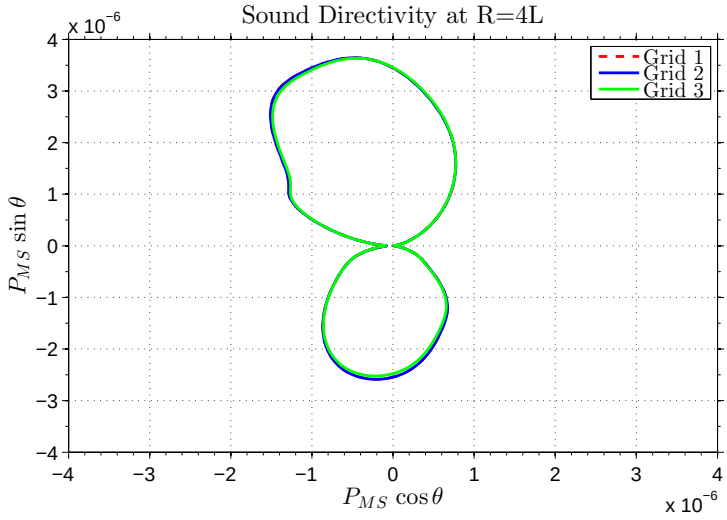

Figure 13: Grid convergence test

4.1.2 The Reference Solution Methods

There are a number of published solutions to this CAA benchmark problem. Some researchers such as Scott [54] obtained the solutions by solving the linearised Euler equations. Others such as Hixon et al. [97] solved the full 2D Euler equations similar to the current study. The two reference solutions used for this validation study were obtained by solving the full Euler equations. The first set of reference solutions is that by Golubev and Mankbadi [56], who utilised the space-time mapping analysis (STMA) method first proposed by Hixon. Their method treated any 2D or 3D unsteady problems as steady-state problems in 3D or 4D. Essentially, the temporal dimension was being treated as an extra spatial dimension. They used the 7-point 4^{th}-order dispersion relation preserving (DRP) scheme by Tam and Webb to solve the STMA equations. Also, 10^{th}-order artificial dissipation was added to ensure numerical stability. Radiation BC and Tam and Webb's BC were used at the inflow and outflow boundaries of each (x, y) plane respectively. They used 605 and 240 grid points in the $x-$ and $y-$directions respectively, i.e. 145,200 points altogether, for the cases with the highest gust frequency (corresponds to $k = 2.0$). The second set of reference solutions is that by Wang et

al. [56], who used the space-time conservation element and solution element (CE/SE) method. Their method was a type of finite volume (FV) method with second-order accuracy in both space and time. Simple non-reflecting BC and an unstructured grid were used. The domain stretched to $23L$ from the aerofoil in all directions, and a much larger number of grid points were used compared to the high-order FD based methods. There were 427,392 *triangles* altogether in the grid used by Wang et al..

4.1.3 Results Comparison

Figures 14 and 15 show the surface mean and RMS pressure distributions comparisons for *case 1* and *case 2* respectively; Figure 16 shows the sound directivity comparisons for *case 1* and *case 2*. Note that no aerofoil surface mean and RMS pressure distributions result was provided by Golubev and Mankbadi for *case 1*.

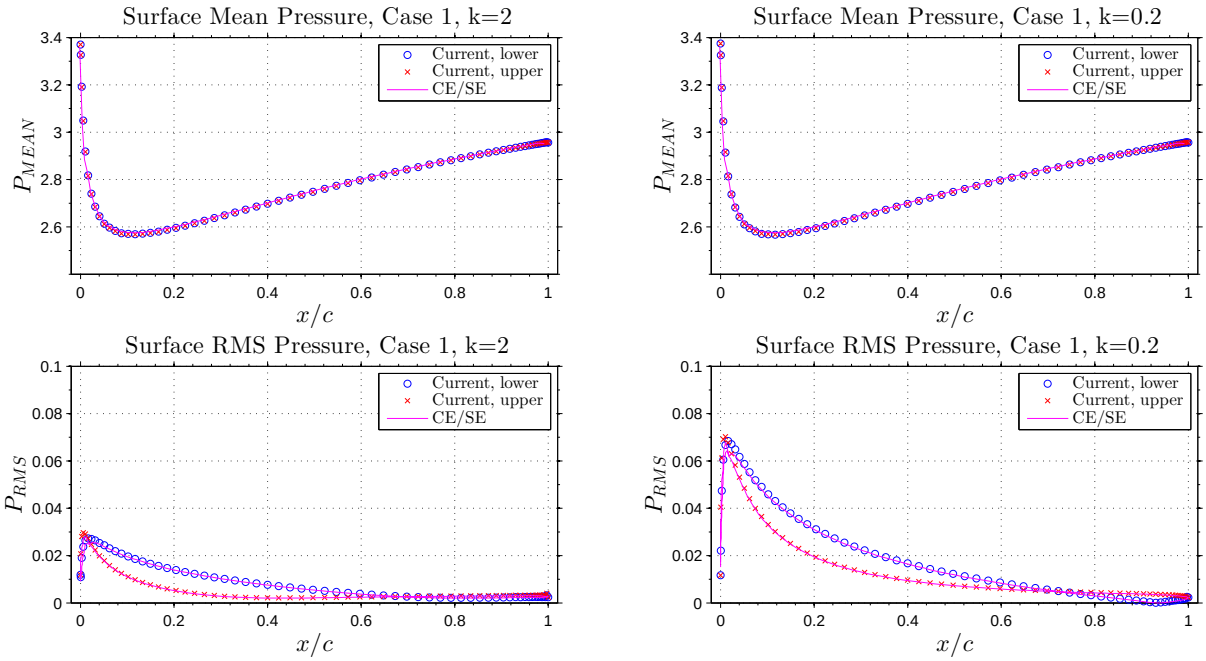

Figure 14: The surface mean and RMS pressure for case 1

It can be seen from the results that the current numerical methodology is capable of producing similar solutions to the published reference solutions. For the aerofoil surface mean and RMS pressure distributions for *case 2*, the results by the STMA method of Golubev and Mankbadi show oscillations near the leading and trailing edges. Such oscillations are not present in the current results. For the sound directivity patterns, the current results are also in good agreement with the reference solutions. The patterns for *case 2* with $k = 2.0$ show bigger variation. The current solution is closer to the solution by the STMA method for that case. It is because similar to the current approach, Golubev and Mankbadi used high-order FD type discretisations. The current methodology, however, is much less computationally expensive than the STMA method. For the cases with $k = 2.0$, the number of grid points required by the current 2D code is only about 20% of that needed by the STMA method on the (x, y) plane. Hence the current numerical methodology is well-suited to be used for more complicated problems such as 3D simulations and simulations with more complex wing section geometries.

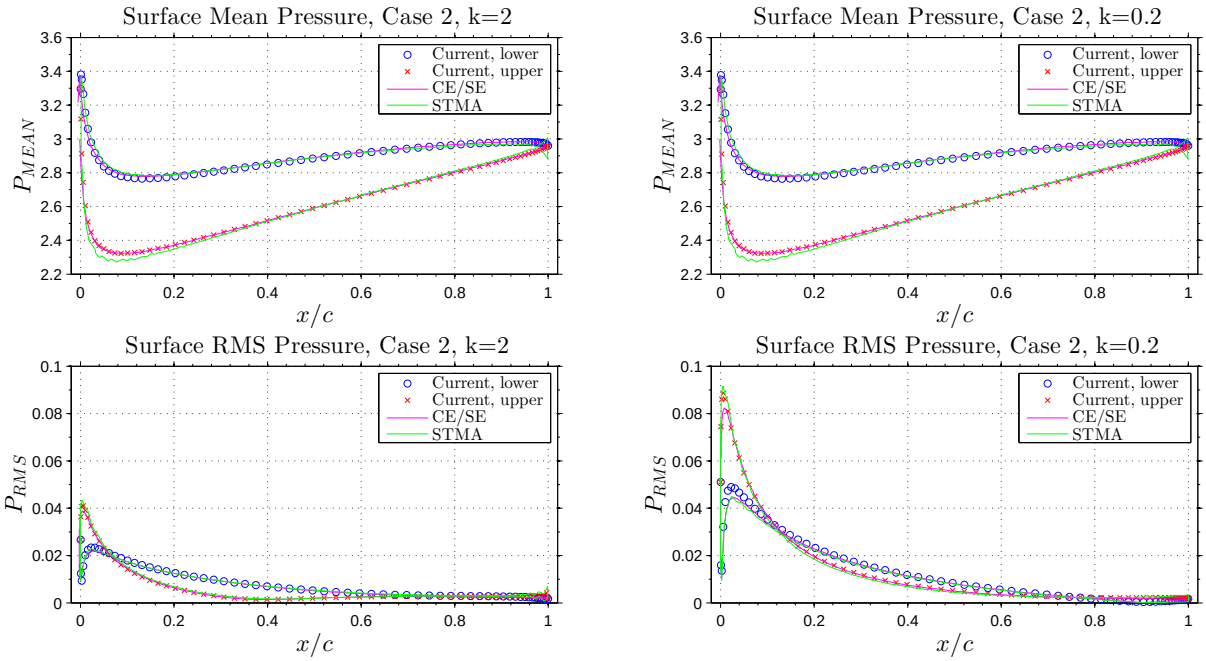

Figure 15: The surface mean and RMS pressure for case 2

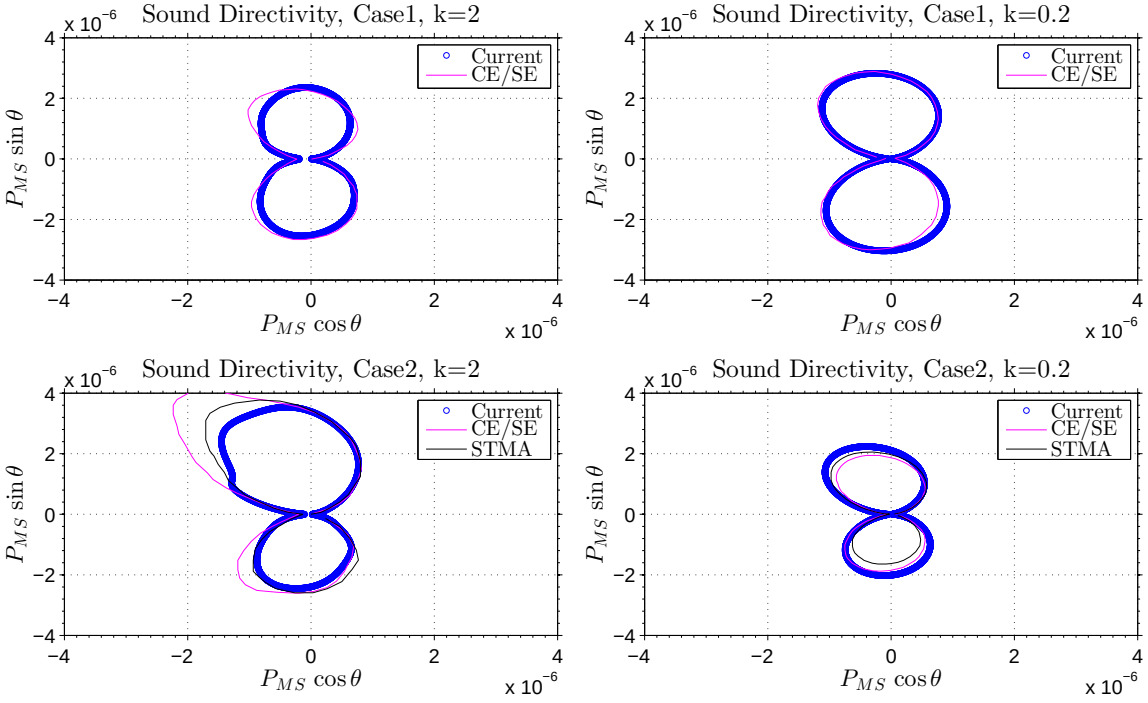

Figure 16: Sound directivity pattern comparisons

4.2 Validations by Theoretical Results

In the second validation study, the theoretical prediction of far-field pressure for a 2D flat plate aerofoil at zero α proposed by Myers and Kerschen [24] mentioned in Chapters 1 and 2.2 is used for comparison. Their theoretical far-field pressure is denoted by P_{MK}, and is plotted as $|P_{MK}|\sqrt{r_{ph}}$, where r_{ph} is the physical radial distance from the leading edge. To compare with the theoretical results, the current numerical results to be plotted is $P_{RMS}\sqrt{r_{ph}}/\zeta$, where P_{RMS} is the root mean square pressure perturbation and ζ is the perturbed velocity magnitude and is a small dimensionless number - $\zeta = 0.01$ is used in this paper. The current values of P_{RMS} are calculated at $r_{ph} = 4L$. The computed $P_{RMS}\sqrt{r_{ph}}$ directivity patterns need to be divided by ζ since P_{MK} is independent on ζ.

For the theoretical model of Myers and Kerschen, the incident gust is 2D and purely vortical, i.e.

$$\begin{pmatrix} u' \\ v' \end{pmatrix} = \zeta U_\infty \begin{pmatrix} A_t \\ A_n \end{pmatrix} e^{ik(\phi + k_n \psi - t)}, \tag{24}$$

where u' and v' are the x- and y-components of the perturbed velocity; ζ is a dimensionless parameter and is assumed to be small; U_∞ is the freestream velocity; k is the reduced frequency defined by equation (22); ϕ and ψ are the dimensionless velocity potential and stream-function, which form the orthogonal curvilinear coordinates system; $\sqrt{{A_t}^2 + {A_n}^2} = 1$ for the vortical velocity to be divergence-free, in here, $A_t = A_n = \sqrt{0.5}$; $k_n = 1/\sqrt{1 - {M_\infty}^2}$, which corresponds to a Prandtl-Glauert transformation, is introduced.

Since this validation study is a 2D problem, it is more convenient to use the current 2D code to produce results for comparison. Before comparing with the theoretical solutions of Myers and Kerschen, the results computed by the current 2D and 3D codes are compared. A 2D flat-plate aerofoil at zero α is subjected to a mean flow with freestream Mach number $M_\infty = 0.5$, and a superposed perturbed velocity defined as

$$u'_i = (-1^{(i-1)})\{A_{\rm mp}\cos[k(x + y - M_\infty t)] + A_{\rm mp}\sin[k(x + y - M_\infty t)]\},$$

where $i = 1$ and 2 for the x and y perturbed velocity components respectively, M_∞ is the freestream Mach number and $A_{\rm mp}$ is the amplitude parameter. Hence, the magnitude of the current u'_i is $\sqrt{2}A_{\rm mp}$. The corresponding magnitude of u'_i employed by Myers and Kerschen was $\sqrt{0.5}\,\zeta U_\infty$, where U_∞ was the freestream velocity. Furthermore, in the current study, the aerofoil full-chord is used to non-dimensionalise lengths. This is different to the study by Myers and Kerschen, who used the semi-chord. Hence in the current computation, a factor of two is added to $A_{\rm mp}$ for fair comparisons. Therefore, $A_{\rm mp} = 2(\sqrt{0.5}\,\zeta M_\infty)/\sqrt{2}$ in the current study. Hence to maintain the same *gust wavelength to chord ratio*, the wavenumbers or reduced frequencies used in the current computations are twice as large as the corresponding values used in the model of Myers and Kerschen. All the values of k referred to in this section from now on are the current values. The pressure directivity patterns with $k = 4$ and $k = 8$, computed by the current 2D and 3D codes are plotted in Figure 17. It can be seen that the current 2D and 3D results are identical.

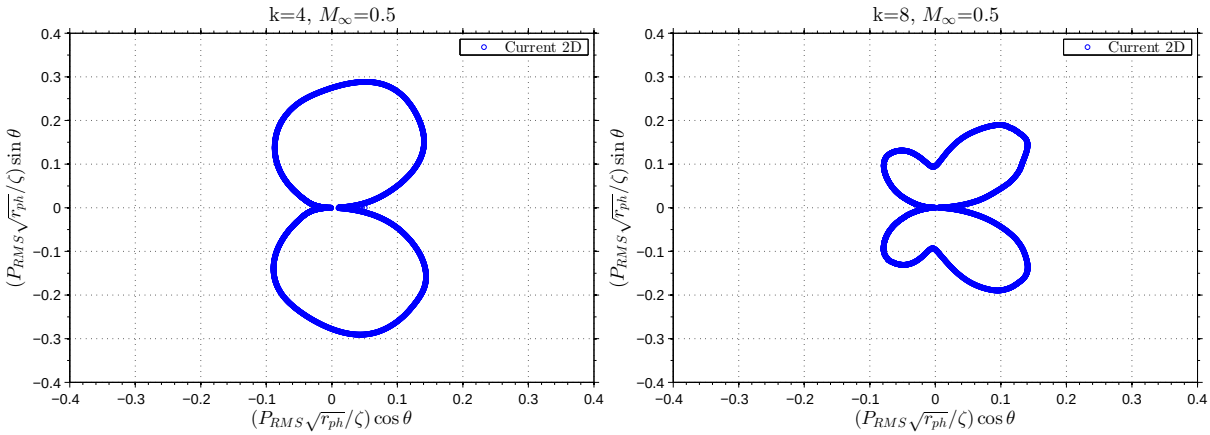

Figure 17: 3D and 2D code results comparison

Now, the results computed by the current 2D code will be used to compared with the theoretical solutions of Myers and Kerschen. Two tests are presented. The first test is about the effect of the reduced frequency k, which varies from three to ten with an increment of one. The freestream Mach number M_∞ remains constant at 0.5 throughout. The resulting directivity patterns for the k tests are shown in Figures 18 and 19. The second test is about the effect of M_∞, which varies from 0.45 to 0.65 with an increment of 0.05. k is kept at 4 for this test. The results for the M_∞ tests are shown in Figures 20 and 21. It can be seen that the computed and theoretical results show very good agreement with each other, particularly for the high-frequency cases since the theory of Myers and Kerschen assumed that the frequency of the convected disturbance was high. This excellent agreement shows that the current methodology is suitable and accurate for the simulations of AGI noise. In the next section, the first of the validation studies which utilises 3D aerofoils will be presented.

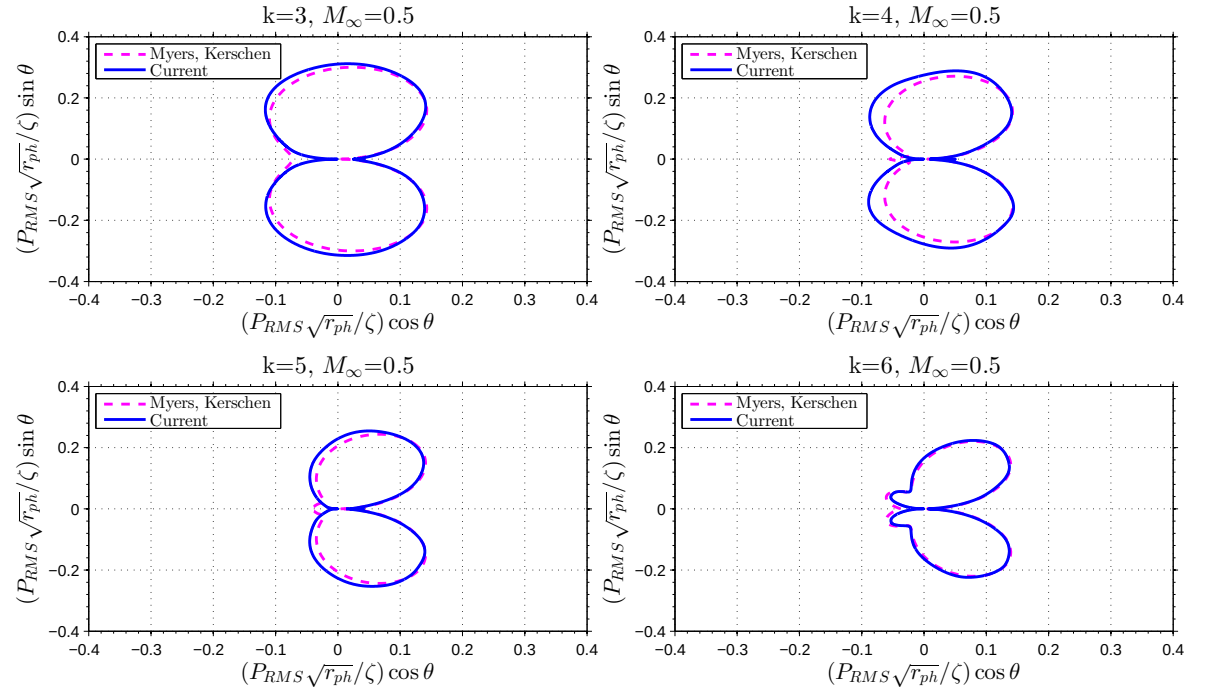

Figure 18: The effect of reduced frequency, k = 3, 4, 5 and 6

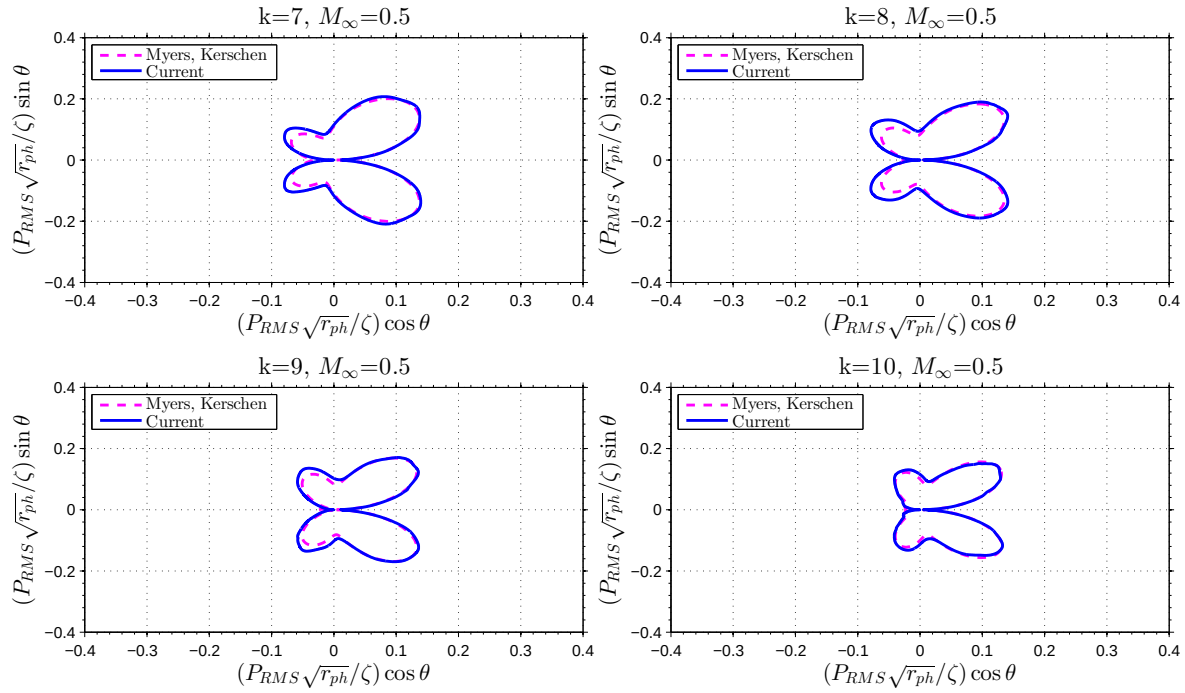

Figure 19: The effect of reduced frequency, $k = 7$, 8, 9 and 10

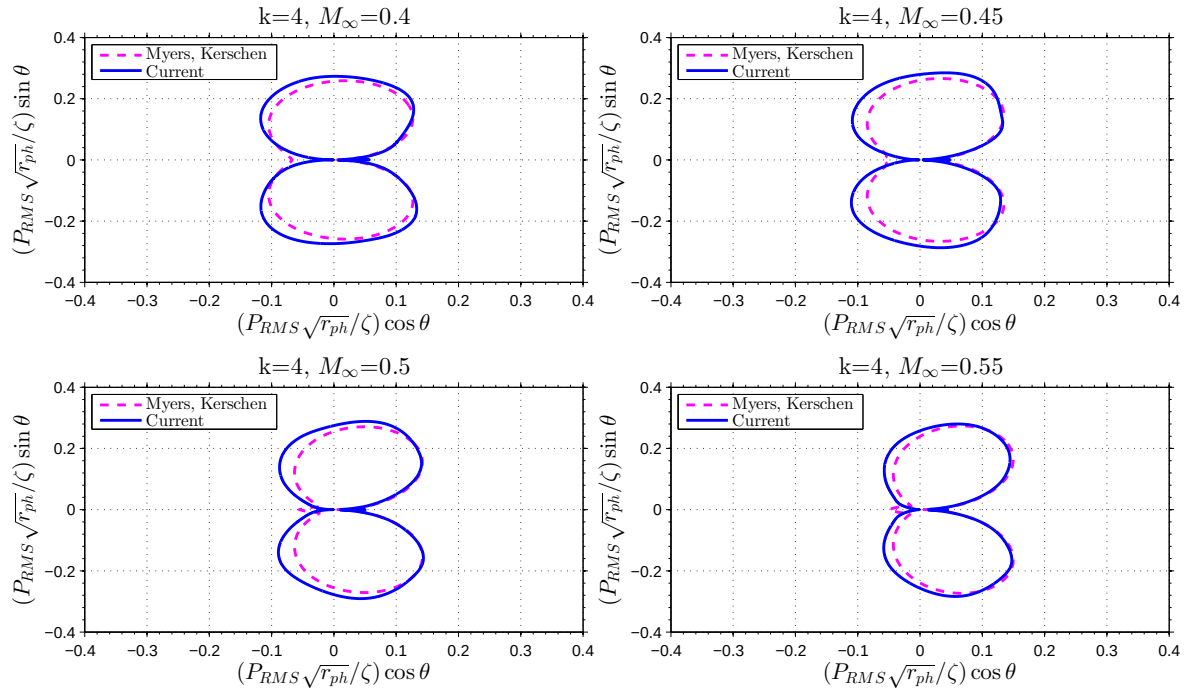

Figure 20: The effect of free-stream Mach number, $M_\infty = 0.4$, 0.45, 0.5 and 0.55

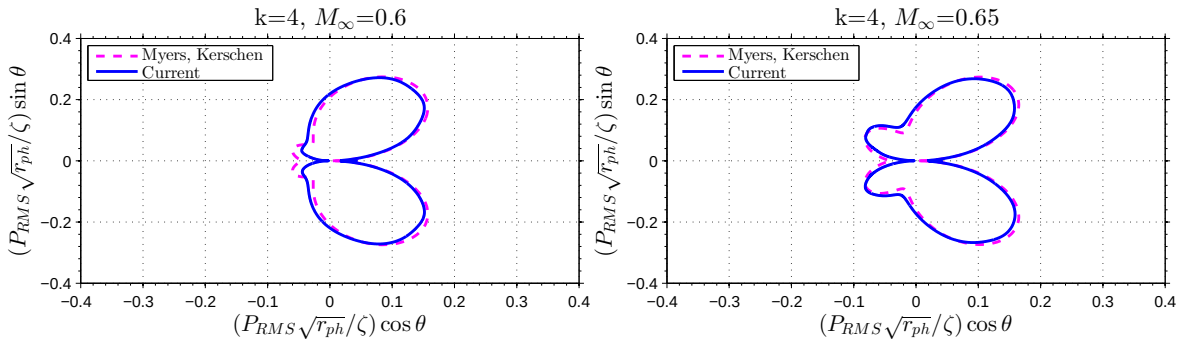

Figure 21: The effect of free-stream Mach number, $M_\infty = 0.6$ and 0.65

4.3 Validations by Lift Coefficients Comparison

The third validation study involves comparison with experimentally measured data for lift coefficients. Figure 22 shows the present 3D aerofoil geometry and the frame of computational domain used, where the definitions of leading-edge amplitude and wavelength, denoted by LEA and LEW respectively, are given. Note that LEA is peak-to-peak based, and the presence of leading-edge waviness does not change the aerofoil shape and the wing planform area.

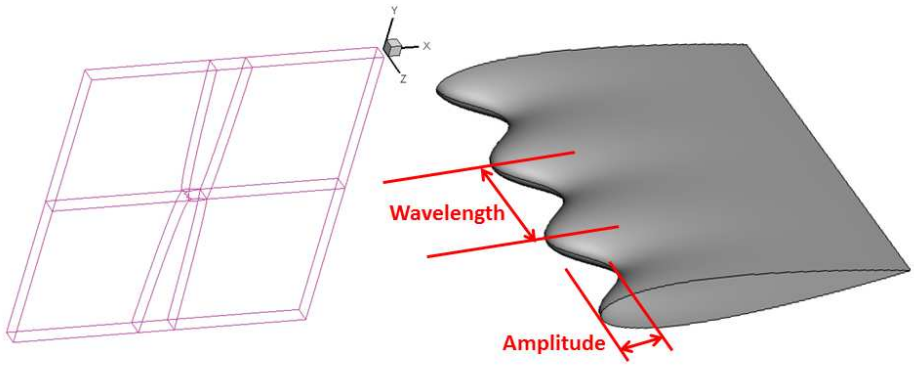

Figure 22: The grid structure and the definitions of leading-edge amplitude and wavelength

The imposed perturbed velocity components are based on the first approach and are given by

$$u_i' = A_i \cos(k_1 x + k_2 y + \omega t) + B_i \sin(k_1 x + k_2 y + \omega t) \text{ for } i = 1, 2, \tag{25}$$

where the amplitude parameters $A_1 = B_1 = 0.005$ and $A_2 = B_2 = -0.004$ are constantly used in the subsequent simulations in this thesis. The prescribed velocity disturbances are mainly in the streamwise ($x-$) and vertical ($y-$) directions, whereas the spanwise component u_3' is used only to satisfy the divergence-free condition avoiding unwanted pressure fluctuations to appear in the freestream. The streamwise and vertical components are the major ones causing pressure fluctuations on the aerofoil surface leading to AGI noise. The freestream Mach number is set to $M_\infty = 0.5$ for the rest of the thesis unless otherwise specified. The indices $i = 1, 2$ denote the Cartesian coordinates; u_i' represents the velocity perturbation along the i^{th} direction; k_1 and k_2 are the non-dimensional

wavenumbers; and $\omega = -k_1 M_\infty$ is the angular frequency for a wave travelling in the positive x-direction (from left to right).

First, a grid convergence test is performed. Two grids, one with double the grid density of the other, are used. Then, two different sizes of the domain in the spanwise direction are tested. Two grids of the same grid density on the $x-y$ plane, one with *two* LEWs in span and the other with only one, are used. For these two tests, $k_1 = k_2 = 2\pi$, $\alpha = 0$ and the NACA 0015 aerofoil are used. Periodic BCs are imposed on the two spanwise $x-y$ end planes. For both tests, $LEA = 0.1L$ and $LEW = 0.5L$. The parameters for the compact filters and the sponge zone, as well as the dimensions of the domain in the $x-y$ plane are the same as in the previous sections. The numerical results presented are directivity patterns of P_{MS} in the $x-y$ plane, which are averaged over the span in z-coordinate and obtained at a radial distance R of $4L$ from the averaged centre of the 3D aerofoil section.

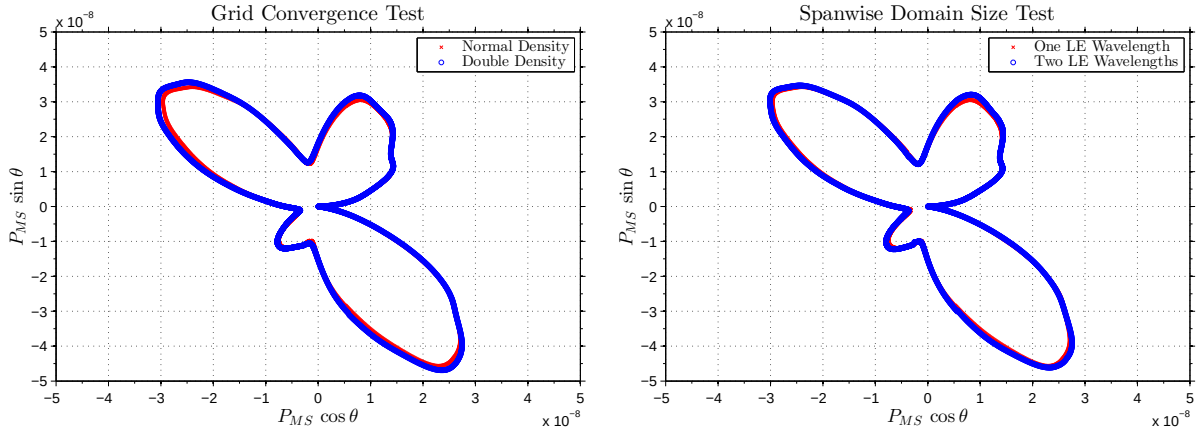

Figure 23: Grid convergence and domain size tests

Figure 23 shows the resulting directivity patterns for the two tests. From the plot on the right of Figure 23, it can be seen that the directivity patterns for the two grids of equal grid density but with different span lengths are identical. This indicates that one leading-edge wavelength in span is sufficient for the subsequent investigation. The plot on the left of Figure 23 shows that the two grids with different grid density yield very little difference in solution. This result provides a baseline grid for simulations in the case of $k_1 = k_2 = 2\pi$ as shown in Table 3.

Up- or down-stream	131
Above or below	131
Upper and lower surface of aerofoil	131
Spanwise	36
Total	3,706,776

Table 3: The number of grid points used in the baseline grid

This baseline grid contains about 11 grid points per gust wavelength near the domain boundaries

where the grid is the coarsest. The same level of grid density per gust wavelength is maintained in this thesis for all the other cases with different gust frequencies. Note that the spanwise number of grid points varies with different values of LEW.

Since the current numerical simulations are inviscid, no meaningful drag results can be drawn. However, the lift at low α is computed and compared with some measured data for validation purpose. In this third validation study, the lift is calculated by integrating all the elemental surface pressure force components around the 3D aerofoil in the vertical direction. The aerofoil used for this validation study is also NACA 0015. For the first test, a straight leading edge is used and *no* incident gust is imposed. Three freestream Mach numbers are tested: 0.1, 0.3 and 0.5. The values of lift coefficient (C_L) are calculated for $\alpha = -1°$, $0°$, $1°$, $2°$, $3°$. The computed lift coefficients are compared with the experimental data at $Re = 3.6 \times 10^5$ provided by Sheldahl and Klimas [95] for the same aerofoil (NACA 0015).

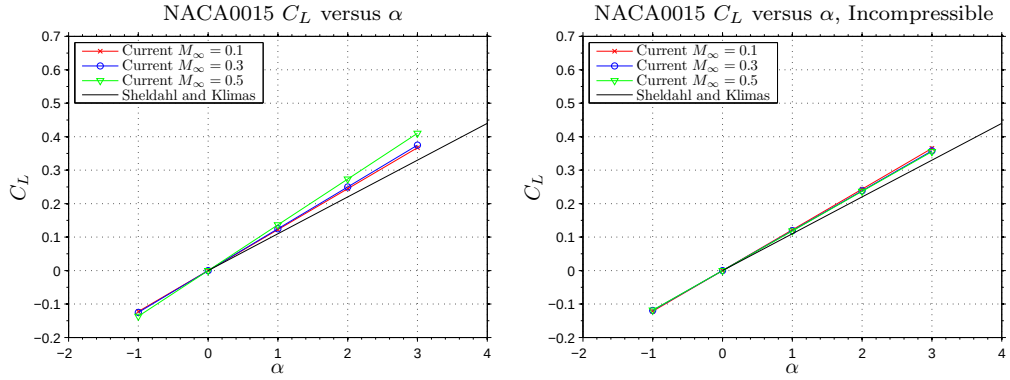

Figure 24: Calculated lift coefficients (for a straight leading edge) compared with experimental data

The computed lift coefficients are presented in Figure 24, where the left figure is straight from the current calculation and the right one shows the current data multiplied by the Prandtl-Glauert factor $\sqrt{1 - {M_\infty}^2}$ that converts the current compressible C_L to its corresponding incompressible value. It can be seen from the plot on the left that as Mach number increases, the slope of the current C_L-to-α lines also increases. This increase in slope is due to the compressibility effect as suggested by the plot on the right, which shows that the current C_L-to-α lines at different Mach numbers collapse onto a single line after applying the Prandtl-Glauert factor. The discrepancy between the current and the experimental data is conjectured to result from the omission of viscosity in the current simulation.

The second test employs wavy leading edges and an incident vortical gust given by Eq. (25) with the same Mach number ($M_\infty = 0.5$) and wavelength ($k_1 = k_2 = 2\pi$) used in the earlier grid-convergence test. The spanwise size of the domain is set to one LEW as mentioned earlier. The test cases are listed in Table 4. The resulting C_L data are plotted in Figure 25 compared with the data from a straight leading edge without the incident gust. It can be seen that all the calculated data agree with each other very well, which indicates that the averaged aerodynamic performance of the present 3D aerofoils with wavy leading edges is identical to that of the original 2D aerofoil.

	LEA	LEW	α tested
Case 1	$0.1L$	$0.5L$	0°, 1°, 2°, 3°
Case 2	$0.2L$	$1.0L$	0°, 2°, 4°
Case 3	$0.3L$	$1.0L$	0°, 2°, 4°
Case 4	$0.4L$	$1.0L$	0°, 2°

Table 4: Test cases for C_L validation of the 3D aerofoil with wavy leading edges

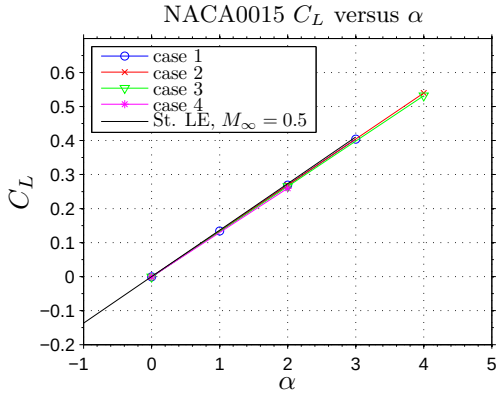

Figure 25: Aerodynamic validation of the present 3D aerofoils with wavy leading edges

Since no viscosity is included in the current study, the current simulation is meaningful only in a low range of α. Given the limitation, the validation studies show that the current numerical methodology provides an accurate, reliable and efficient ground for the investigation of AGI noise associated with wavy leading edges.

4.4 Validations by the Mean Aerodynamics of Wavy Leading Edges

The last validation study involves comparing qualitatively the mean aerodynamic features of wavy leading edges observed in the current simulation and reported in the literature. It has been reported in the literature that for leading-edge tubercles and wavy leading edges, the mean pressure is lower and the mean velocity is higher in the troughs [13, 14, 18–20, 72, 79]. The numerical surface mean pressure and mean velocity contours from a current simulation (with $LEA = 0.3L$ and $M_\infty = 0.5$) are plotted in Figures 26 and 27 respectively. It is obvious that for the 3D aerofoil with a wavy leading edge, the surface mean pressure is lower and the surface mean velocity is higher in the troughs. This indicates that the current numerical methodology is able to simulate the near-surface mean pressure and mean velocity properly.

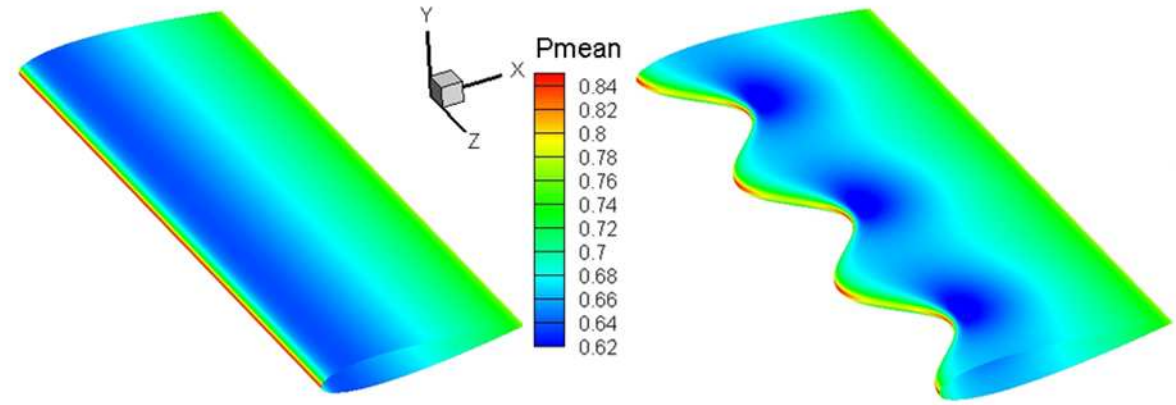

Figure 26: Numerical surface mean pressure contour

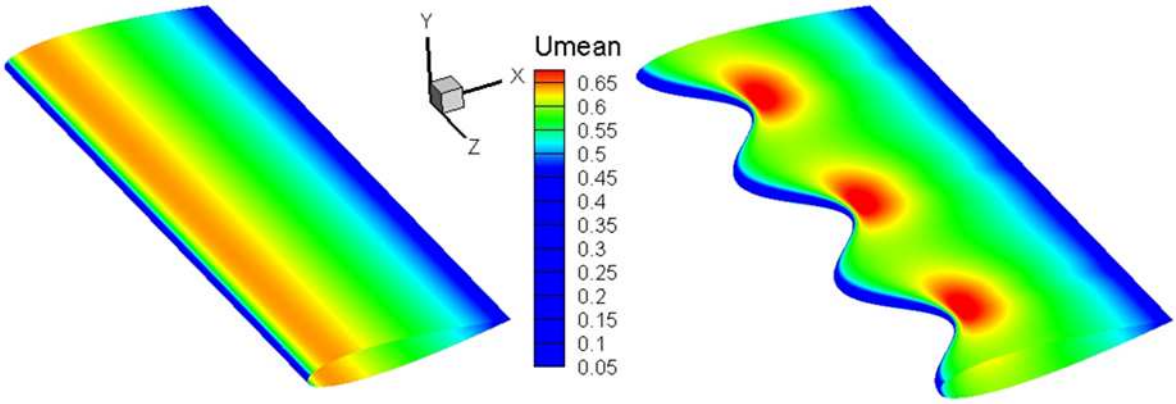

Figure 27: Numerical surface mean velocity magnitude contour

5 The Effects of Wavy Leading Edges on AGI Noise

The high accuracy and the high efficiency of the current numerical methodology have been demonstrated by the validation studies. Now the current code can be used, with confidence, for the investigation of the effects of wavy leading edges on AGI noise. For all the subsequent tests shown in this thesis, unless stated otherwise, the first approach (Eq. (25)) to prescribe the incident gust, the amplitude parameters $A_1 = B_1 = 0.005$ and $A_2 = B_2 = -0.004$, the freestream Mach number $M_\infty = 0.5$ and the NACA 0015 aerofoil are always used.

5.1 The Effects of Wavy Leading-Edge Amplitude and Wavelength

In this section, the effects of wavy leading-edge peak-to-peak amplitude (LEA) and wavelength (LEW) with respect to the longitudinal (streamwise) wavelength of the incident gust (λ_g) on AGI noise are investigated. Four different gusts with $\lambda_g/L = 2.0$, 1.0, 0.5 and 1/3, which are referred to as the *very-low-*, the *low-*, the *medium-* and the *high-frequency* gusts respectively, are used. The numerical results are presented in the form of spanwise-averaged $x-y$ plane P_{MS} directivity patterns plotted at $R = 4L$ from the averaged centre of the 3D aerofoil section. Also, the percentage differences relative to the straight leading-edge case are plotted against the sound propagation angle θ, whose definition is shown in Figure 28. The test cases in this section are listed in Table 5.

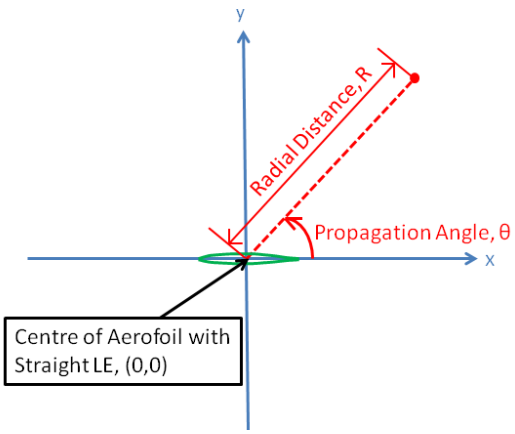

Figure 28: Definition of sound propagation angle θ

The low-frequency gust is used for Tests 1.0 and 2.0 to 2.3, and the high- and medium-frequency gusts are used for Tests 1.1 and 3 respectively. Zero α is applied in this section. Tests 1.0 and 1.1 investigate the effects of LEA, and Tests 2.0 to 2.3 and 3 are for the effect of LEW, where the geometric parameters are related with the gust wavelength (λ_g). Collectively, these parametric tests should show a glimpse of when the reduction in AGI noise becomes significant.

	LEA	LEW	λ_g
Test 1.0	$0.1L$ to $0.5L$[a]	$1.0L$	1.0L
Test 1.1	$0.1L, 0.3L, 0.5L$	$0.3L$	(1/3)L
Test 2.0	$0.3L$	$0.5L$ to $2.0L$[b]	1.0L
Test 2.1	$0.1L$	$0.5L, 1.0L, 1.5L, 1.75L$	1.0L
Test 2.2	$0.2L$	$0.5L, 1.0L$	1.0L
Test 2.3	$0.5L$	$0.5L, 0.75L, 1.0L$	1.0L
Test 3	$0.15L$	$0.0L, 0.5L, 0.75L, 1.0L$	0.5L

[a] Increments of 0.1L

[b] Increments of 0.25L

Table 5: The list of leading-edge and gust parameters tested in this section

5.1.1 The Effects of LEA

The resulting directivity patterns of P_{MS} from Test 1.0 for the low-frequency gust and the percentage differences relative to the straight leading-edge case are plotted in Figure 29. It can be seen that the AGI noise level reduces as the peak-to-peak LEA increases and the amount of reduction is particularly significant at the major angles of propagation. It is shown that 80% or higher percentage reduction in a wide range of angles can be achieved with $LEA = 0.5L$. However, there should be a certain limitation to the peak-to-peak LEA value in practical wind-turbine applications due to structural concerns.

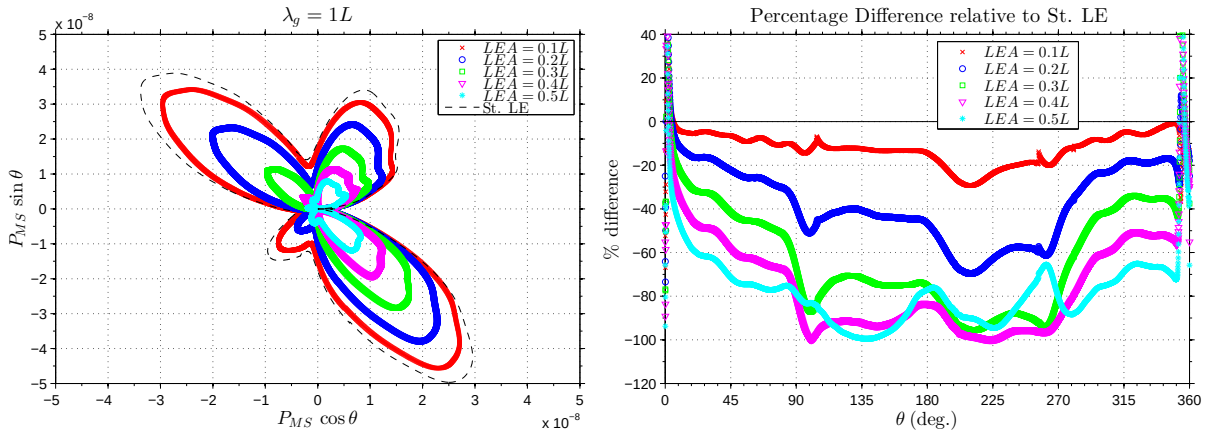

Figure 29: Results of Test 1.0 for the effect of LEA based on a low-frequency gust

Figure 30 shows the result of an additional test with $LEA = 0.15L$ and $LEW = 0.5L$ against the medium-frequency gust. The result of Test 1.0 with $LEA = 0.3L$ is also shown together. For both tests, the ratio of wavy leading-edge amplitude to the longitudinal (streamwise) wavelength of the gust, denoted by LEA/λ_g, is fixed at 0.3. From Figure 30, it can be seen that, although the incident gusts and the leading-edge geometries of the two tests are significantly different, the profiles of the relative (normalised) reduction of AGI noise look remarkably similar. This suggests that LEA/λ_g is the key factor that characterises the performance of wavy leading edges.

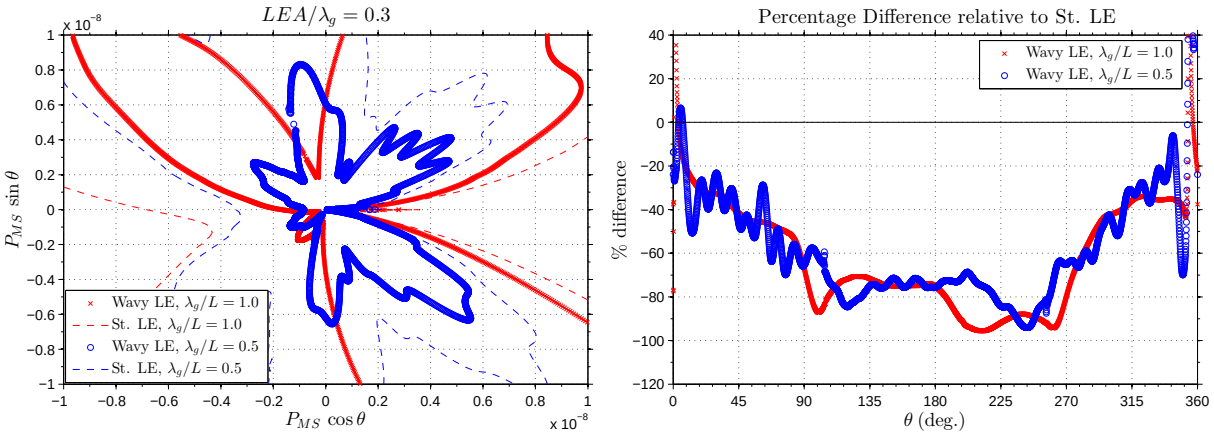

Figure 30: The effect of LEA/λ_g: comparison of low- and medium-frequency gust cases

Figure 30 also shows that the medium-frequency gust generates a smaller level of AGI noise and more complex directivity patterns with distinct lobes, compared to the low-frequency gust. Note that the amplitude parameters of the low- and the medium-frequency gusts are identical. Myers and Kerschen [6] analytically predicted for a 2D flat plate that the acoustic power of AGI noise would be inversely proportional to the reduced frequency of the gust.

Figure 31 shows the results of Test 1.1 based on the high-frequency gust, which showcases that a high percentage reduction of AGI noise (80% or more) uniformly in all directions may be achieved when LEA/λ_g is sufficiently larger than 0.3 at the given LEW. This test also suggests that the amount of noise reduction may become saturated when LEA/λ_g is around 0.9. Note that the local data in the trailing-edge direction ($\theta = 0°$ and $360°$) may not be sufficiently meaningful since the original values of P_{MS} in that region are extremely small and numerical errors associated with the geometric singularity of the trailing-edge may have prevailed.

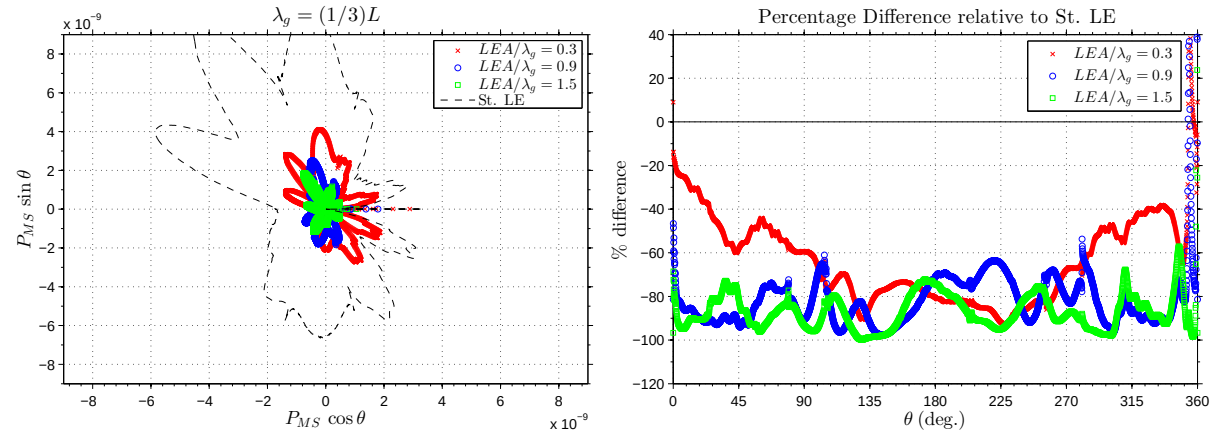

Figure 31: Results of Test 1.1 for the effect of LEA/λ_g based on a high-frequency gust

Figure 32 compares the three different cases from the low-, medium- and high-frequency gusts with the same value of $LEA/\lambda_g = 0.3$. Two additional tests, one with $LEA = 0.4L$ and $LEW = 1.0L$ against the very-low-frequency gust, and the other with $LEA = 0.1L$ and $LEW = 1.0L$ against the medium-frequency gust, have been performed. Both these two additional tests have $LEA/\lambda_g = 0.2$.

Figure 33 compares the three different cases from the very-low-, low- and medium-frequency gusts with the same value of $LEA/\lambda_g = 0.2$. The similarity in the profiles of relative (normalised) noise reduction at the same value of LEA/λ_g, which was conjectured earlier from Figure 30, now looks more convincing. This confirms that LEA/λ_g is the key factor to predict and characterise the aeroacoustic performance of wavy leading edges for the reduction of AGI noise.

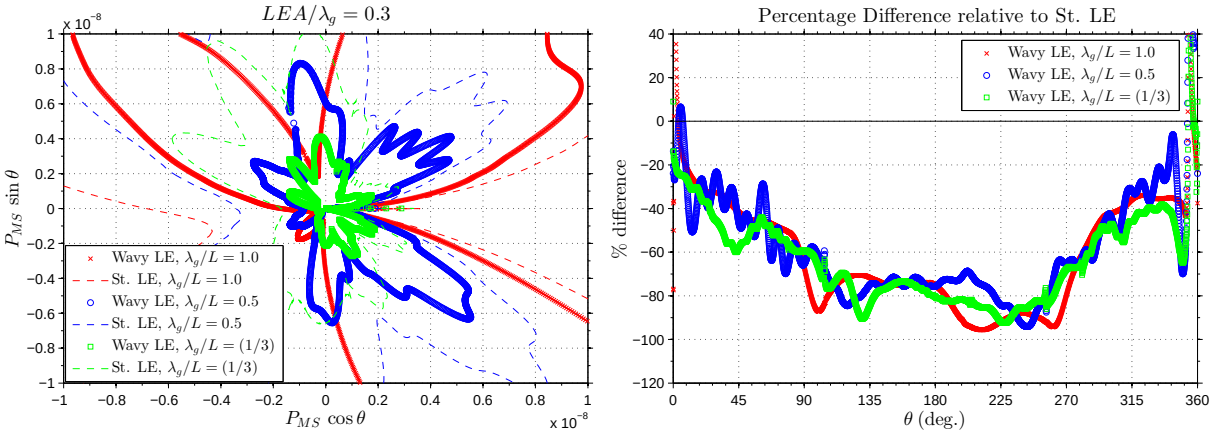

Figure 32: The effect of LEA/λ_g: comparison of low-, medium- and high-frequency gust cases

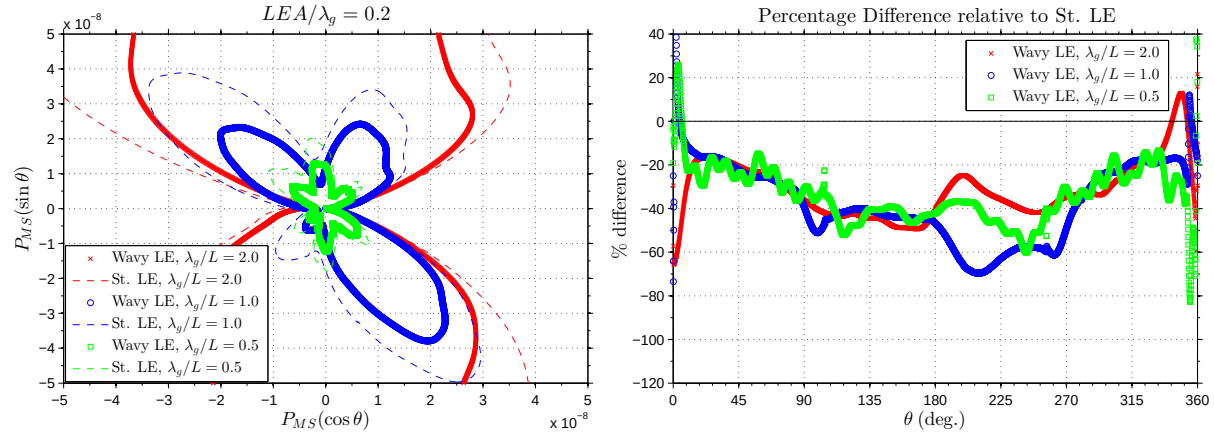

Figure 33: The effect of LEA/λ_g: comparison of very-low-, low- and medium-frequency gust cases

5.1.2 The Effect of LEW

Figure 34 shows the directivity patterns of noise propagation and the profiles of relative noise reduction for Test 2.0 where various wavelengths of the wavy leading edge are investigated. In this test, LEA/λ_g is kept at 0.3 and, again, the similarity in the profiles of relative noise reduction takes place irrespective of various LEWs. Although the profiles show insignificant differences against each other due to the similarity prevailing, the results suggest that some improvement in noise reduction may be achieved by adjusting LEW.

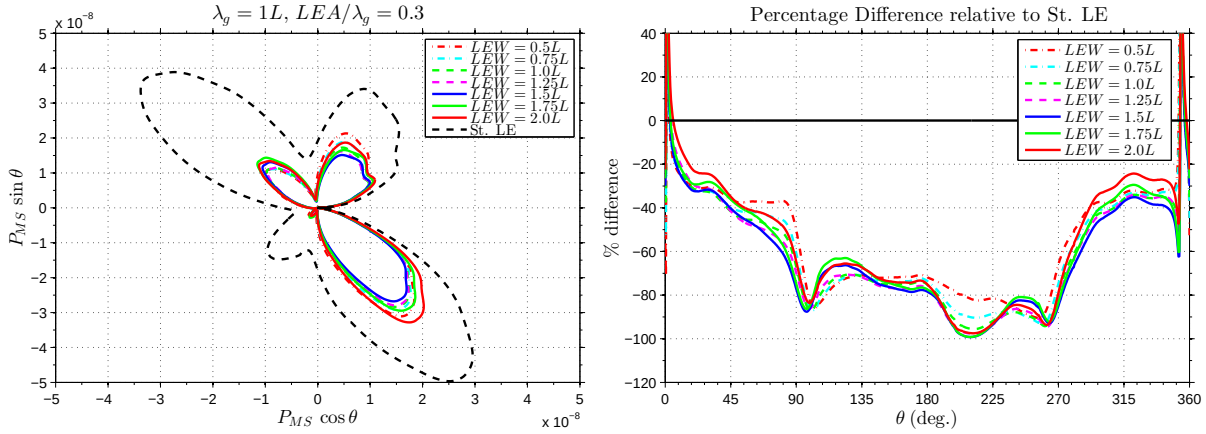

Figure 34: Results of Test 2.0 for the effect of LEW

To further investigate the effect of LEW, Tests 2.1, 2.2 and 2.3 are conducted for three different values of LEA/λ_g and the results are plotted on Figures 35, 36 and 37 respectively. Overall, the results show the major dependency of LEA/λ_g with minor variations against LEW. It is conjectured that the minor effect of LEW might be attributed to the present gust model with perturbed velocity components that do not vary in the spanwise (z-) direction, which results in weak interactions with the spanwise-varying aspect of the wavy leading edges.

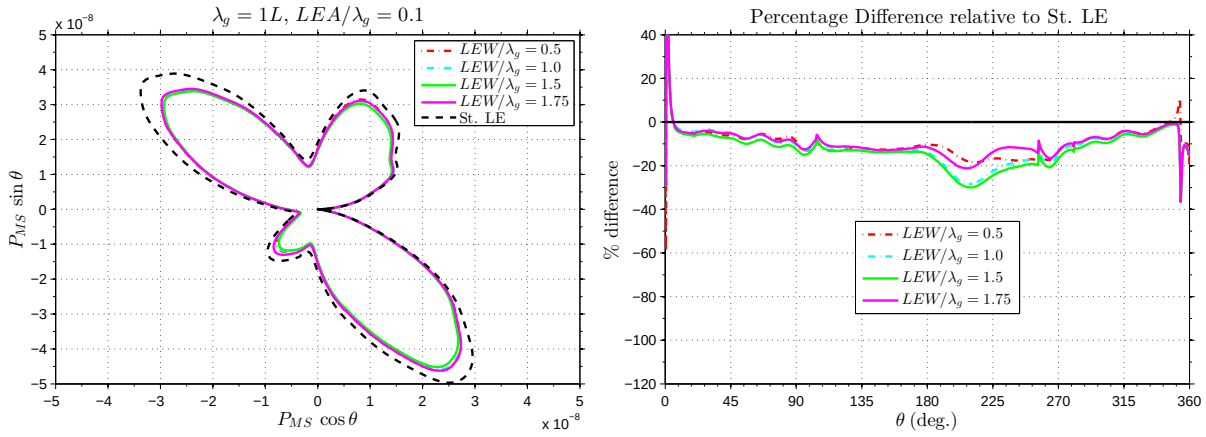

Figure 35: Results of Test 2.1 for the effect of LEW

In Figure 35 for $LEA/\lambda_g = 0.1$, it can be seen that there is an additional reduction in noise between $LEW/\lambda_g = 0.5$ and 1.0. The noise reduction seems to reach the maximum at $LEW/\lambda_g = 1.5$ (as hinted in Test 2.0) but returns to the initial level at $LEW/\lambda_g = 1.75$. The meaningful improvement of noise reduction taking place between $LEW/\lambda_g = 0.5$ and 1.0 is also exhibited in the following Figures 36 and 37 for different values of LEA/λ_g (0.2 and 0.5 respectively). While these results are based on the low-frequency gust, Test 3 is carried out for the medium-frequency gust. Figure 38 shows the results of Test 3 where LEA/λ_g is set to 0.3 and three different cases of $LEW/\lambda_g = 1.0$, 1.5 and 2.0 are compared. It can be seen that the same trends found in the low-frequency gust case still apply in the higher-frequency case. It is worth noting again that the effect of leading-edge wavelength (albeit less significant than LEA) becomes meaningful when $1.0 \leqslant LEW/\lambda_g \leqslant 1.5$ whereas the effect diminishes outside the range.

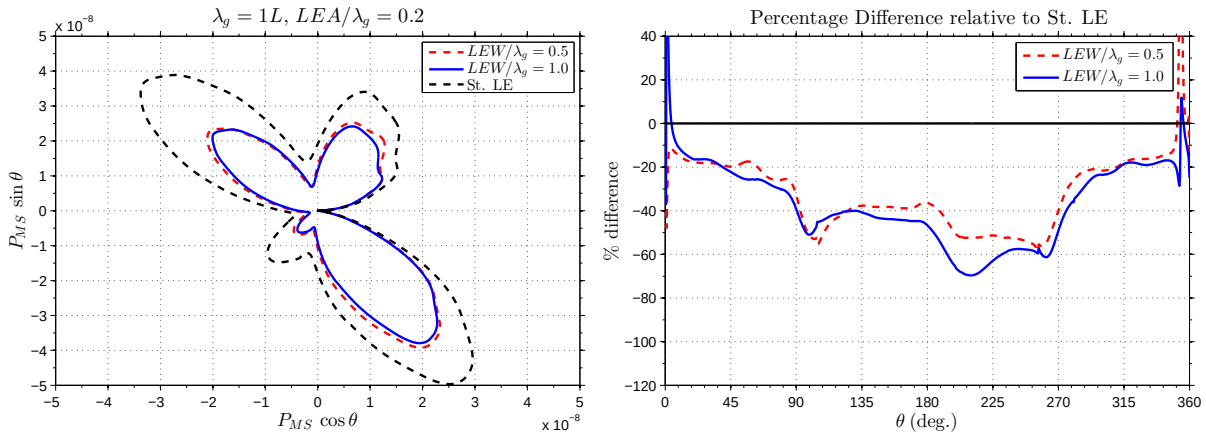

Figure 36: Results of Test 2.2 for the effect of LEW

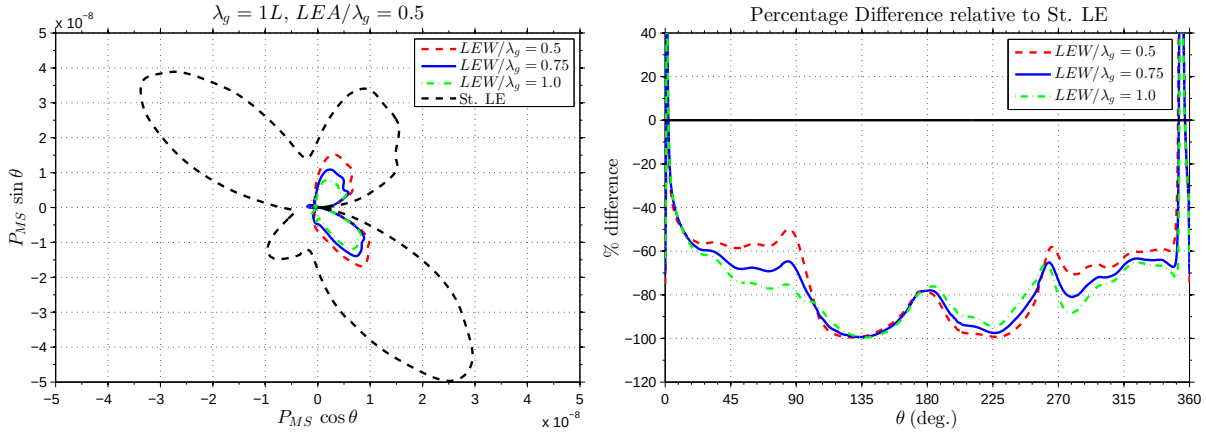

Figure 37: Results of Test 2.3 for the effect of LEW

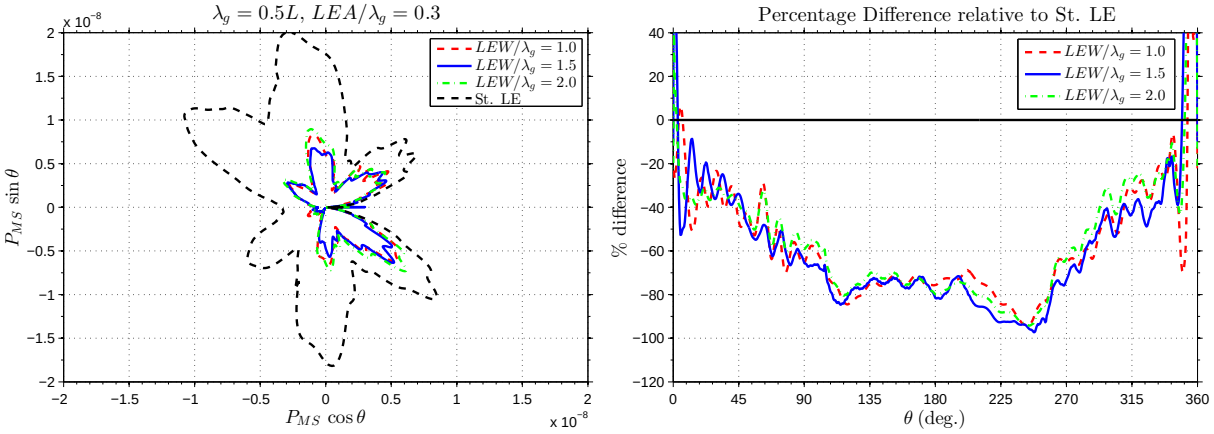

Figure 38: Results of Test 3 for the effect of LEW/λ_g

5.2 The Noise Reduction Mechanism of Wavy Leading Edges

In this section, the AGI-noise-reduction mechanism of wavy leading edges is investigated. Two different wavy leading edge geometries ($LEA = 0.3L$ and $0.4L$ with both $LEW = 1.0L$) are employed and the results are compared against the straight leading-edge case. The incident gust is also imposed by using the first approach (Eq. (25)) with $k_1 = k_2 = 2\pi$ which sets the longitudinal wavelength of the gust to $\lambda_g = 1.0L$. The time signals of pressure fluctuation and its rate of change are recorded at six 'transducer' points located around a leading edge. The transducer locations are depicted in Figure 39 and they are namely, *Peak 1* and *2*; *Middle 1* and *2*; and, *Trough 1* and *2*. Hence there are three pairs of transducers for each geometry. Although the straight leading edge has no peak or trough, the same names of transducers are used to indicate the corresponding locations.

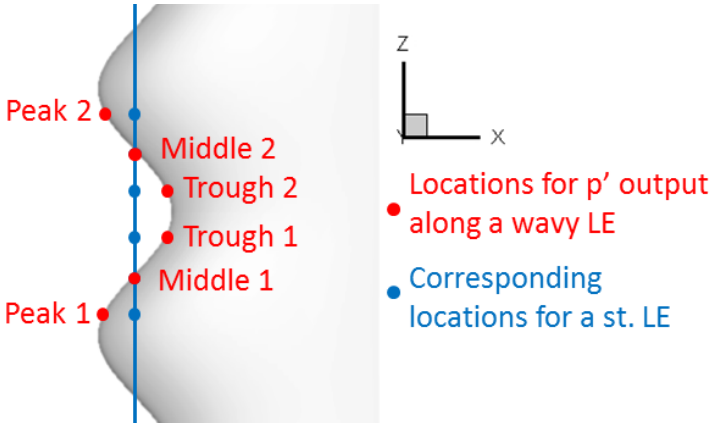

Figure 39: Six 'transducer' locations for the measurement of pressure fluctuations

The time signals of pressure fluctuation and its rate of change calculated and collected at the six transducer locations for the three leading-edge geometries are plotted in Figures 40 and 41 respectively. The results show that, for the straight leading edge, the signals are completely in-phase and are almost identical as anticipated. In contrast, wavy leading edges produce significant phase shifts between signals from different pairs of transducers (although no difference is observed among each pair of transducers 1 and 2). It seems apparent that the case of $LEA/\lambda_g = 0.4$ yields larger phase shifts and lower levels of fluctuations than the case of $LEA/\lambda_g = 0.3$. Both wavy leading edges show noticeably decreased fluctuations compared to the straight leading edge.

In order to check the global effect of the wavy leading edges, the pressure fluctuation data are integrated over the aerofoil surface and the perturbed lift coefficient (C_L') is calculated. The time signals of C_L' and dC_L'/dt for the three different leading edges are plotted in Figure 42. It is confirmed that the wavy leading edges reduce the amplitude of fluctuations compared to the straight leading-edge case and the reduction becomes more pronounced as LEA/λ_g increases.

The results indicate that the wavy leading edges yield a de-synchronised gust response (phase shift) in span along the frontline of the aerofoil, which makes the local pressure fluctuations around

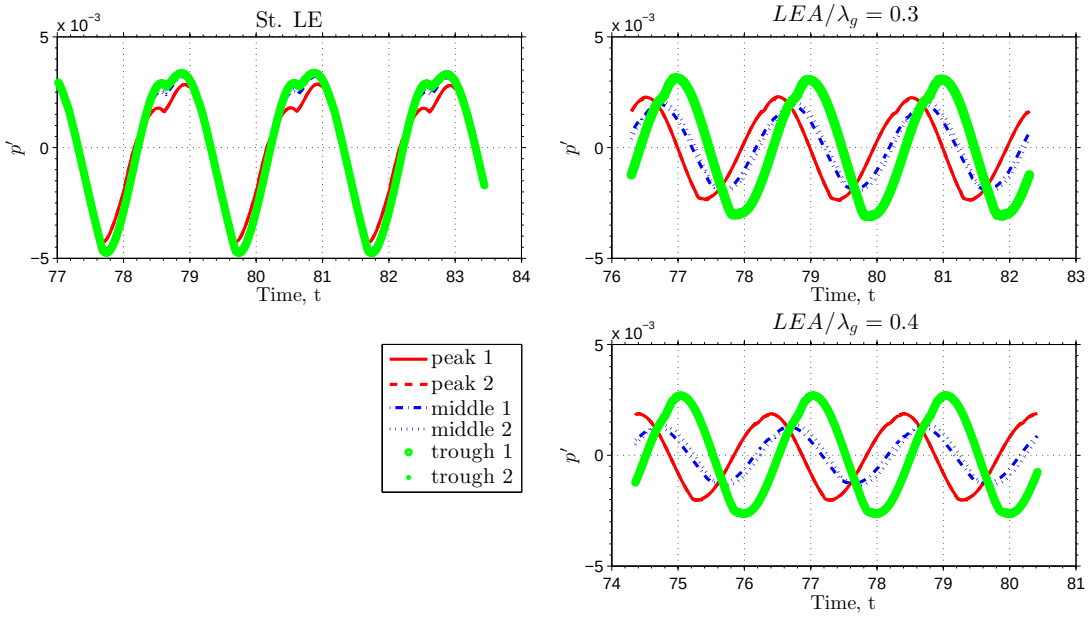

Figure 40: Time signals of pressure fluctuation (p') measured at the six transducer locations for three different leading-edge geometries

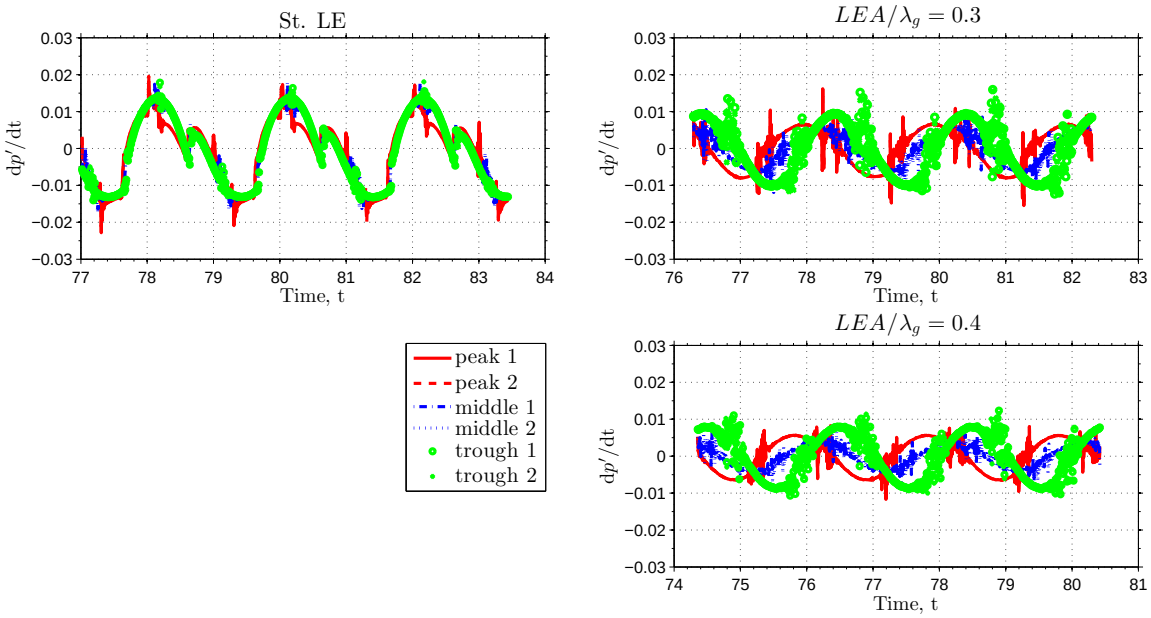

Figure 41: Time signals of dp'/dt measured at the six transducer locations for three different leading-edge geometries

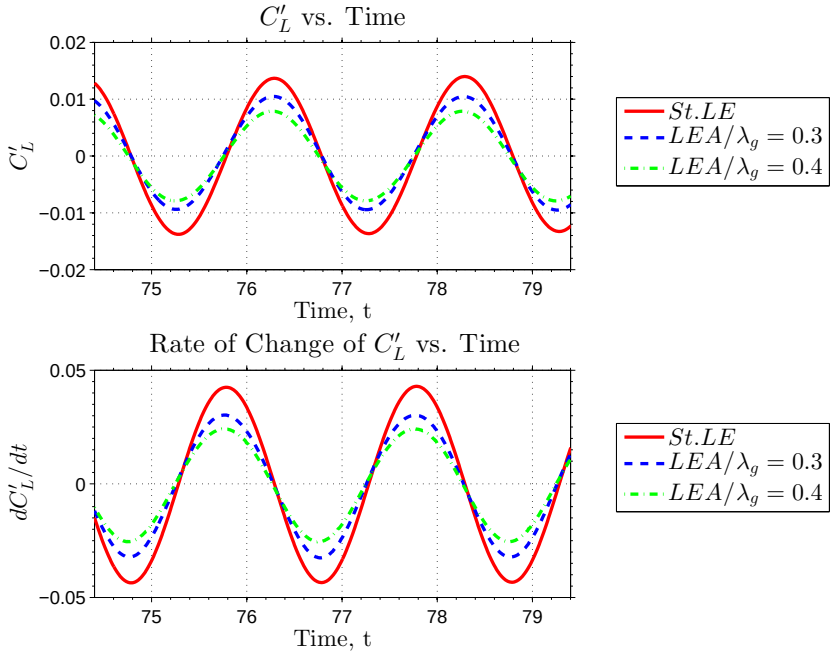

Figure 42: C'_L time signals and rates of change for three different leading edges

the leading-edge area dispersed over the retarded period of time. These local changes brought about by the wavy leading edges in turn lead to a global reduction in the unsteady force acting on the aerofoil surface. The consequence of the reduced AGI noise can be explained by using the loading, or dipole, source term of the FW-H equation. Farassat [98] have derived one of the solutions to the FW-H equation referred to as *Formulation 1A*. The far-field loading noise component of the Formulation 1A solution can be written as

$$4\pi p'_L(\mathbf{x},t) = \int_{l=0} \left[\frac{(\partial p'/\partial \tau)\cos\theta}{c\,r\,(1-M_r)^2} \right]_{ret} dS,$$

where τ is the source or retarded time (details can be found in [98]). This explains that the amplitude of dp'/dt at the source location and time is directly proportional to the magnitude of the propagated sound. Since wavy leading edges reduce the unsteady fluctuations both locally (dp'/dt) and globally (dC'_L/dt), the reduction of AGI noise is a direct consequence as described by the above formula.

5.3 The Effects of α and Aerofoil Thickness

In this section, the effects of α and aerofoil thickness associated with wavy leading edges on the reduction of AGI noise is studied. The same flow-gust condition as used in the previous section is maintained. The gust wavelength is also kept at $\lambda_g = 1L$. Three different angles of attack, $\alpha = 1°$, $2°$ and $3°$, are tested. For this test, the NACA 0015 aerofoil is used and the wavy leading-edge parameters selected are $LEA/\lambda_g = 0.1$ and $LEW/\lambda_g = 0.5$. Figure 43 shows the sound directivity patterns and the profiles of relative noise reduction varying with α. It can be seen from the results that AGI noise level increases with α for both the straight and the wavy leading edge, although the overall

shape of the directivity patterns seems unchanged. Myers and Kerschen [24] analytically predicted that the acoustic power of AGI noise (from a flat plate) increases almost linearly with the angle of attack in $0° \leqslant \alpha \leqslant 3°$ for $M_\infty = 0.5$ (see Figure 5 of [24]). In the meantime, the relative reduction of noise due to the wavy leading edges remains more or less the same. This indicates that the noise reduction capability of wavy leading edges is not significantly affected by the change of α (at least within $0° \leqslant \alpha \leqslant 3°$). An extended study on larger values of α would be useful but nonlinear viscous effects will need to be taken into account, which is beyond the scope of the current study.

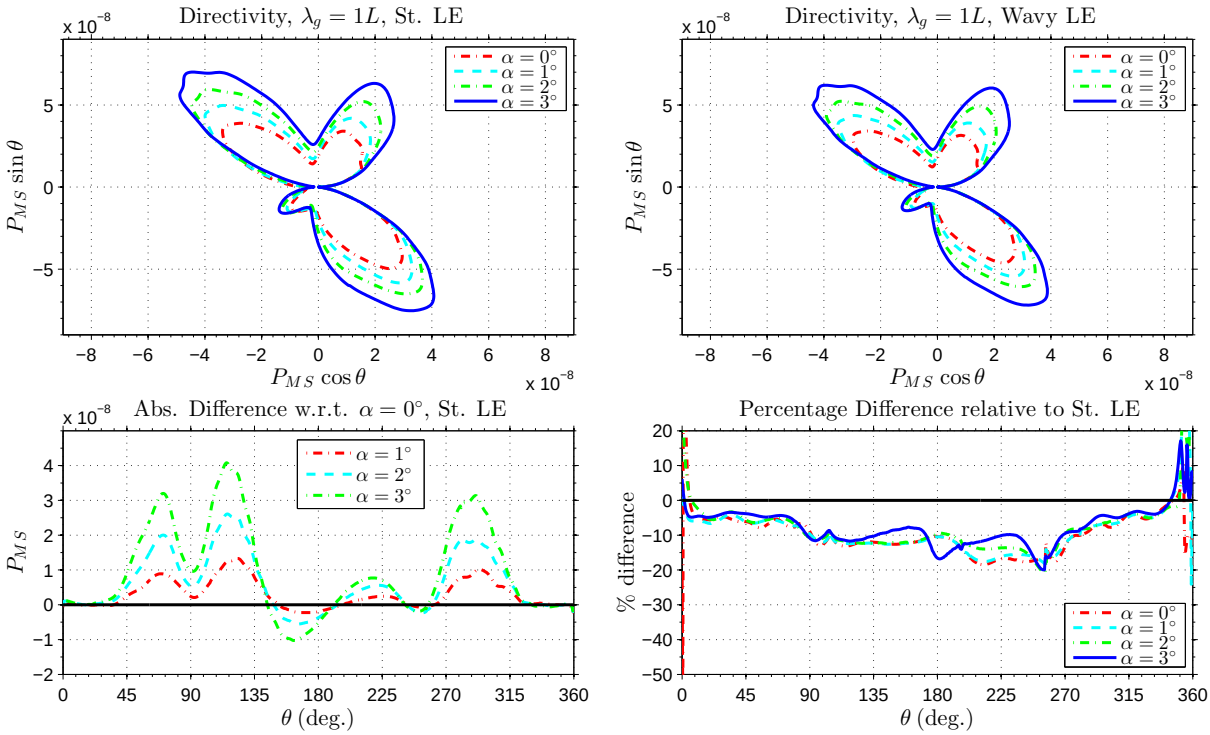

Figure 43: The effect of α on AGI noise: straight LE (left) and wavy LE (right) cases

For studying the effect of aerofoil thickness associated with wavy leading edges, four different values of thickness: NACA 0005, 0010, 0015 and 0020 are used. The same flow-gust condition and leading-edge geometry parameters used in the earlier study are maintained and α is kept at zero. The results are presented in Figure 44. First, it can be seen that there exist remarkable changes in the sound directivity patterns varying with the aerofoil thickness. The main changes take place in the upper half plane for this particular gust condition, and more sound propagates upstream as the aerofoil becomes thicker. The second observation is that the profiles of relative noise reduction due to the wavy leading edges (compared to the straight leading-edge case) still show a strong similarity at $LEA/\lambda_g = 0.1$ despite the substantial differences in thickness.

Another observation from Figure 44 is that the directivity patterns are much closer to being symmetrical about the line $y = 0$ for the thinnest NACA 0005 aerofoil when interacting with the current gust. To investigate this phenomenon, the perturbed vertical and streamwise force coefficients, denoted by C'_{LS} and C'_{DS} respectively, on the upper and lower surfaces of the 3D NACA 0005, 0010 and 0020 aerofoils are calculated. The resulting time variations of C'_{LS} and C'_{DS} for the three aerofoils

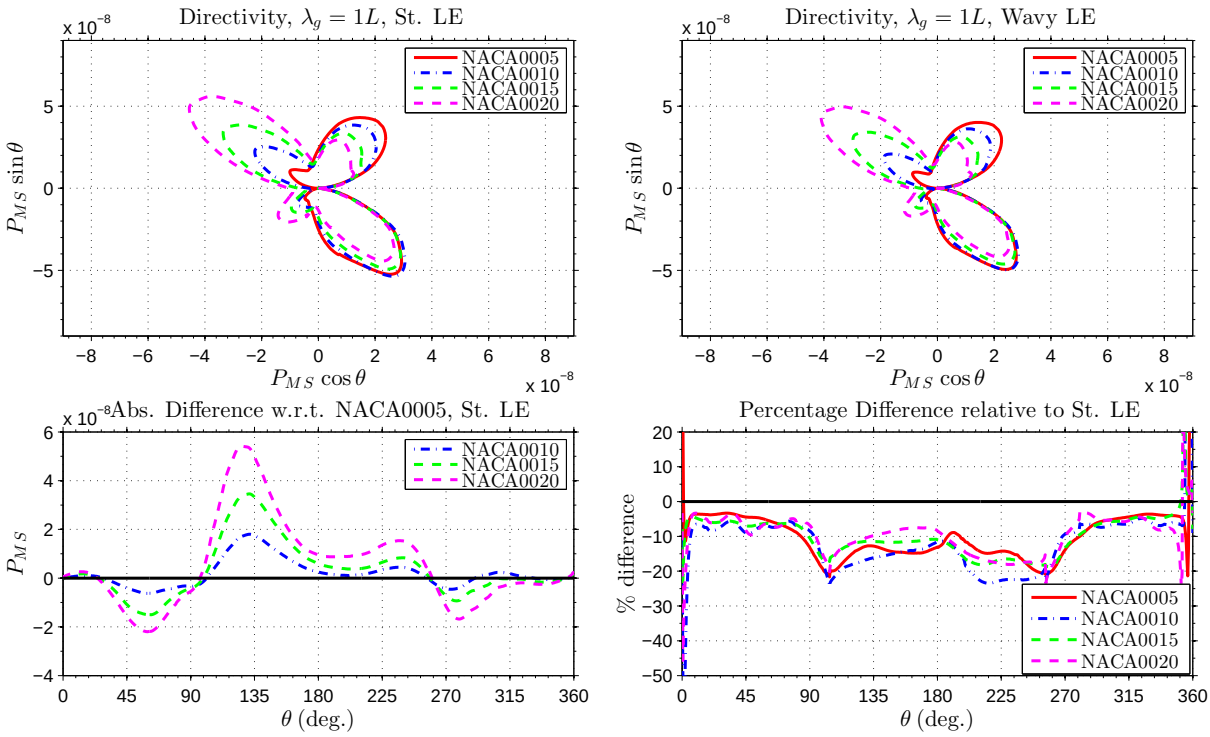

Figure 44: The effect of aerofoil thickness: straight LE (left) and wavy LE (right) cases

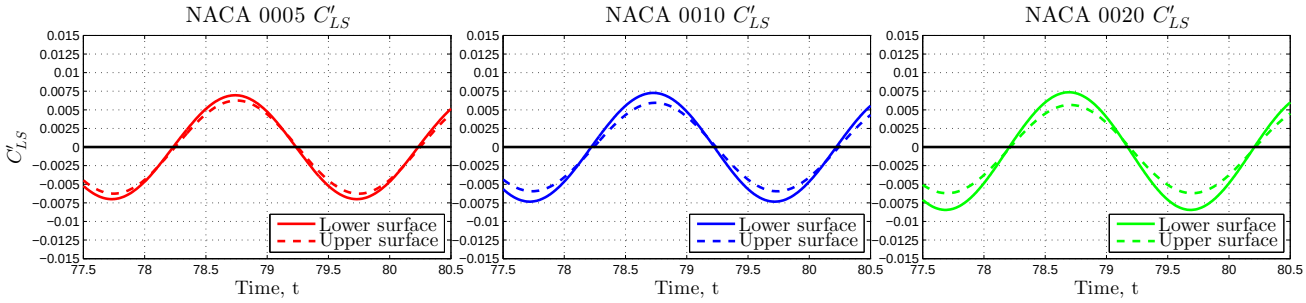

Figure 45: The perturbed vertical force coefficient (C'_{LS}) for the upper and lower aerofoil surfaces

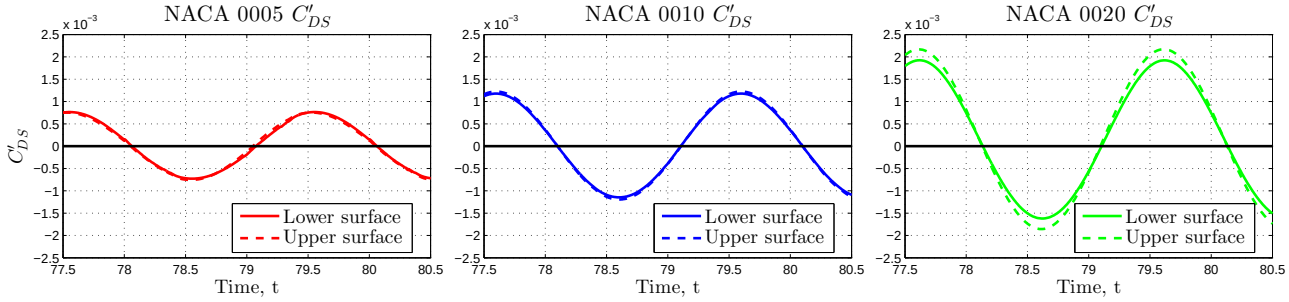

Figure 46: The perturbed streamwise force coefficient (C'_{DS}) for the upper and lower aerofoil surfaces

are plotted in Figures 45 and 46 respectively. Note that these time variations have been adjusted in time so that the signals for the upper and lower aerofoil surfaces are nearly in-phase, and any difference in magnitude between the signals is more clearly shown. It can be seen from Figure 45 that as aerofoil thickness increases, the difference in magnitude between the C'_{LS}-time variations for the upper and lower aerofoil surfaces becomes bigger. Figure 46 shows that for the NACA 0005 and 0010 aerofoils, their respective upper and lower surface C'_{DS}-time variations are nearly identical. For the NACA 0020 aerofoil, the difference in magnitude between the C'_{DS}-time variations for the upper and lower surfaces is more obvious. These results show that as aerofoil thickness increases, the difference in magnitude between the perturbed force time variations for the upper and lower aerofoil surfaces becomes bigger. This leads to the loss of the upper-lower symmetry in the sound directivity pattern as aerofoil thickness increases under the current gust.

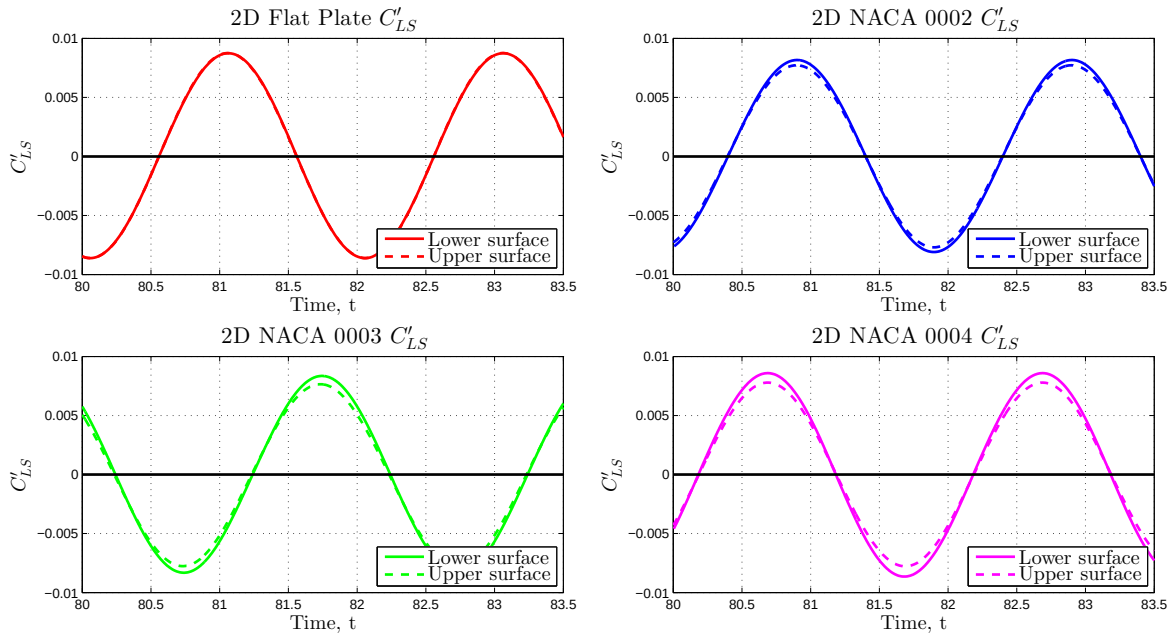

Figure 47: C'_{LS} for the upper and lower surfaces of the four thinner 2D aerofoils

To further show the effects of aerofoil thickness on the radiated AGI noise directivity, the 2D code is used to compute the AGI noise due to eight aerofoils of different thicknesses: NACA 0020, NACA 0015, NACA 0010, NACA 0005, NACA 0004, NACA 0003, NACA 0002 and a flat plate aerofoils. All these eight aerofoils have zero camber, and α is always kept at zero. For this test, $M_\infty = 0.5$ and the perturbed velocity is defined by

$$u'_i = A_i \cos(k_1 x + k_2 y + \omega t) \text{ for } i = 1, 2,$$

where $k_1 = k_2 = 2\pi$ and the amplitude parameters $A_1 = -A_2 = 0.00707$ for the gust to be divergence-free. The resulting time variations of C'_{LS} for the 2D flat plate, NACA 0002, 0003 and 0004 aerofoils are plotted in Figure 47; those for the 2D NACA 0005, 0010, 0015 and 0020 aerofoils are plotted in Figure 48. It is obvious that as aerofoil thickness increases, the difference in magnitude between the C'_{LS}-time variations for the upper and lower aerofoil surfaces becomes bigger. Figure 49 shows the C'_{DS}-time variations for the 2D flat plate, NACA 0002, 0003 and 0004 aerofoils; those for

the 2D NACA 0005, 0010, 0015 and 0020 aerofoils are plotted in Figure 50. It can be seen that the 2D flat plate aerofoil has zero C'_{DS}. This is expected since the flat plate aerofoil has zero thickness and camber ratios and α is always kept at 0°. For each respective aerofoil, the C'_{DS}-time variations for the upper and lower aerofoil surfaces are similar. The 2D NACA 0020 aerofoil shows a somewhat bigger difference in magnitude between the C'_{DS}-time variations for the upper and lower surfaces. In general, these observations are consistent to those for the corresponding 3D aerofoil tests.

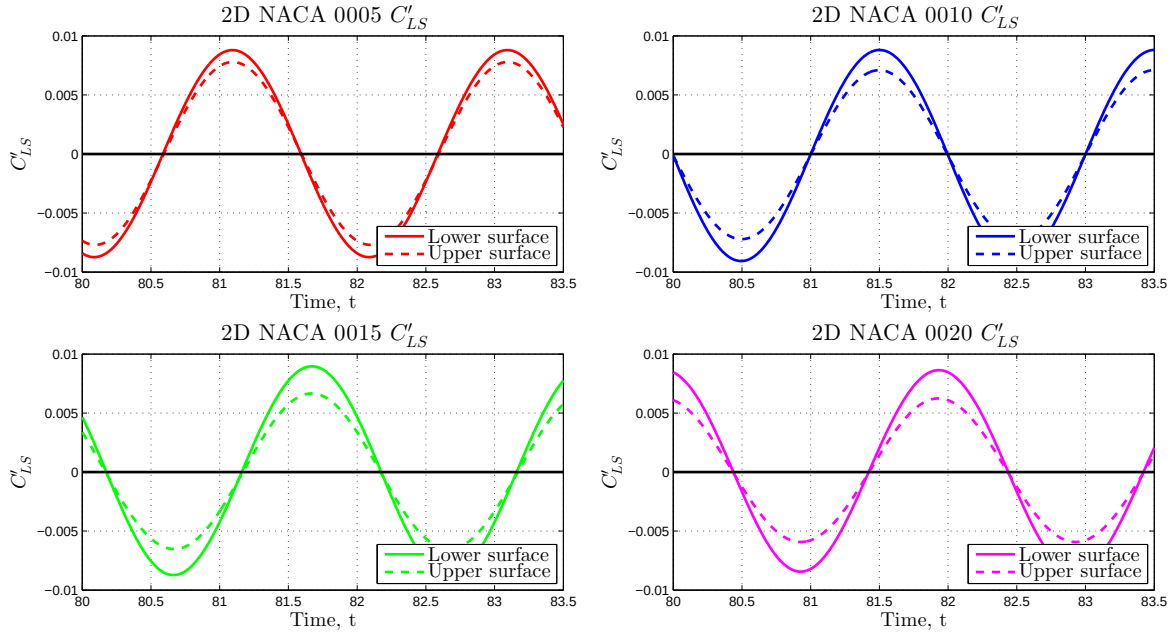

Figure 48: C'_{LS} for the upper and lower surfaces of the four thicker 2D aerofoils

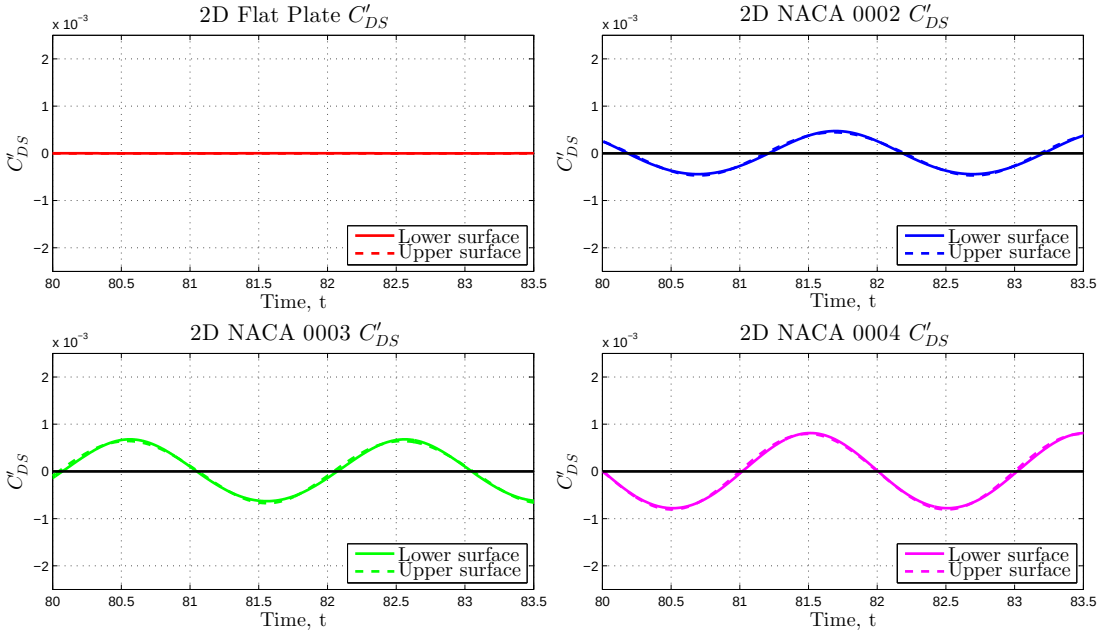

Figure 49: C'_{DS} for the upper and lower surfaces of the four thinner 2D aerofoils

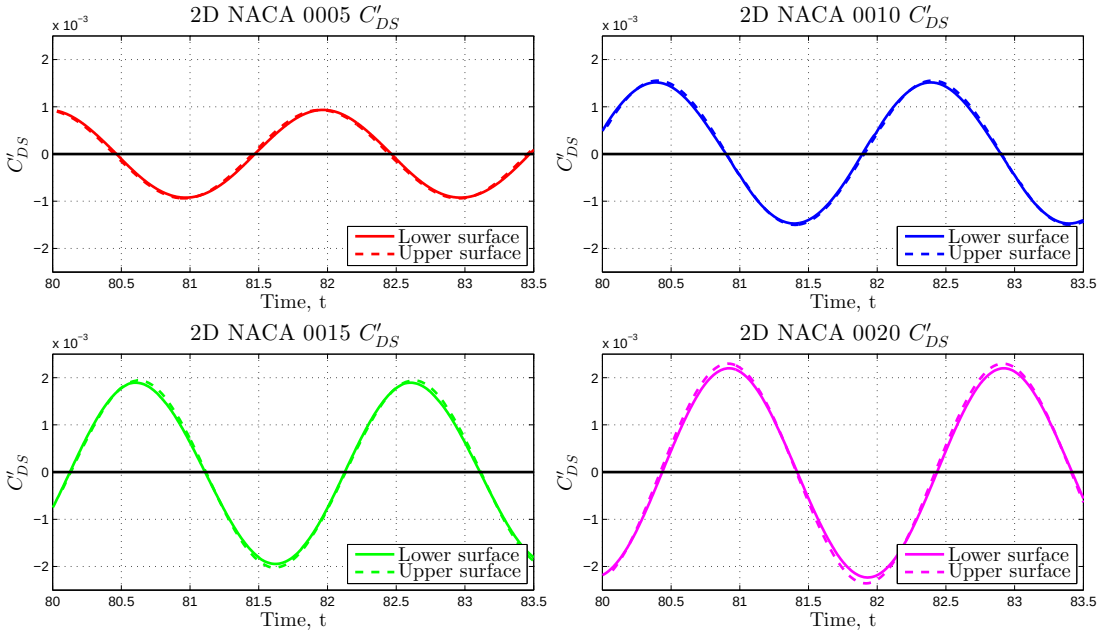

Figure 50: C'_{DS} for the upper and lower surfaces of the four thicker 2D aerofoils

The resulting P_{MS} for the eight 2D aerofoils are also analysed. The P_{MS} directivity patterns and the absolute difference in P_{MS} relative to the 2D flat plate aerofoil are plotted in Figures 51 and 52 respectively. It can be seen from Figure 51 that the flat plate aerofoil produces more noise compared to the thinnest NACA 4-digits aerofoils, and the directivity patterns for the NACA 0003 and 0002 and the flat plate aerofoils are very close to being symmetrical about the line $y = 0$. This upper-lower symmetry is broken as aerofoil thickness increases. This 2D gust is the same as the 3D gust used in this chapter in that the angle that the gust wavefronts make with the streamwise $x-$direction on the $x - y$ plane, referred to as the *gust angle* θ_g herein, is 45°. Figure 53 shows the definition of θ_g, which is related to the gust wavenumbers by $k_2 = k_1 \tan(\theta_g)$. The current 2D results suggest that a gust angle θ_g of 45° and an aerofoil thickness of greater than 3% chord contribute to the lack of upper-lower symmetry in the sound directivity pattern.

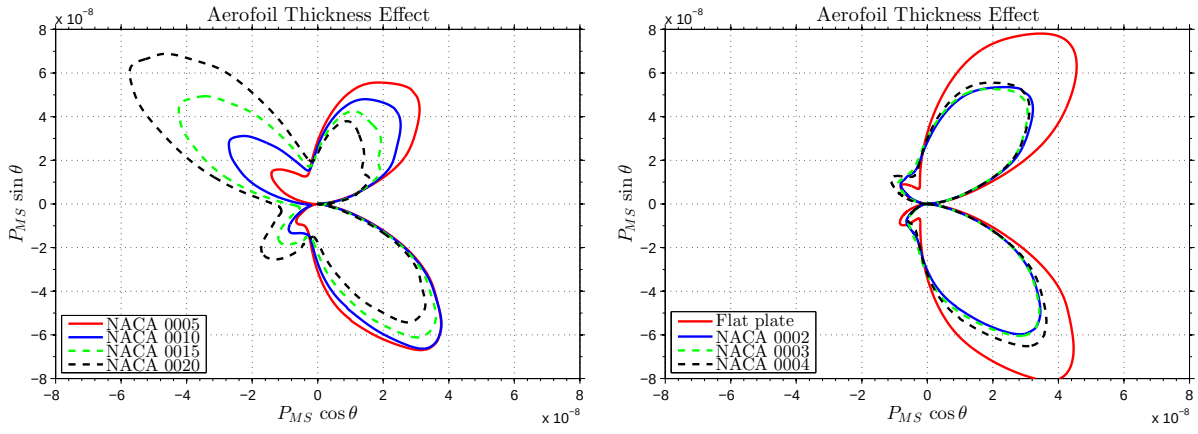

Figure 51: The effect of aerofoil thickness on the upper-lower symmetry of P_{MS} directivity

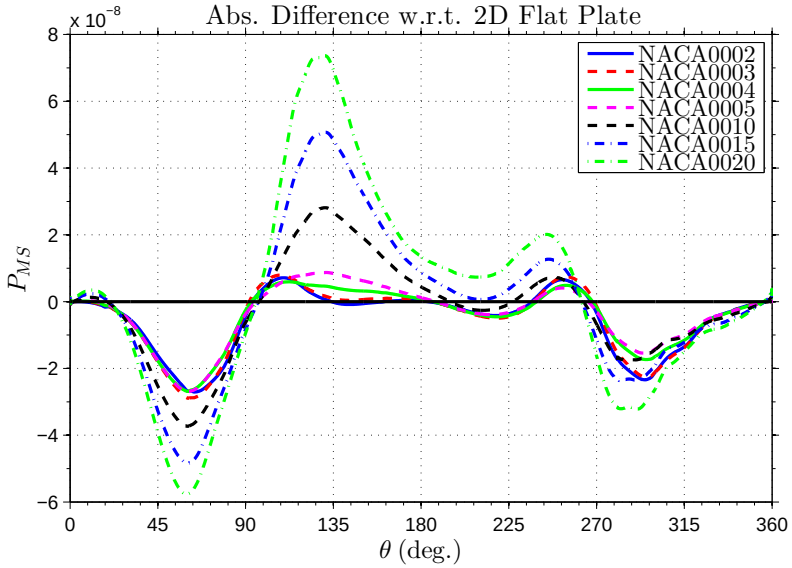

Figure 52: Absolute difference in P_{MS} relative to the flat plate aerofoil

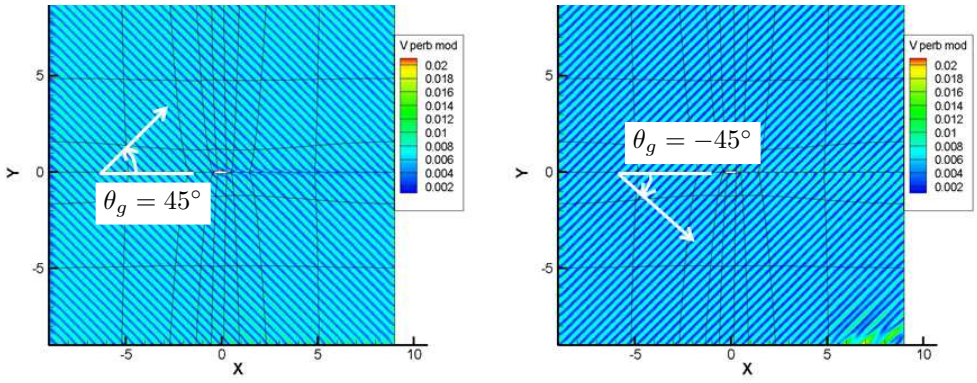

Figure 53: Definition of the gust angle θ_g

Two further tests are conducted to investigate the effects of θ_g on the upper-lower symmetry of the sound directivity pattern. For both tests, $k_2 = 0$ and hence $\theta_g = 0°$, $k_2 = 2\pi$, $M_\infty = 0.5$ and a 3D NACA 0015 aerofoil with $LEA/\lambda_g = 0.3$ and $LEW/\lambda_g = 1.0$ is used. Also, for these two simulations

$$u_1' = A_1 \cos(k_1 x + \omega t) + B_1 \sin(k_1 x + \omega t);$$
$$u_3' = -\left(\frac{\partial u_1'}{\partial x}\right) z,$$

where u_1' and u_3' are the streamwise and spanwise perturbed velocity components respectively, $A_1 = B_1 = 0.005$. One of the tests has $u_2' = 0$, and the other has $u_2' = A_2 \cos(k_1 x + \omega t) + B_2 \sin(k_1 x + \omega t)$ with $A_2 = B_2 = -0.004$. The resulting P_{MS} directivity patterns for these two tests are shown in Figure 54. It can be seen that the directivity pattern for the test with $u_2' = 0$ has a near-perfect upper-lower symmetry, while that for the other test is not symmetrical about $y = 0$ but is closer to achieving upper-lower symmetry than the corresponding case with $\theta_g = 45°$ presented earlier in this chapter (see Figure 29 of section 5.1.1). The effects of aerofoil thickness on AGI noise will be further investigated at a later publication.

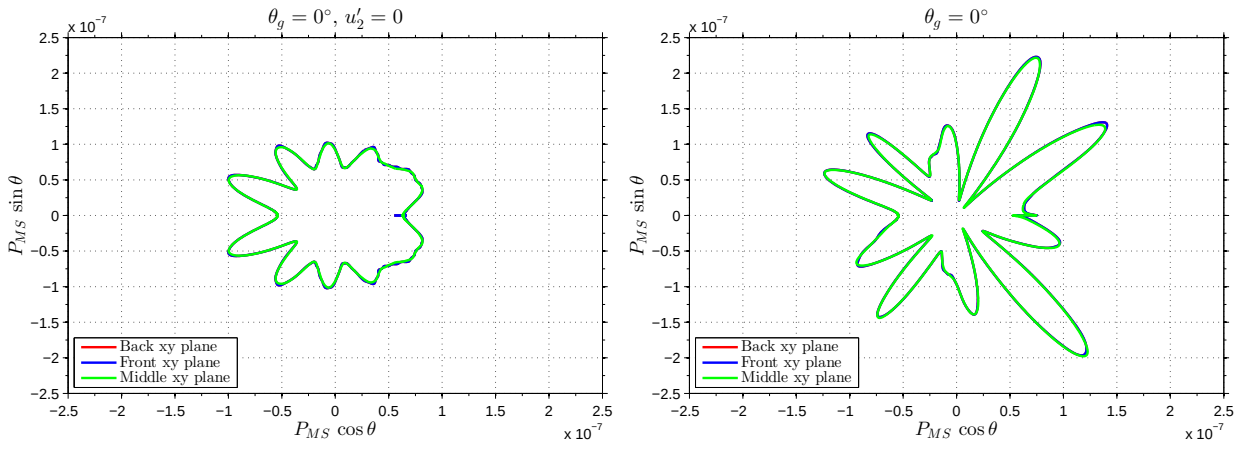

Figure 54: The P_{MS} directivity patterns for the two tests with $\theta_g = 0°$

5.4 The Effects of Multi-mode Gusts

In this section, incident flows with two and four constituent gust-modes are implemented to investigate their combined effects compared to the earlier single-mode cases. The results from this analysis may provide ground for further studies on how the wavy leading-edge geometry can be adjusted or optimised to reduce AGI noise effectively in a real atmospheric turbulence/gust condition.

5.4.1 Two-Mode Gust Condition

The present two-mode incident gust is specified by the parameters listed in Table 6, where $f_g = M_\infty/\lambda_g$ denotes the gust frequency of each mode. The first approach (Eq. (25)) is used to generate the velocity disturbances. The same amplitudes of disturbances are applied to both modes by using the same coefficients $A_1 = B_1 = 0.005$ and $A_2 = B_2 = -0.004$, which is intended for comparison purposes. The freestream Mach number $M_\infty = 0.5$. The NACA 0015 aerofoil is used and two different wavy leading edges named *Wavy LE 1* and *Wavy LE 2* with the same LEA but different LEW are employed, of which the geometric parameters are specified in Table 7. The ratios of the leading-edge parameters to the incident gust wavelengths in each mode are summarised in Table 8.

Gust mode	λ_g	f_g	$k_1 = k_2$
1	$1.0L$	0.50	2π
2	$(2/3)L$	0.75	3π

Table 6: Parameters for two constituent gust-modes used

Name	LEA	LEW
Wavy LE 1	$0.3L$	$1.0L$
Wavy LE 2	$0.3L$	$(2/3)L$

Table 7: Wavy leading-edge parameters used for simulations with a two-mode gust

Gust mode	LEW/λ_g of *Wavy LE 1*	LEW/λ_g of *Wavy LE 2*	LEA/λ_g
1	1.0	$(2/3)L$	0.30
2	1.5	1.0	0.45

Table 8: Parameters of the two wavy leading edges relative to each gust mode

The P_{MS} directivity results of the two-mode gust simulations are shown in Figure 55. It is obvious that the two wavy leading-edge geometries lead to significantly reduced sound levels compared to the straight leading-edge case. However, the difference of noise reduction between the *Wavy LE 1* and *Wavy LE 2* cases is rather insignificant as it is discussed in Section 5.1.2 that LEW has a much less impact on noise reduction than LEA has for the current gust configuration. Most of the noise reduction comes from the effect of LEA as revealed in Section 5.1.1, and it is expected that the noise reduction is more effective against the second gust mode than the first one since the ratio of LEA/λ_g is higher with the second mode. To confirm this, sound pressure spectra are calculated at four different locations shown in Figure 56, and the results are presented in Figure 57. The two spectral peaks at $f_g = 0.5$ and 0.75 correspond to the first and the second gust mode respectively. It can be seen from Figure 57 that both wavy leading edges lead to significant noise reduction at the second mode frequency. Therefore, it is certain that LEA/λ_g plays the major role in AGI noise reduction against multi-mode gusts.

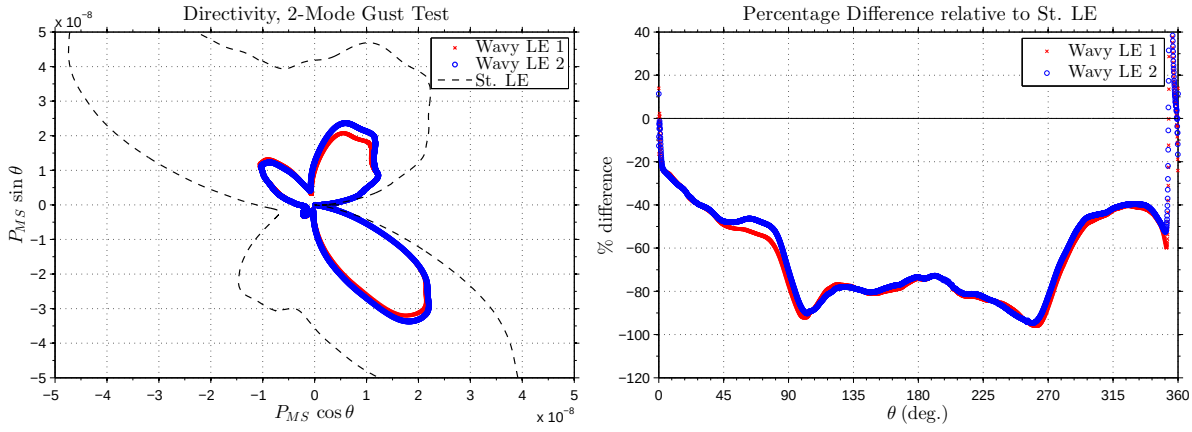

Figure 55: P_{MS} directivity patterns from two-mode gust simulations

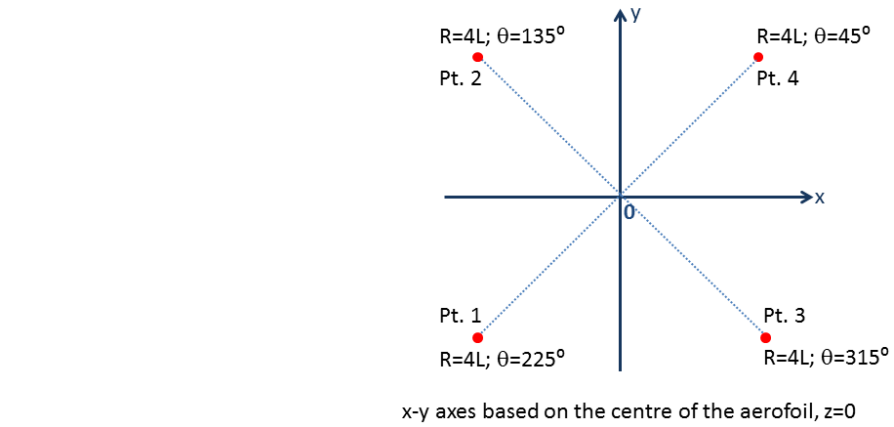

Figure 56: The locations of the four observer points for the calculation of sound pressure spectra

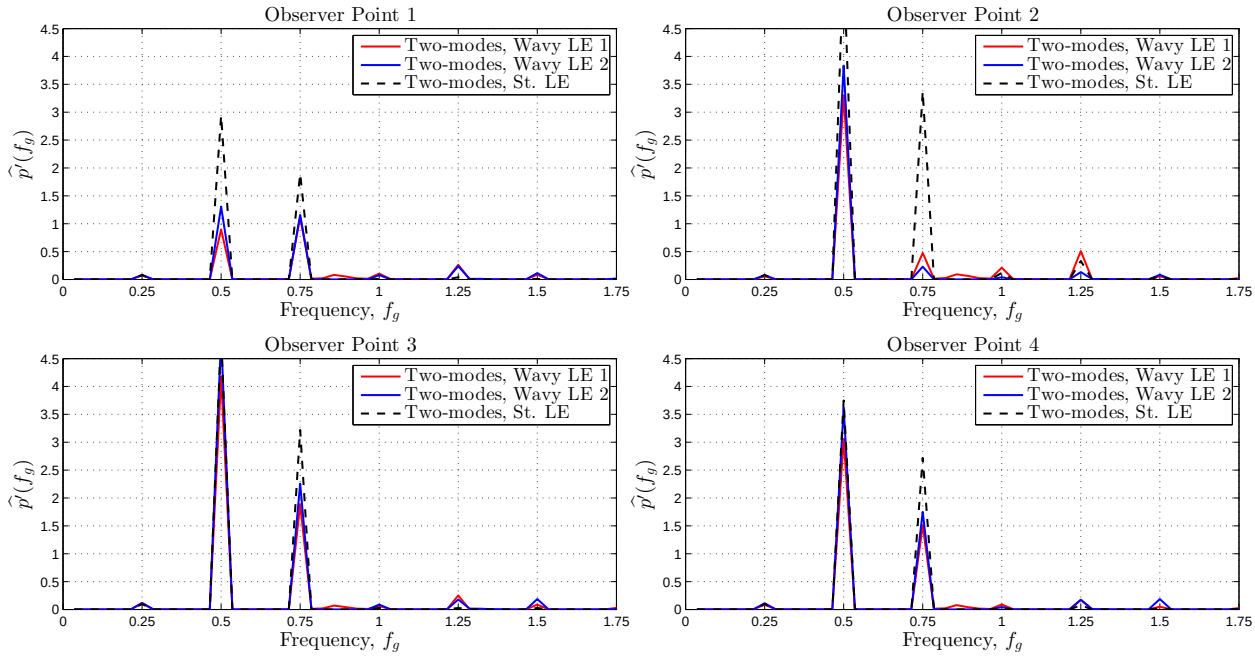

Figure 57: Sound pressure spectra calculated at the four observer locations: two-mode case

The wavy leading edge geometry *Wavy LE 1* is also used for the simulations of AGI noise due to each of the two gust modes prescribed as a single-mode gust. The overall sound pressure spectra due to the two-mode incident gust and the individual spectra due to each of the gust modes as a single-mode gust at the four observer points are plotted on Figure 58. It can be seen that the single peak of each of the individual sound pressure spectra matches perfectly to the peak at the corresponding gust mode frequency of the overall spectrum. This is expected since the perturbed velocity magnitude $|u'|$ used is small (approximately 2.5% of the freestream Mach number), hence the AGI noise produced is linear, i.e. the peaks in the sound pressure spectra are the direct results of the individual gust modes.

A further test is performed using a two-mode gust with the same flow and gust parameters but with larger gust amplitude parameters: $A_1 = B_1 = 0.040$ and $A_2 = B_2 = -0.032$ for each of the two gust modes. Hence the values of A_i and B_i are eight times larger, and the perturbed velocity magnitude

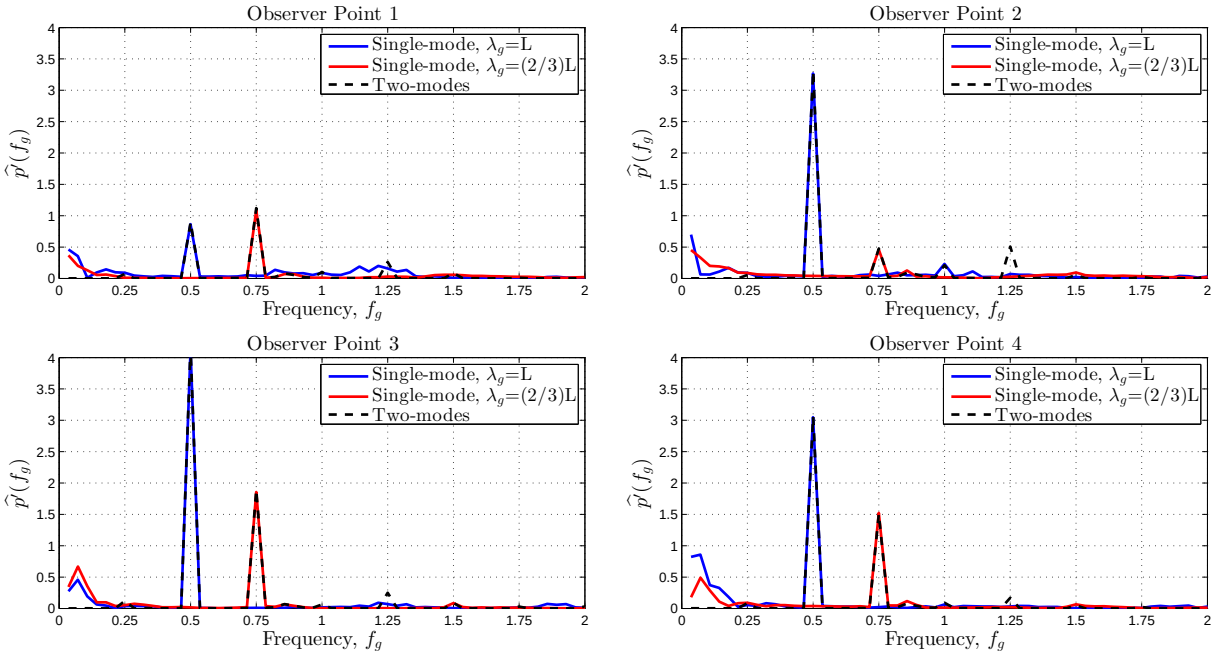

Figure 58: Individual and overall sound pressure spectra calculated at the four observer locations: original-amplitude gusts with *Wavy LE 1*

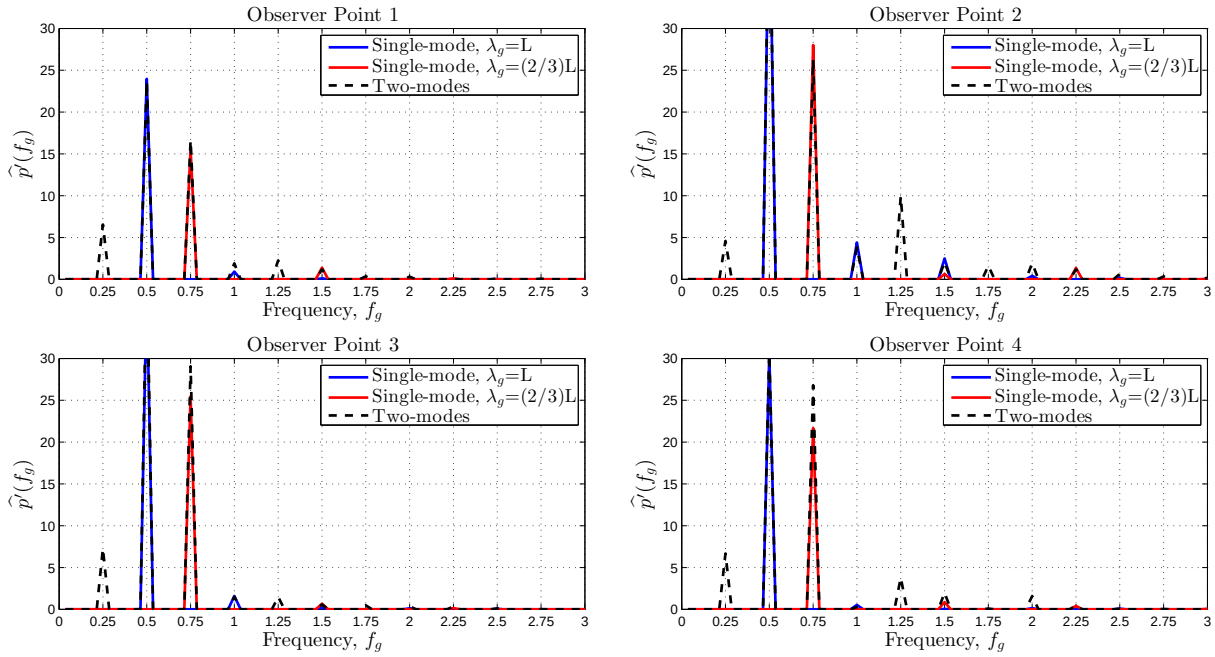

Figure 59: Individual and overall sound pressure spectra calculated at the four observer locations: large-amplitude gusts with straight LE

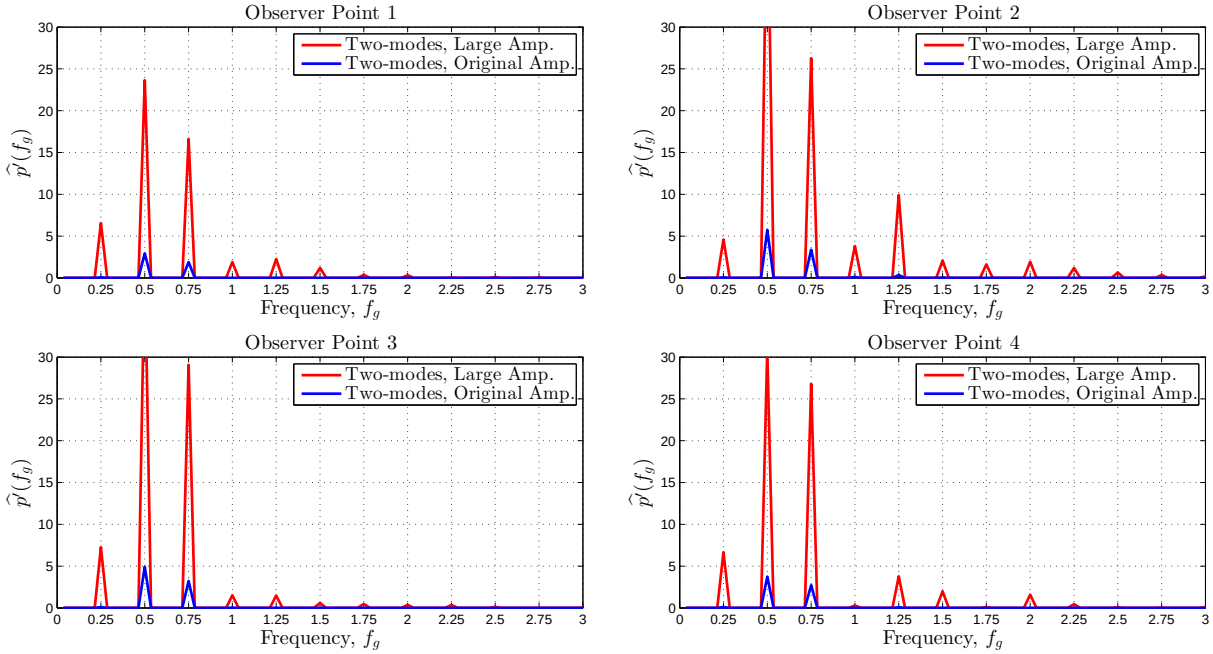

Figure 60: Overall sound pressure spectra at the four observer locations for the large- and the original-amplitude two-mode gusts with straight LE

$|u'|$ is approximately 20% of the freestream Mach number. For this test, 3D NACA 0015 aerofoil with *straight* leading edge is used. The overall sound pressure spectra and the individual spectra with each of the two gust modes prescribed as a single-mode gust are computed and plotted in Figure 59. Compared to the overall sound pressure spectra due to the original-amplitude two-mode gust impinging on a straight leading edge (see Figure 57), the spectra due to the large-amplitude two-mode gust have relatively larger peaks that do not correspond to any of the two constituent gust mode frequencies. The relatively larger growth of these other peaks are evidence of non-linearity in the AGI noise produced. Figure 60 further shows the difference between the overall sound pressure spectra due to the large-amplitude and the original-amplitude two-mode gusts.

5.4.2 Four-Mode Gust Condition

Gust mode	λ_g	f_g	$k_1 = k_2$	LEW/λ_g	LEA/λ_g
1	$2.0L$	0.25	π	0.25	0.075
2	$1.0L$	0.50	2π	0.50	0.150
3	$(2/3)L$	0.75	3π	0.75	0.225
4	$0.5L$	1.00	4π	1.00	0.300

Table 9: Details of the four-mode gust and the LEA/λ_g and LEW/λ_g ratios

Now a four-mode gust is employed in the calculation. One wavy leading edge with $LEA = 0.15L$ and $LEW = 0.5L$ is compared to a straight leading edge in this study. The NACA 0015 aerofoil is still

used. The details of the four constituent gust modes and the values of LEA/λ_g and LEW/λ_g against each mode are listed in Table 9. The same amplitudes of disturbances are applied to all four modes ($A_1 = B_1 = 0.005$ and $A_2 = B_2 = -0.004$). $M_\infty = 0.5$. The resulting P_{MS} directivity patterns at $R = 4L$ are shown in Figure 61 where it is clear again that the wavy leading edge leads to a reduced level of AGI noise in every direction.

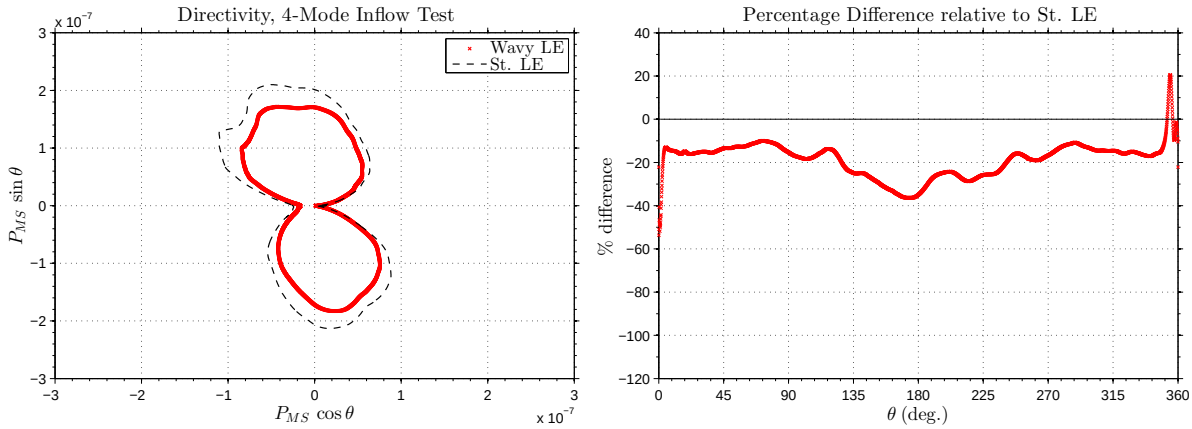

Figure 61: P_{MS} directivity patterns from four-mode gust simulations

In the same way that was demonstrated in the two-mode case, the sound pressure spectra are analyzed at the four observer locations as depicted in Figure 56 in the last section. The resulting spectra are presented in Figure 62 comparing the wavy and straight leading-edge cases. The four major peaks at $f_g = 0.25$, 0.50, 0.75 and 1.00 correspond to each individual mode. The top two spectra for observer points 1 and 2 in Figure 62 clearly show that the noise reduction of the wavy leading edge is predominantly from the two highest frequencies. This is again because the value of LEA/λ_g is larger for a higher gust frequency (smaller λ_g). The same trend is also found in the bottom two spectra although it is not so pronounced since observer points 3 and 4 locate within the region with less significant noise reduction ($\theta \geqslant 315°$ and $\theta \leqslant 45°$ as suggested by the directivity patterns in Figure 61).

Next, the wavy leading edge geometry is used for a further test. The overall sound pressure spectra due to the four-mode incident gust and the individual spectra by each of the four gust modes introduced as a single-mode gust will be compared. The overall and the individual sound pressure spectra at the four observer locations are plotted on Figure 63. It can be seen that the single peak of each of the individual sound pressure spectra matches perfectly to the peak at the corresponding gust mode frequency of the overall spectrum. Hence the AGI noise produced is linear. The effects of wavy leading edges are fully demonstrated and confirmed through multi-mode gust simulations.

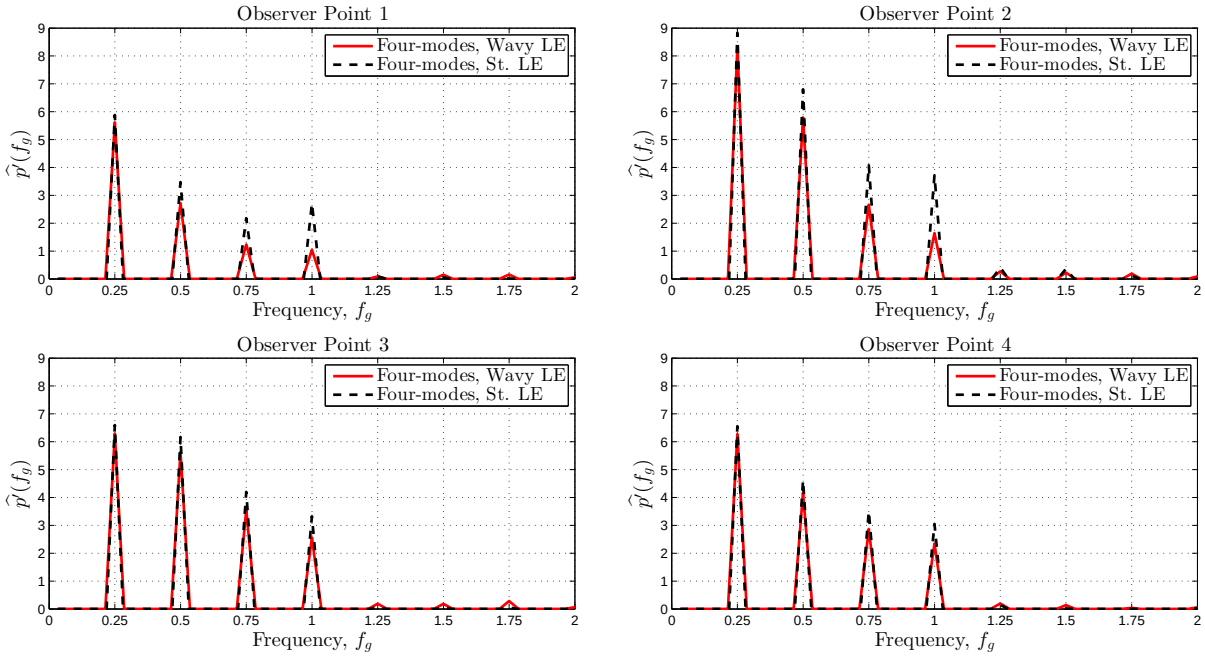

Figure 62: Sound pressure spectra obtained at the four observer locations: four-mode case

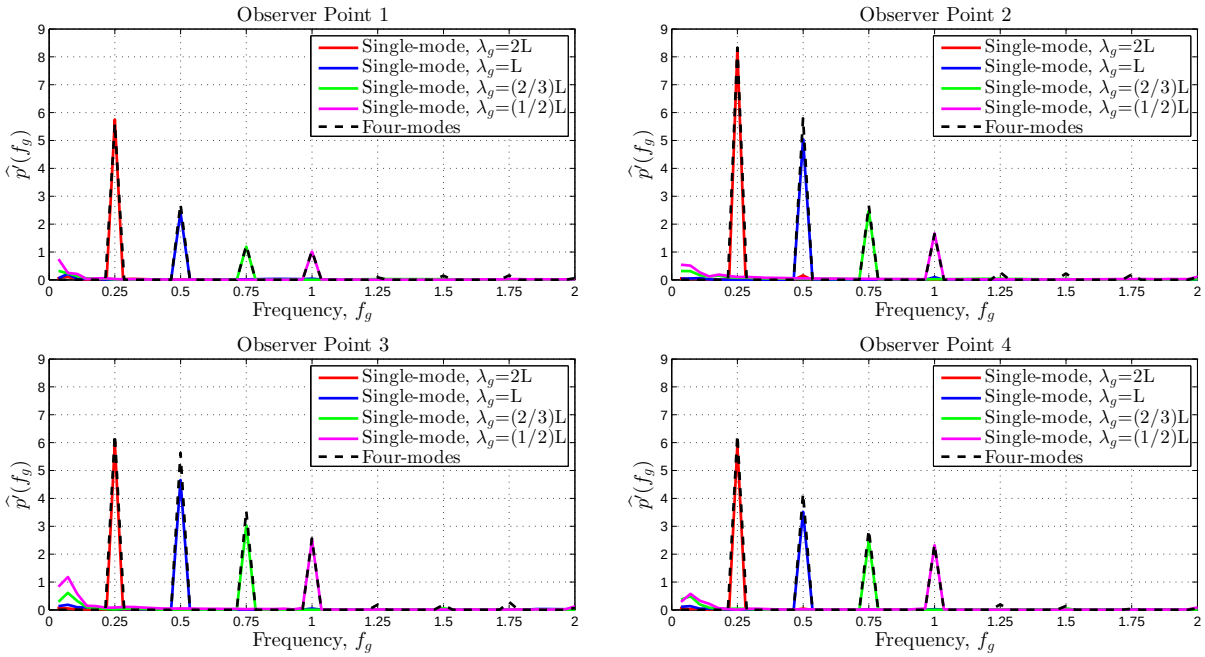

Figure 63: Individual and overall sound pressure spectra calculated at the four observer locations

5.5 The Effects of the Alternative Gust

In this section, the alternative approach to prescribe the incident gust mentioned in Chapter 3.4 is investigated. Based on equations (19) and (20) in Chapter 3.4, a single-mode gust defined by using the alternative approach is given by

$$u_i' = A_i \cos\Omega + B_i \sin\Omega \qquad for \quad i = 1, 2;$$

$$u_3' = -\left(\frac{k_1 A_1 + k_2 A_2}{k_3}\right)\cos\Omega - \left(\frac{k_1 B_1 + k_2 B_2}{k_3}\right)\sin\Omega,$$

with $\Omega = (k_1 x + k_2 y + k_3 z + \omega t)$, where $k_1 = k_2 = k_3 = 2\pi$; $\omega = -k_1 M_\infty$; $M_\infty = 0.5$; $A_1 = B_1 = 0.005$ and $A_2 = B_2 = -0.004$. For this test, four 3D NACA 0015 aerofoils with straight leading edges and different spans: $0.05L$, $0.2L$, $0.5L$ and $1.0L$ are used. The resulting directivity patterns are plotted in Figure 64. It can be seen from the results that the AGI noise level reduces as the simulated span increases from $0.05L$ to $1.0L$. When the simulated span is large, the spanwise variation in the perturbed velocity is fully realised. Then the wavefronts of the perturbed velocity impinge upon the leading edge at an angle on the $x - z$ plane. With $k_3 = 2\pi$, this angle is 45°. This inclination angle between the perturbed velocity wavefronts and the leading edge leads to reduced interaction which results in reduced AGI noise. The sound generated for the case with $LEW = 1.0L$ is so much reduced (in the order of 10^{-10}) that the shape of the directivity pattern is not preserved for this case.

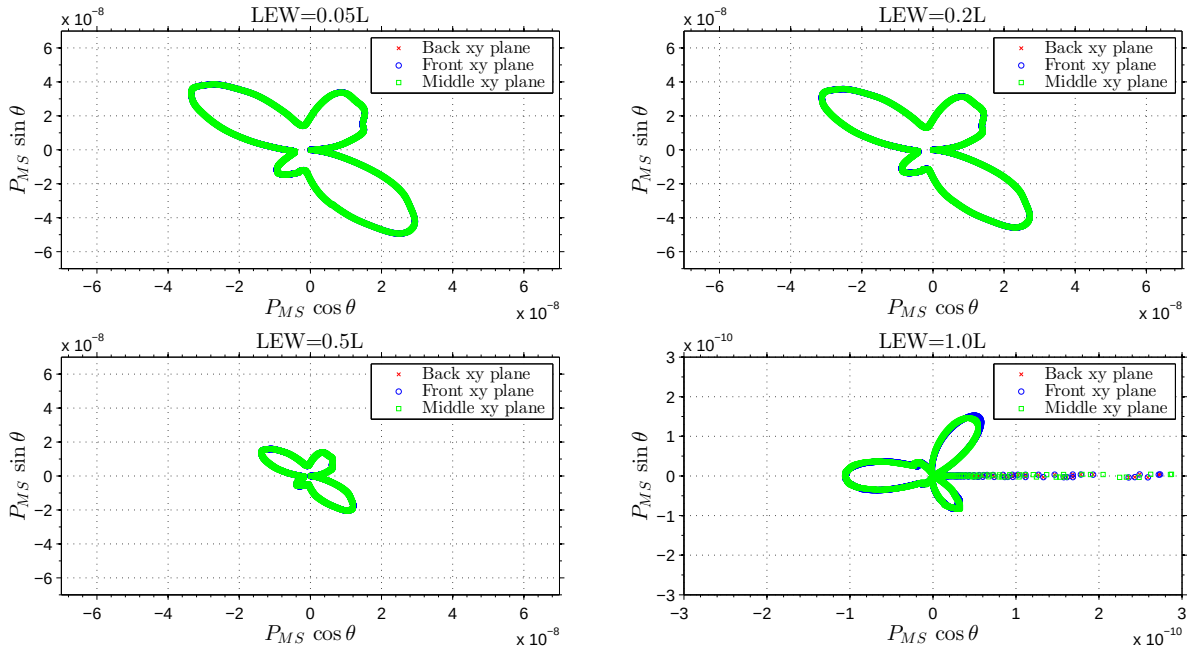

Figure 64: AGI noise due to a gust prescribed by the alternative approach and a st. LE

For comparison purpose, a test which uses the first approach (Eq. (25)) to prescribe the incident gust is conducted. Two 3D NACA 0015 aerofoils with straight leading edges and spans of $0.05L$ and $1.0L$ are used. The resulting directivity patterns are plotted in Figure 65. It is obvious that the two sets of patterns are nearly identical. Hence the first approach to define the incident gust is more appropriate

for the current research as the genuine effects of wavy leading edges can be studied. Examples of the instantaneous contours of $|u'|$ of gusts due to the first and the alternative approaches are shown in Figure 66, where the differences between these two types of incident gust can clearly be seen.

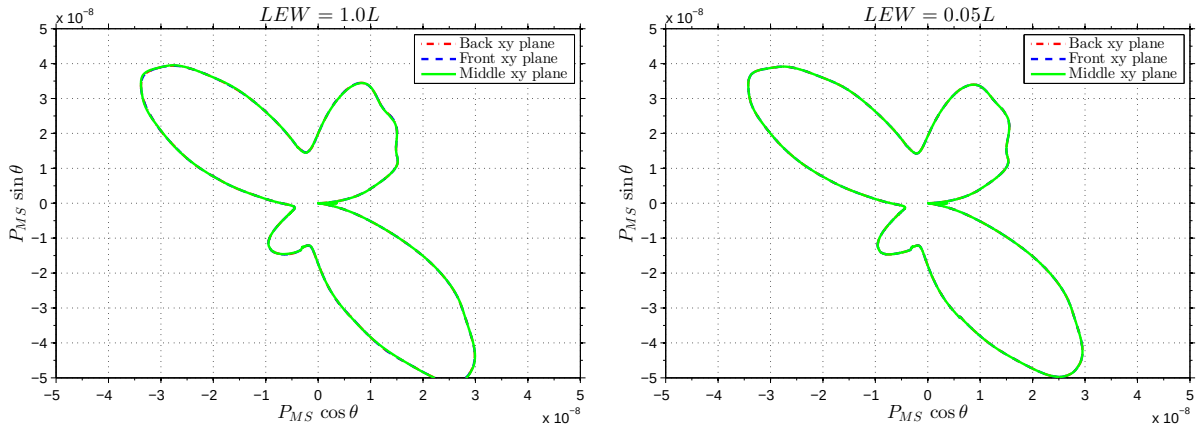

Figure 65: AGI noise due to a gust prescribed by the first approach and a st. LE

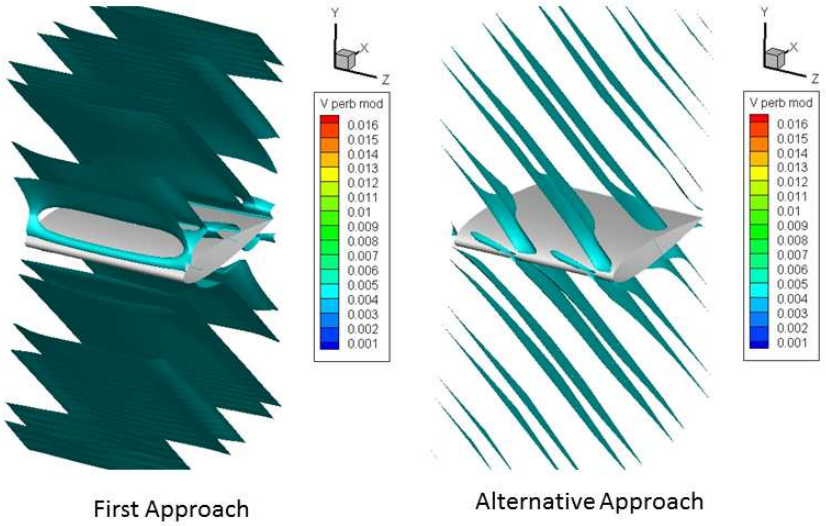

Figure 66: Examples of instantaneous contours of $|u'|$

5.6 Concluding Remarks for 3D Aerofoil Simulations

The present computational results show that the ratio of the peak-to-peak amplitude of wavy leading edges to the longitudinal wavelength of incident gusts, denoted by LEA/λ_g, is the most important factor to characterise the AGI-noise-reducing ability of wavy leading edges under the current type of incident gust. The amount of noise reduction increases with LEA/λ_g and saturates at around $LEA/\lambda_g = 1.0$. It is found that the value of LEA/λ_g at around 0.3 leads to a significant reduction of AGI noise up to 80% or more in a wide range of sound propagation angles. Also, it is conjectured that there exists a strong similarity rule that any two different profiles of relative (normalised) noise reduction (from different leading-edge geometries or incident gusts) match very well together when

they have the same value of LEA/λ_g. In the meantime, the effect of the ratio of the wavelength of wavy leading edges to the longitudinal wavelength of incident gusts, denoted by LEW/λ_g, turns out to be much less significant. This might be due to the fact that the current perturbed velocity components do not vary in the spanwise direction, which results in weak interactions with the spanwise-varying aspect of the wavy leading edges. Nevertheless, it seems that there is a meaningful amount of extra noise reduction when $1.0 \leqslant LEW/\lambda_g \leqslant 1.5$ outside which the effect diminishes. A further study on the effects of LEW/λ_g will be required.

The AGI-noise-reducing mechanism of wavy leading edges has been investigated. It is found that leading-edge waviness induces a de-synchronised gust response in span along the leading edge of the aerofoil. This causes the local pressure fluctuations around the leading-edge area to disperse over the retarded (or source) period of time. The dispersed pressure fluctuations at any spanwise location on a wavy leading edge have smaller amplitudes and time derivatives compared to those at the corresponding location on a straight leading edge. The attenuated level of pressure fluctuations on the aerofoil surface is directly related to a reduced dipole sound according to a solution of the FW-H equation.

Further tests on the AGI-noise-reducing capability of wavy leading edges have been carried out. The test results demonstrate that the relative amount of noise reduction is well maintained for various angles of attack and aerofoil thicknesses. Under the current gust, which has a 45° angle between its wavefronts and the streamwise x-direction on the $x-y$ plane, when the aerofoil thickness increases beyond 3% chord, the symmetry of the sound directivity pattern about the line $y = 0$ will be destroyed. The effectiveness of wavy leading edges is also demonstrated through multi-mode gust tests, which confirm that LEA/λ_g plays the major role in reducing the noise at a constituent gust frequency. For a given leading-edge peak-to-peak amplitude (LEA), higher-frequency gust components are more effectively attenuated since the value of LEA/λ_g is larger. It has also been shown that the first approach to define the incident gust (Eq. (25)) is more suitable than the alternative approach for the current study. In the next chapter, which is the penultimate chapter of the current thesis, the focus will be turned to the simulations of AGI noise for low aspect ratio finite-span wings.

6 Low Aspect Ratio Finite-span Wing Simulations

This chapter aims to show the capability of the current numerical methodology for applications beyond 3D aerofoils. Low aspect ratio finite-span wings are studied. A single-mode incident gust prescribed by using the first approach (Eq. (25)) is employed in this test. The details of the incident gust are shown in Table 10. The freestream Mach number M_∞ used is 0.5.

$k_1 = k_2$	λ_g	f_g	$A_1 = B_1$	$A_2 = B_2$
2π	$1.0L$	0.50	0.005	-0.004

Table 10: The details of the incident gust

Since the current wings are symmetrical about the mid-span $x - y$ plane. Each of them is more like a wing floating in mid-air than an actual wind turbine blade, whose blade tip and root are of different geometry. Significant saving in computational cost can be achieved by only simulating the portion of the wing between the mid $x - y$ plane of symmetry and one of the tips. No-penetration condition is applied for the flow on each of the two spanwise $x - y$ end-planes of the grid. The parameters for the compact filters and the sponge zone are the same as in all the previous chapters.

6.1 Computational Grid

Wing Name	LEA	LEW	Tip Radius
Wavy LE	$0.05L$	$0.15L$	$0.5L$
St. LE	$0.00L$	$0.15L$	$0.5L$

Table 11: The geometric details of the two low aspect ratio finite-span wings

The current grid is generated by a *Fortran90* code that utilises the grid generation method described in Chapter 3.5. The dimensions of the domain on the $x - y$ plane are the same as in all the previous chapters. The main difficulty in the grid generation is the smooth transition between the main span and the tip geometry. For the current grid, the wing tip has a simple semi-circular planform. The cross-sections of the semi-circular tip region are not the same as the main span section. The main span cross-section used for the two wings is the NACA 0005 aerofoil. The geometric details of the two low aspect ratio finite-span wings used in the test are shown in Table 11. Two and a half LEW are incorporated into the leading edge of the main span section of the wings. The wings are straight and un-tapered. With the current grid generation method, the thickness of the wings changes smoothly from the main span to the tip, and the shape of the edge of the tip is such that the transition from the rounded leading edge to the sharp trailing edge occurs smoothly. The general geometry and the shape of the tip edge of the wing with wavy leading edge are shown in Figures 67 and 68. An example of the general block arrangement of the lower half of the grid is shown in Figure 69. The

total number of grid points used for both grids is 23,960,020.

Figure 67: General geometry of the wing with wavy leading edge

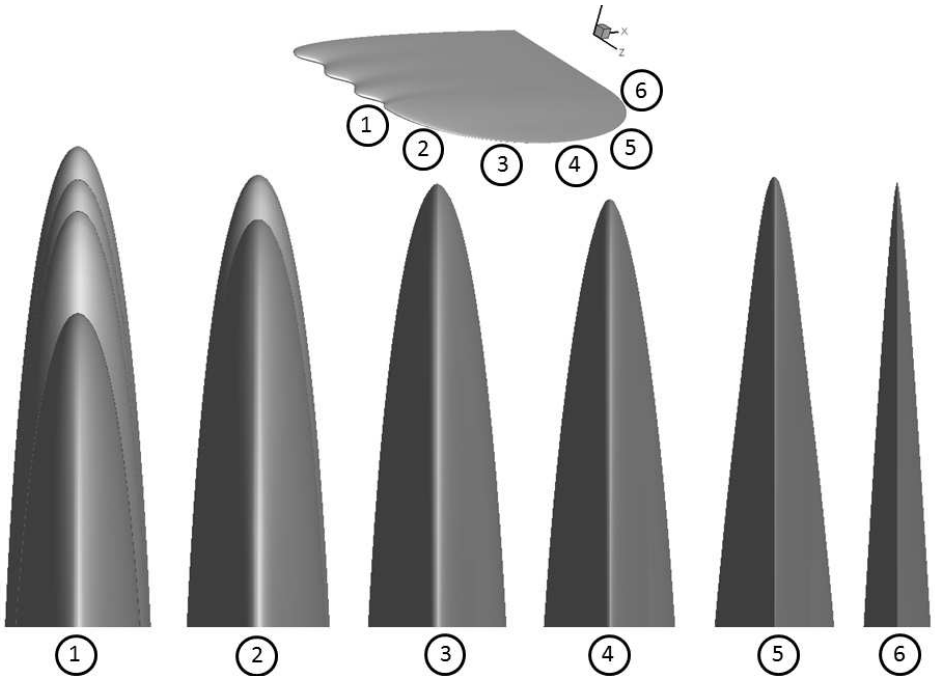

Figure 68: Tip edge shape of the wing with wavy leading edge

6.2 Simulated Aerodynamic Features

For the computations concerning a low aspect ratio finite-span wing, the structure and the block arrangement of the grid are very different to those of the simulations in the previous chapters for 3D

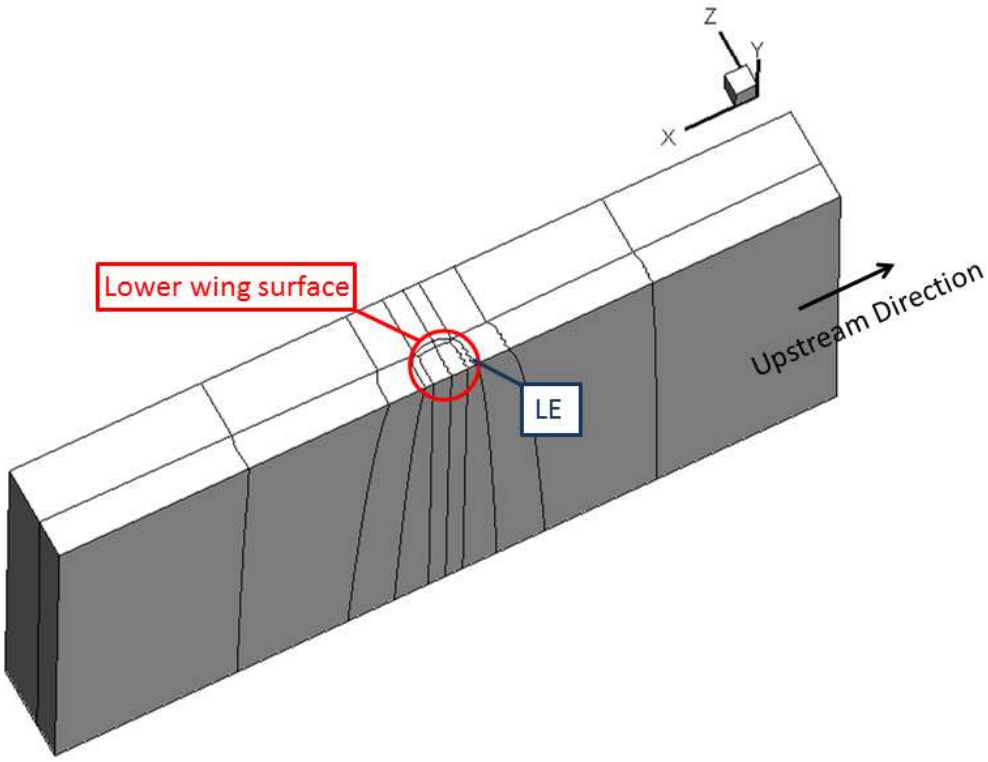

Figure 69: Outline edges of the lower half of the computational grid

aerofoils. Therefore, before looking at the aeroacoustic results, the simulated aerodynamics need to be analysed and compared to those reported in the literature. As reviewed before in Sections 2.5 and 2.6, the flow around a wavy leading edge has several characteristic aerodynamic features: first, the flow velocity in the troughs is higher than that about the peaks on the upper surface of a wing with wavy leading edge [14, 72]; second, because of the higher suction in the troughs, the pressure coefficient in the troughs is lower than that on the peaks [20, 80], about which the pressure coefficient is similar to that of the corresponding wing with straight leading edge [20]. Figure 70 shows the computed mean velocity magnitude contours on the top surfaces of the finite-span wings with and without wavy leading edge. It can be seen that the mean velocity magnitude in the troughs is higher than that about the peaks on the upper surface of the wing with wavy leading edge. This higher top surface suction in the troughs is consistent with the observations reported in the literature. The computed mean surface pressure contours for the two wings with and without wavy leading edge are shown in Figure 71. The lower pressure in the troughs, as observed in many previous studies of wavy leading edges and leading-edge tubercles, is clearly shown by the computed surface pressure contours. These results show that the current code is able to simulate the aerodynamics about the finite-span wing properly. Hence the data obtained from the simulations can be used for the aeroacoustic analysis.

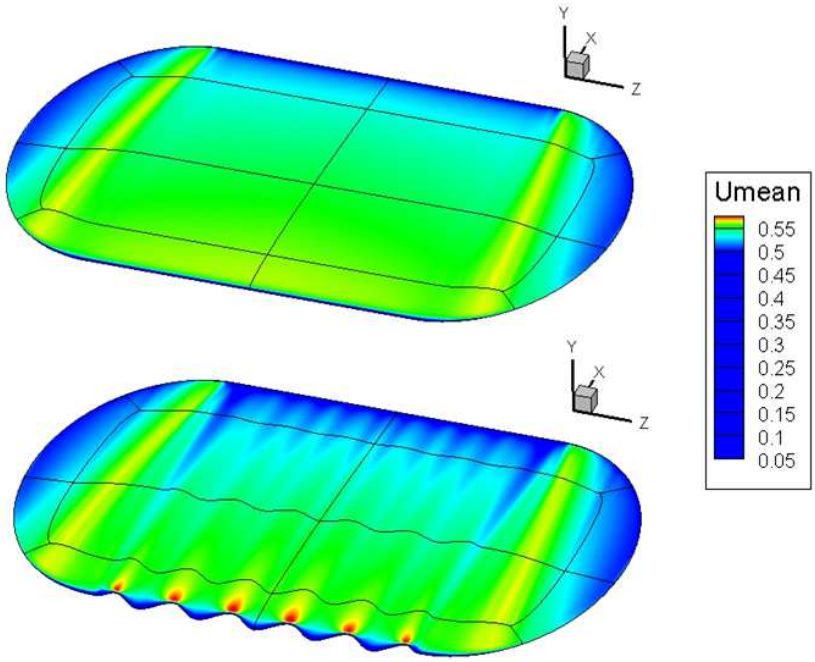

Figure 70: The computed mean velocity magnitude contours on the top surfaces of the two wings

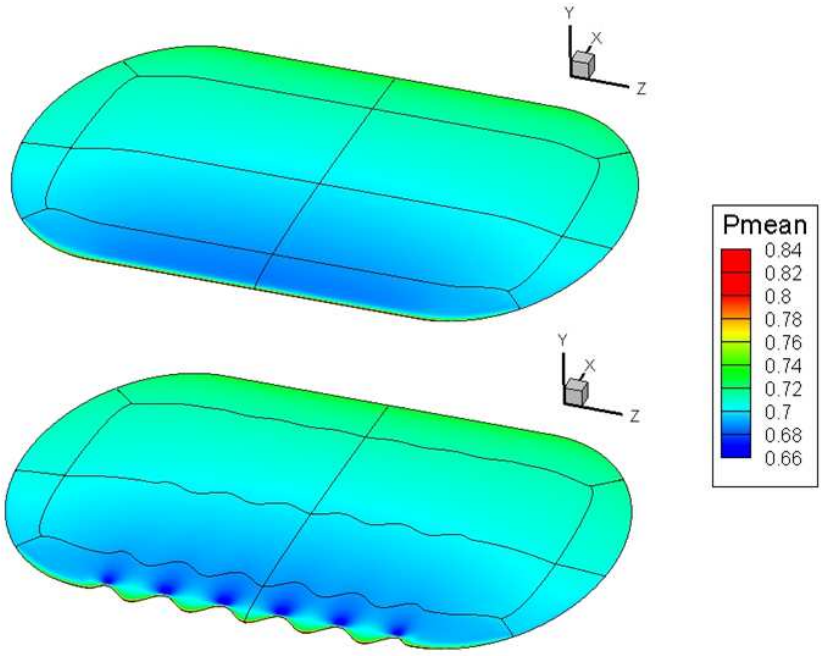

Figure 71: The computed mean pressure contours on the top surfaces of the two wings

6.3 Aeroacoustic Analysis

The P_{MS} directivity patterns at $R = 4L$ on *two* $x - y$ planes located along the main span are computed for the two wings and presented in Figure 72. The locations of the two $x - y$ planes are shown in Figure 73. It can be seen from Figure 72 that the sound due to the two wings with and without wavy leading edge are very similar. The wing with a wavy leading edge shows a very small reduction of AGI noise. This insignificant reduction of AGI noise is due to the small value of LEA/λ_g, which is 0.05 for this test.

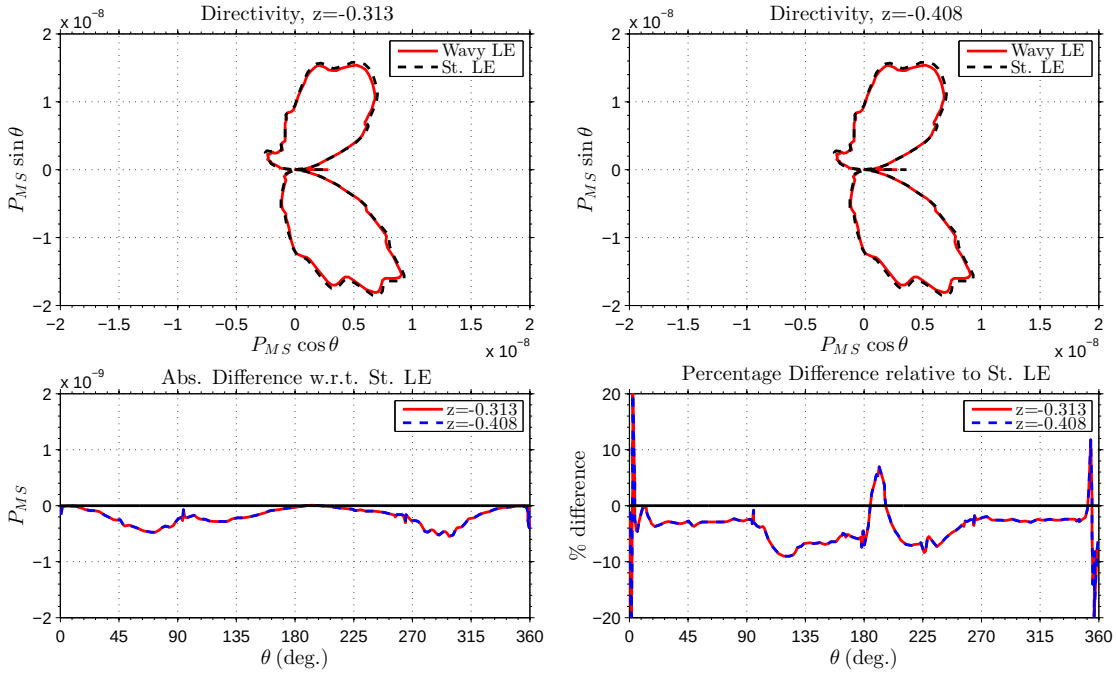

Figure 72: P_{MS} directivity patterns on two $x - y$ planes

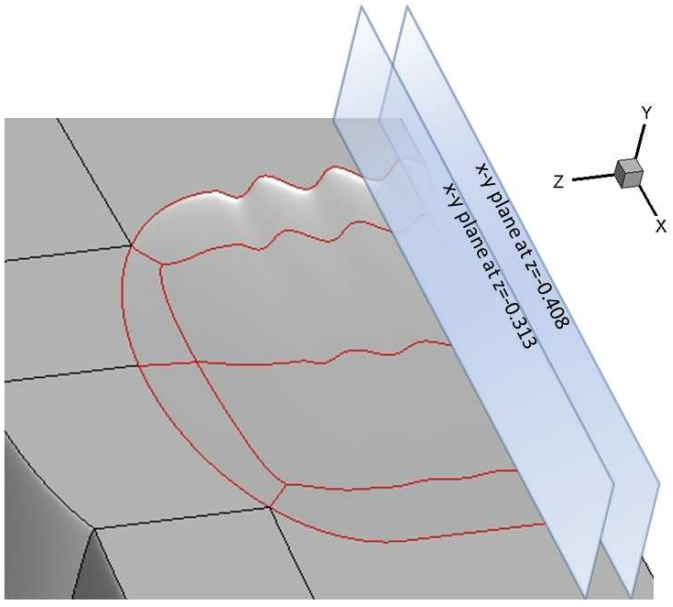

Figure 73: The two output $x - y$ planes for the computation of P_{MS} shown in Figure 72

By comparing the directivity patterns for the finite-span wing with a straight leading edge in Figure 72 with that for a NACA 0005 3D aerofoil with a straight leading edge shown in Figure 44 of Chapter 5.3, it can be observed that the magnitude of P_{MS} due to the finite-span wing is about 2.7 times smaller. The shapes of the directivity patterns for these two cases are similar. The similarity can be explained by the use of the same aerofoil section. The differences are due to the presence of the wing tip, which allows the sound energy to disperse away from the wing in the spanwise direction and leads to a reduced sound level compared to the corresponding 3D aerofoil. The effects of the tip, for example its proximity to the wavy leading edge and its planform shape, on AGI noise need to be further investigated in the future.

Two iso-surfaces and the surface contours of P_{RMS} for the two wings with and without wavy leading edge are shown in Figure 74 and 75 respectively. It can be seen that the P_{RMS} distributions of the two wings are very similar. This similarity has been shown by the P_{MS} directivity patterns in Figure 72. Along the leading edges of the two wings, the level of P_{RMS} is the highest. This shows that for the finite-span wings tested, much of the noise is emitted from the leading edge region. Figures 76 and 77 show planar slices of instantaneous pressure fluctuation contours for the wing with wavy leading edge. Two $x-y$ slices on the main span are shown in Figure 76. While in Figure 77, three $y-z$ slices are shown: one near the leading edge, one near the trailing edge and one slightly aft of the wing. It is obvious from Figures 76 and 77 that the current numerical methodology is able to provide a clean acoustic environment for the AGI noise to develop in all directions within the physical computational domain.

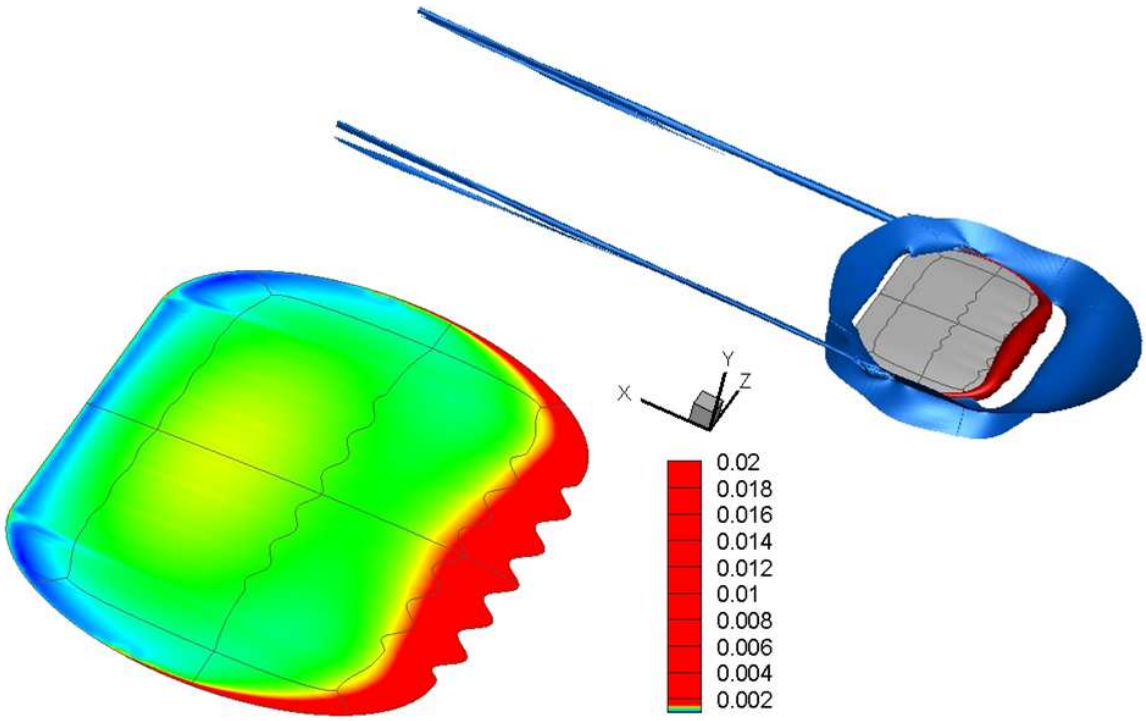

Figure 74: Two iso-surfaces and surface contours of P_{RMS} for the wavy LE wing

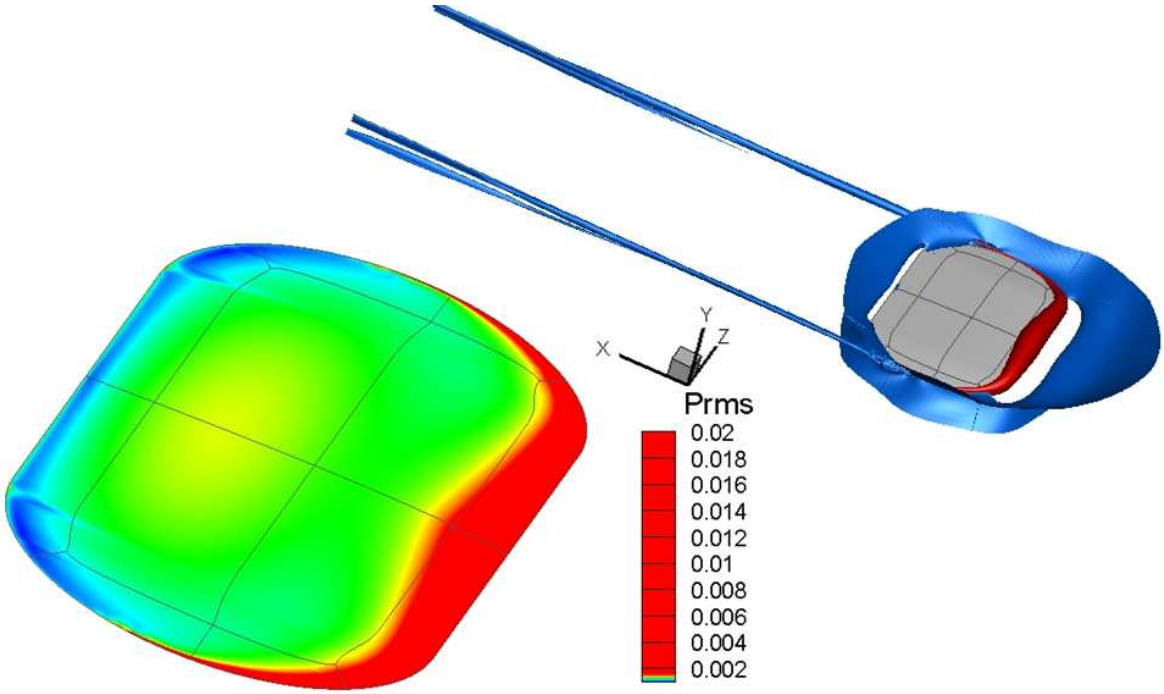

Figure 75: Two iso-surfaces and surface contours of P_{RMS} for the st. LE wing

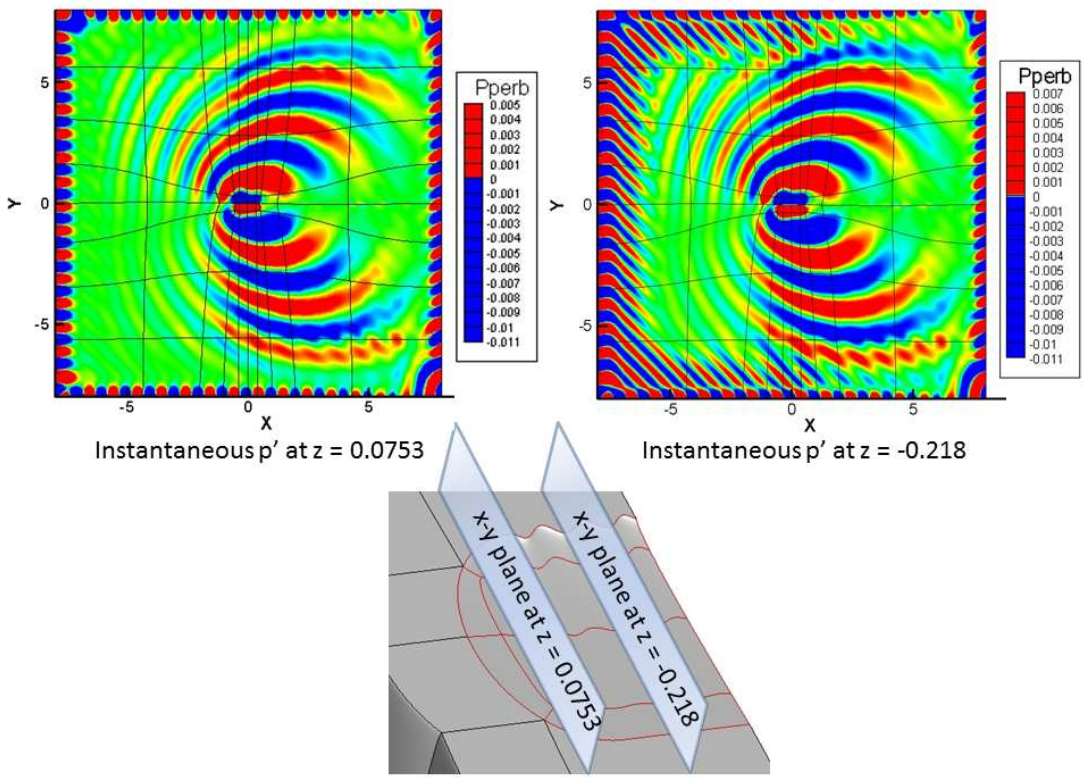

Figure 76: Two $x-y$ slices of instantaneous pressure fluctuation contours for the wavy LE wing

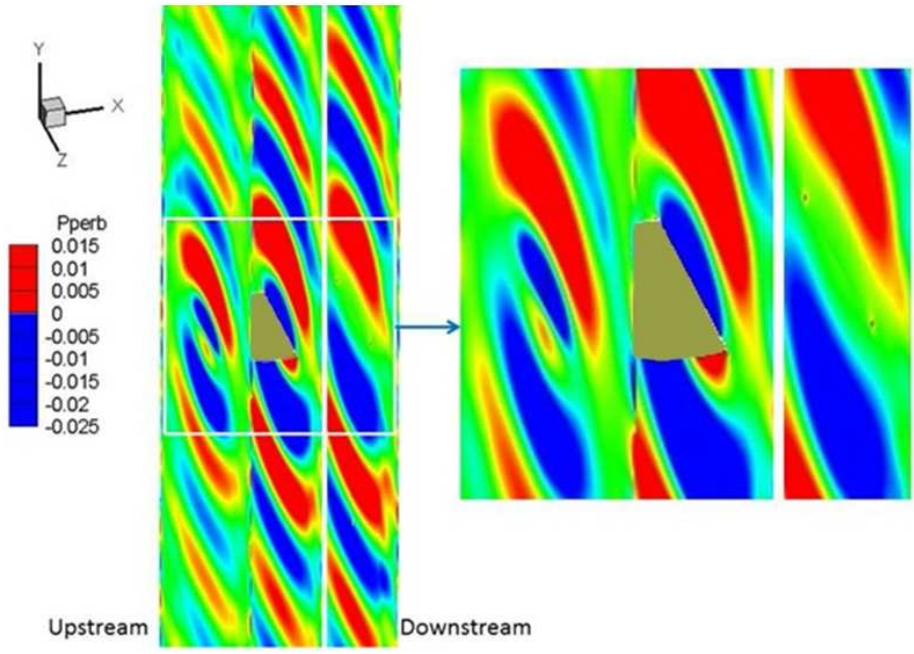

Figure 77: Three $y-z$ slices of instantaneous pressure fluctuation contours for the wavy LE wing

A major difference to the 3D aerofoil cases for the simulation with a finite-span wing can be seen in Figures 74 and 75: there is a long tail of higher P_{RMS} strip, although not as high as the P_{RMS} level along the leading edge, extending from the most distal end of the wing tip to the downstream region. The sound produced along this long trailing strip is shown by the small red dot on the $y-z$ slice of instantaneous pressure fluctuation contour just aft of the wing in Figure 77.

6.4 Concluding Remarks for Finite-span Wings Simulations

The test results presented in this chapter show that the current numerical methodology can be applied to a much more complicated grid structure without many modifications. The current methodology is able to simulate the basic aerodynamics of the flow around a finite-span wing properly. The results indicate that the leading edge region remains the main noise-producing area. With the presence of the wing tip, sound energy is able to disperse away from the wing in the spanwise direction. This leads to a reduced sound level compared to the corresponding 3D aerofoil. Hence the 3D aerofoil simulations represent the acoustic condition far away from the tip, while the low aspect ratio finite-span wing simulations demonstrate the condition very close to the tip. Although the test results for the particular wavy leading edge geometry presented in this chapter do not show significant reduction of AGI noise, it is important to note that the application of leading-edge waviness in close proximity to the wing tip does not lead to an increased noise level. With a higher ratio of LEA/λ_g, it is expected that the wavy leading edge will be able to reduce the AGI noise more significantly. Nevertheless, the capability and potential of the current methodology have been demonstrated clearly by the numerical results presented in this chapter.

7 Final Conclusions and Future Works

The current research employs an accurate and efficient numerical methodology to investigate the AGI noise caused by the interaction of the leading edge with the incident gust. The high-order discretisation methods used to solve the governing compressible Euler equations numerically have been explained in details in the current thesis. The success of the current numerical methodology relies on the ability of the current boundary conditions to provide a clean acoustic environment for genuine AGI noise to develop. The current sponge zone boundary conditions are used to introduce the incident gusts into the computational domain, and to minimise the non-physical characteristic wave reflection at the domain boundaries. The current incident gusts are periodic, 3D and divergence-free. Furthermore, the current grid generation method is able to create high-quality grids which are very suitable for CAA applications. Therefore, the current numerical methodology is highly suitable for the study of the effects of wavy leading edges on AGI noise.

Four validation studies for the current methodology have been presented in this thesis. The first two validation cases involve 2D aerofoils. First, a benchmark problem regarding the acoustic response of a Joukowski aerofoil under a simple periodic gust is chosen from the Third [55] and the Fourth [56] CAA Workshops for comparison purposes. Then, the theoretical results proposed by Myers and Kerschen [24] on AGI noise are compared with the current numerical results. The last two validation cases involve 3D aerofoils. First, the computed total lift coefficients C_L at small angles of attack ($-1^\circ \leqslant alpha \leqslant 3^\circ$) for a 3D NACA 0015 aerofoil are compared to those measured by Sheldahl and Klimas [95] experimentally. The effects of different incident flows and different wavy leading-edge geometries on the computed C_L have also been investigated. The second 3D aerofoil validation study employs qualitative comparisons of the computed 3D aerofoil surface mean pressure and velocity distributions with the mean aerodynamic features reported in the literature for wavy leading edges. The results of these four validation studies show that the current methodology is accurate, efficient and robust. Hence it can be used with confidence for the investigation of the effects of wavy leading edges on AGI noise.

For 3D aerofoils under the current type of incident gust defined using the first approach (Eq. (25)), the present computational results show that the ratio of the peak-to-peak amplitude of wavy leading edges to the longitudinal wavelength of incident gusts, denoted by LEA/λ_g, is the most important factor to characterise the AGI-noise-reducing ability of wavy leading edges. The amount of noise reduction increases with LEA/λ_g and saturates at around $LEA/\lambda_g = 1.0$. It is found that the value of LEA/λ_g at around 0.3 leads to a significant reduction of AGI noise up to 80% or more in a wide range of sound propagation angles. Also, the current results from simulations with different leading-edge geometries and incident gusts support a strong similarity rule that any two different profiles of relative (normalised) noise reduction match very well together when they have the same value of LEA/λ_g. The effect of the ratio of the wavelength of wavy leading edges to the longitudinal wavelength of incident gusts, denoted by LEW/λ_g, turns out to be much less significant. This might be due to the fact that the current perturbed velocity components do not vary in the spanwise (z-) direction, which results in weak interactions with the spanwise-varying aspect of the wavy leading

edges. Nevertheless, it seems that there is a meaningful amount of extra noise reduction when $1.0 \leqslant LEW/\lambda_g \leqslant 1.5$ outside which the effect diminishes. A further study on the effects of LEW/λ_g will be required.

The AGI-noise-reducing mechanism of wavy leading edges has been investigated. It is found that leading-edge waviness induces a de-synchronised gust response in span along the leading edge of the aerofoil. This causes the local pressure fluctuations around the leading-edge area to disperse over the retarded (or source) period of time. The dispersed pressure fluctuations at any spanwise location on a wavy leading edge have smaller amplitudes and time derivatives compared to those at the corresponding location on a straight leading edge. The attenuated level of pressure fluctuations on the aerofoil surface is directly related to a reduced dipole sound according to a solution of the FW-H equation.

Further tests on the AGI-noise-reducing capability of wavy leading edges have been carried out. It is found that for various angles of attack and aerofoil thicknesses, the relative amount of noise reduction due to wavy leading edges is well maintained. Under the current gust, which has a 45° angle between its wavefronts and the streamwise x-direction on the $x - y$ plane, when the aerofoil thickness increases beyond 3% chord, the symmetry of the sound directivity pattern about the line $y = 0$ will be destroyed. The effectiveness of wavy leading edges is also demonstrated through multi-mode gust tests, which confirm that LEA/λ_g plays the major role in reducing the noise at a constituent gust frequency. For a given leading-edge peak-to-peak amplitude (LEA), higher-frequency gust components are more effectively attenuated since the value of LEA/λ_g is larger. It has also been shown that the first approach to define the incident gust (Eq. (25)) is more suitable than the alternative approach for the current study.

Finally, the capability of the current methodology to simulate the AGI noise due to a low aspect ratio finite-span wing has been demonstrated. The current methodology is able to simulate the basic aerodynamics of the flow around the finite-span wing properly. The main aim of the low aspect ratio finite-span wing simulations presented is to demonstrate the effect of leading edge waviness very close to the tip. Although significant AGI noise reduction is not observed for the particular wavy leading edge geometry tested, it is expected that a more significant reduction will be brought about by the use of a wavy leading edge with a larger value of LEA/λ_g.

The robustness of the current numerical methodology is also shown by the fact that for all the validations and tests presented in the this thesis, the same filter and sponge zone parameters have been used throughout. Hence the current numerical recipe can be used without many modifications for a wide range of problems. The principal findings of the current research are as follows

- under the current gust defined by the first approach (Eq. (25)), the ratio of the peak-to peak amplitude of the wavy leading edge to the longitudinal wavelength of the incident gust, denoted by LEA/λ_g, is the most important factor in reducing AGI noise;

- the amount of noise reduction increases with LEA/λ_g and saturates at around $LEA/\lambda_g = 1.0$;
- $LEA/\lambda_g \geqslant 0.3$ leads to a significant AGI noise reduction of more than 80% relative to the straight leading edge case in a wide range of sound propagation angles;
- similarity in the profiles of relative (normalised) noise reduction for cases which have the same value of LEA/λ_g has been identified;
- under the current gust, the effect of the ratio of the wavelength of the wavy leading edge to the longitudinal wavelength of the incident gust, denoted by LEW/λ_g, is much less significant than LEA/λ_g;
- a meaningful amount of extra noise reduction when $1.0 \leqslant LEW/\lambda_g \leqslant 1.5$ is observed;
- the de-synchronised gust response in span along a wavy leading edge leads to a reduced level of both pressure fluctuation and its time derivative, which causes a reduction in the resulting AGI noise level;
- for the various angles of attack and aerofoil thicknesses tested, the relative amount of noise reduction due to wavy leading edges is well maintained;
- the multi-mode gust tests confirm that LEA/λ_g plays the major role in reducing the noise at a constituent gust frequency;
- the close proximity of the wavy leading edge to a wing tip does not lead to higher AGI noise level.

7.1 Future Works

The accuracy, efficient and robustness of the current numerical methodology for the study of AGI noise have been shown. Hence, it is envisaged that with a few modifications, the current methodology can be used for studies that are more directly relevant to wind turbine noise research. For example, the AGI noise emitted due to the interaction of a rotating wind turbine blade with the atmospheric wind gust, or the unsteady flow aft of a number of upstream wind turbines in a wind farm. For these simulations, a more sophisticated atmospheric wind gust model and a more complicated grid are required. The effects of multi-scale leading edge waviness, which employs more than one set of LEA and LEW in a certain combination, on AGI noise can also be investigated. For a rotating wind turbine blade, due to the variation of the linear velocity along the span, the optimal values of LEA and LEW at different spanwise locations are different. Hence multi-scale leading edge waviness represents an interesting future research topic.

References

[1] G. Guidati, J. Ostertag, and S. Wagner, "Prediction and reduction of wind turbine noise: an overview of research activities in Europe," in *19th ASME Wind Energy Symposium, 38th Aerosp. Sci. Meeting and Exhibit*, 2000.

[2] P. Morris, L. Long, and K. Brentner, "An aeroacoustic analysis of wind turbines," in *42nd AIAA Aerosp. Sci. Meeting and Exhibit*, 2004.

[3] O. Fleig, M. Iida, and C. Arakawa, "Wind turbine blade tip flow and noise prediction by large-eddy simulation," *J. Sol. Energy Eng.*, vol. 126(4), pp. 1017–1024, 2004.

[4] C. Arakawa, O. Fleig, M. Iida, and M. Shimooka, "Numerical approach for noise reduction of wind turbine blade tip with Earth Simulator," *J. Earth Sim.*, vol. 2, pp. 11–33, 2005.

[5] S. Oerlemans, P. Sijtsma, and B. Mendez Lopez, "Location and quantification of noise sources on a wind turbine," *J. Sound Vib.*, vol. 299(4-5), pp. 869–883, 2007.

[6] S. Oerlemans, M. Fisher, T. Maeder, and K. Kogler, "Reduction of wind turbine noise using optimized airfoils and trailing-edge serrations," in *14th AIAA/CEAS Aeroacoustics Conference*, 2008.

[7] S. Oerlemans and J. Schepers, "Prediction of wind turbine noise and validation against experiment," *Int. J. Aeroacoustics*, vol. 8(6), pp. 555–584, 2009.

[8] W. Leithead, "Wind energy," *Phil. Trans. R. Soc. A*, vol. 365(1853), pp. 957–970, 2007.

[9] F. van den Berg, E. Pedersen, J. Bouma, and R. Bakker, "WINDFARM perception: visual and acoustic impact of wind turbine farms on residents - final report," tech. rep., 2008.

[10] P. Soderman, "Leading edge serrations which reduce the noise of low-speed rotors," tech. rep., NASA, 1973.

[11] S. Ito, "Aerodynamic influence of leading-edge serrations on an airfoil in a low Reynolds number - a study of an owl wing with leading edge serrations," *J. Biomech. Sci. Eng.*, vol. 4(1), pp. 117–123, 2009.

[12] D. Miklosovic, M. Murray, L. Howle, and F. Fish, "Leading-edge tubercles delay stall on humpback whale (Megaptera novaeangliae) flippers," *Phys. Fluids*, vol. 16(5), pp. L39–L42, 2004.

[13] K. Hansen, R. Kelso, and B. Dally, "Performance variations of leading-edge tubercles for distinct airfoil profiles," *AIAA J.*, vol. 49(1), pp. 185–194, 2011.

[14] F. Fish and J. Battle, "Hydrodynamic design of the humpback whale flipper," *J. Morphol*, vol. 225(1), pp. 51–60, 1995.

[15] F. Fish, L. Howle, and M. Murray, "Hydrodynamic flow control in marine mammals," *Integr. Comp. Biol.*, vol. 48(6), pp. 788–800, 2008.

[16] H. Johari, C. Henoch, D. Custodio, and A. Levshin, "Effects of leading-edge protuberances on airfoil performance," *AIAA J.*, vol. 45(11), pp. 2634–2642, 2007.

[17] M. Stanway, "Hydrodynamic effects of leading-edge tubercles on control surfaces and in flapping foil propulsion," Master's thesis, Massachusetts Institude of Technology, 2008.

[18] D. Custodio, "The effect of humpback whale-like leading edge protuberances on hydrofoil performance," Master's thesis, Worcester Polytechnic Institute, 2007.

[19] H. Pedro and M. Kobayashi, "Numerical study of stall delay on humpback whale flippers," in *46th AIAA Aerosp. Sci. Meeting and Exhibit*, 2008.

[20] H. Yoon, P. Hung, J. Jung, and M. Kim, "Effect of the wavy leading edge on hydrodynamic characteristics for flow around low aspect ratio wing," *Comput. Fluids*, vol. 49(1), pp. 276–289, 2011.

[21] K. Hansen, R. Kelso, and C. Doolan, "Reduction of flow induced tonal noise through leading edge tubercle modifications," in *16th AIAA/CEAS Aeroacoustics Conference Proc.*, 2010.

[22] V. Clair, C. Polacsek, T. L. Garrec, G. Reboul, M. Gruber, and P. Joseph, "Experimental and numerical investigation of turbulence-airfoil noise reduction using leading edge serrations," in *18th AIAA/CEAS Aeroacoustics Conference Proc.*, 2012.

[23] M. Goldstein, "Unsteady vortical and entropic distortions of potential flows round arbitrary obstacles," *J. Fluid Mech.*, vol. 89, pp. 433–468, 1978.

[24] M. Myers and E. Kerschen, "Influence of incidence angle on sound generation by airfoils interacting with high-frequency gusts," *J. Fluid Mech.*, vol. 292, pp. 271–304, 1995.

[25] M. Myers and E. Kerschen, "Influence of camber on sound generation by airfoils interacting with high-frequency gusts," *J. Fluid Mech.*, vol. 353, pp. 221–259, 1997.

[26] M. Lowson, "A new prediction model for wind turbine noise," in *Renewable Energy Int. Conference on Clean Power*, pp. 177–182, 1993.

[27] R. Amiet, "Acoustic radiation from an airfoil in a turbulent stream," *J. Sound Vib.*, vol. 41(4), pp. 407–420, 1975.

[28] J. Scott and H. Atassi, "A finite-difference frequency-domain numerical scheme for the solution of the gust response problem," *J. Comput. Phys.*, vol. 119(1), pp. 75–93, 1995.

[29] D. Lockard and P. Morris, "Radiated noise from airfoils in realistic mean flows," *AIAA J.*, vol. 36(6), pp. 907–914, 1998.

[30] V. Golubev, R. Mankbadi, and R. Hixon, "Space-time mapping analysis of airfoil nonlinear interaction with unsteady inviscid flow," *AIAA J.*, vol. 43(10), pp. 2147–2156, 2005.

[31] H. Atassi, A. Ali, O. Atassi, and I. Vinogradov, "Scattering of incident disturbances by an annular cascade in a swirling flow," *J. Fluid Mech.*, vol. 499, pp. 111–138, 2004.

[32] R. Hixon, A. Sescu, and S. Sawyer, "Vortical gust boundary condition for realistic rotor wake/stator interaction noise prediction using computational aeroacoustics," *J. Sound Vib.*, vol. 330, pp. 3801–3817, 2011.

[33] J. Kim, A. Lau, and N. Sandham, "Proposed boundary conditions for gust-airfoil interaction noise," *AIAA J. Technical Notes*, vol. 48(11), pp. 2705–2710, 2010.

[34] J. Kim and D. Lee, "Generalized characteristic boundary conditions for computational aeroacoustics," *AIAA J.*, vol. 38(11), pp. 2040–2049, 2000.

[35] J. Kim and D. Lee, "Generalized characteristic boundary conditions for computational aeroacoustics part 2," *AIAA J.*, vol. 42(1), pp. 47–55, 2003.

[36] J. Kim, "Optimised boundary compact finite difference schemes for computational aeroacoustics," *J. Comput. Phys.*, vol. 225(1), pp. 995–1019, 2007.

[37] J. Kim and R. Sandberg, "Efficient parallel computing with a compact finite difference scheme," *J. Comput. Phys.*, Submitted.

[38] J. Kim, "High-order compact filters with variable cut-off wavenumber and stable boundary treatment," *Comput. Fluids*, vol. 39(7), pp. 1168–1182, 2010.

[39] P. Migliore and S. Oerlemans, "Wind tunnel aeroacoustic tests of six airfoils for use on small wind turbines," *J. Sol. Energy Eng.*, vol. 126(4), pp. 974–985, 2004.

[40] P. Moriarty, G. Guidati, and P. Migliore, "Prediction of turbulent inflow and trailing-edge noise for wind turbines," in *11th AIAA/CEAS Aeroacoustics Conference*, 2005.

[41] M. Lighthill, "On sound generated aerodynamically I. General theory," in *Proc. R. Soc. Lond. A*, vol. 211(1107), pp. 564–587, 1952.

[42] R. Self, "Jet noise prediction using the Lighthill acoustic analogy," *J. Sound Vib.*, vol. 275(3-5), pp. 757–768, 2004.

[43] N. Curle, "The influence of solid boundaries upon aerodynamic sound," in *Proc. R. Soc. Lond. A*, vol. 231(1187), pp. 505–514, 1955.

[44] A. Dowling and J. Ffowcs Williams, *Sound and sources of sound*. Ellis Horwood Limited, 1989.

[45] F. Farassat, "Acoustic radiation from rotating blades - the kirchhoff method in aeroacoustics," *J. Sound Vib.*, vol. 239(4), pp. 785–800, 2001.

[46] A. Fillos, N. Tachos, A. Fragias, and D. Margaris, "Broadband noise radiation analysis for an hawt rotor," *Renewable Energy*, vol. 32(9), pp. 1479–1510, 2007.

[47] A. Tadamasa and M. Zangeneh, "Numerical prediction of wind turbine noise," *Renew. Energ.*, vol. 36(7), pp. 1902–1912, 2011.

[48] R. Szasz and L. Fuchs, *Wind Power Generation and Wind Turbine Design*, ch. Wind Turbine Acoustics, pp. 153–183. WIT Press, 2010.

[49] T. Dassen, R. Parchen, G. Guidati, S. Wagner, S. Kang, and A. Khodak, "Comparison of measured and predicted airfoil self-noise with application to wind turbine noise reduction," tech. rep., National Aerospace Laboratory NLR, 1997.

[50] P. Moriarty and P. Migliore, "Semi-empirical aeroacoustic noise prediction code for wind turbines," tech. rep., NREL, 2003.

[51] G. Leloudas, W. Zhu, J. Sorensen, W. Shen, and S. Hjort, "Prediction and reduction of noise from a 2.3 mw wind turbine," in *J. Phys Conf. Series*, vol. 75, 2007.

[52] T. Brooks, D. Pope, and M. Marcolini, "Airfoil self-noise and prediction," tech. rep., NASA, 1989.

[53] T. Colonius and S. Lele, "Computational aeroacoustics: progress on nonlinear problems of sound generation," *Prog. Aerosp. Sci.*, vol. 40(6), pp. 345–416, 2004.

[54] J. Scott, "Benchmark solutions for computational aeroacoustics (CAA) code validation," tech. rep., NASA, 2004.

[55] "Third computational aeroacoustics (CAA) workshop on benchmark problems," Tech. Rep. nasa 20010061385, NASA, 1999.

[56] "Fourth computational aeroacoustics (CAA) workshop on benchmark problems," Tech. Rep. nasa_techdoc_20040182258, NASA, 2004.

[57] J. Hardin and D. Pope, "An acoustic/ viscous splitting technique for computational aeroacoustics," *Theor. Comput. Fluid Dyn.*, vol. 6(5-6), pp. 323–340, 1994.

[58] W. Shen and J. Sorensen, "Comment on the aeroacoustic formulation of Hardin and Pope," *AIAA J.*, vol. 37(1), pp. 141–143, 1999.

[59] W. Shen and J. Sorensen, "Aeroacoustic modelling of low-speed flows," *Theor. Comput. Fluid Dyn.*, vol. 13(4), pp. 271–289, 1999.

[60] W. Shen and J. Sorensen, "Aeroacoustic modelling of turbulent airfoil flows," *AIAA J.*, vol. 39(6), pp. 1057–1064, 2001.

[61] W. Shen and J. Sorensen, "Aero-acoustic modelling using large eddy simulation," *J. Phys. Conf. Ser.*, vol. 75, 2007.

[62] W. Zhu, *Aero-acoustic computations of wind turbines*. PhD thesis, Fluid Mechanics Department of Mechanical Engineering Technical University of Denmark, 2007.

[63] R. Ewert, "Broadband slat noise prediction based on caa and stochastic sound sources from a fast random particle-mesh (RPM) method," *Comput. Fluids*, vol. 37(4), pp. 369–387, 2008.

[64] M. Klein, A. Sadiki, and J. Janicka, "A digital filter based generation of inflow data for spatially developing direct numerical or large eddy simulations," *J. Comput. Phys.*, vol. 186(2), pp. 652–665, 2003.

[65] R. Ewert, "RPM - the fast random particle-mesh method to realize unsteady turbulent sound sources and velocity fields for CAA applications," in *13th AIAA/CEAS Aeroacoustics Conference Proc.*, 2007.

[66] R. Ewert, J. Dierke, J. Siebert, A. Neifeld, C. Appel, M. Siefert, and O. Kornow, "CAA broadband noise prediction for aeroacoustic design," *J. Sound Vib.*, vol. 330(17), pp. 4139–4160, 2011.

[67] M. Dieste and G. Gabard, "Predicting broadband fan interaction noise using a random-vortex-particle method," in *20th International Congress on Acoustics, ICA 2010*, 2010.

[68] M. Dieste, *Random-vortex-particle methods applied to broadband fan interaction noise.* PhD thesis, Institute of Sound and Vibration Research, University of Southampton, 2011.

[69] F. Fish and G. Lauder, "Passive and active flow control by swimming fishes and mammals," *Annu. Rev. Fluid Mech.*, vol. 38, pp. 193–224, 2006.

[70] F. Fish, P. Weber, M. Murray, and L. Howle, "The tubercles on humpback whales' flippers: application of bio-inspired technology," *Integr. Comp. Biol.*, vol. 51(1), pp. 203–213, 2011.

[71] D. Miklosovic, M. Murray, and L. Howle, "Experimental evaluation of sinusoidal leading edges," *J. Aircraft*, vol. 44(4), pp. 1404–1407, 2007.

[72] P. Weber, L. Howle, and M. Murray, "Lift, drag and cavitation onset on rudders with leading-edge tubercles," *Marine Technology*, vol. 47(1), pp. 27–36, 2010.

[73] L. Howle, "Whalepower Wenvor blade - a report on the efficiency of a whalepower corp. 5 meter prototype wind turbine blade," tech. rep., Bellequant Engineering, PLLC, 2009.

[74] "Whalepower tubercle blade power performance test report," tech. rep., Wind Energy Institute of Canada, 2008.

[75] M. Murray, T. Gruber, and D. Fredriksson, "Effect of leading edge tubercles on marine tidal turbine blades," in *63td Annual Meeting of the APS Division of Fluid Dynamics*, vol. 55(16), 2010.

[76] T. Goruney and D. Rockwell, "Flow past a delta wing with a sinusoidal leading edge: near-surface topology and flow structure," *Exp. Fluids*, vol. 47(2), pp. 321–331, 2009.

[77] C. Ozen and D. Rockwell, "Control of vortical structures on a flapping wing via a sinusoidal leading-edge," *Phys. Fluids*, vol. 22(2), pp. 021701–1–021701–3, 2010.

[78] P. Watts and F. Fish, "The influence of passive, leading edge tubercles on wing performance," in *12th international symposium on unmanned untethered submersible technology*, pp. 1–5, 2001. Available from `www.appliedfluids.com/UUST01.pdf`.

[79] E. von Nierop, S. Alben, and M. Brenner, "How bumps on whale flippers delay stall: an aerodynamic model," *Phys. Rev. Lett.*, vol. 100, 2008.

[80] P. Weber, L. Howle, M. Murray, and D. Miklosovic, "Computational evaluation of the performance of lifting surfaces with leading-edge protuberances," *J. Aircraft*, vol. 48(2), pp. 591–600, 2011.

[81] J. Ekaterinaris, "Implicit, high-resolution, compact schemes for gas dynamics and aeroacoustics," *J. Comput. Phys.*, vol. 156(2), pp. 272–299, 1999.

[82] M. Visbal and D. Gaitonde, "On the use of higher-order finite-difference schemes on curvilinear and deforming meshes," *J. Comput. Phys.*, vol. 181(1), pp. 155–185, 2002.

[83] C. Tam and J. Webb, "Dispersion-relation-preserving finite difference schemes for computational acoustics," *J. Comput. Phys.*, vol. 107(2), pp. 262–281, 1993.

[84] K. Thompson, "Time-dependent boundary conditions for hyperbolic systems, ii," *J. Comput. Phys.*, vol. 89(2), pp. 439–461, 1990.

[85] D. Bodony, "Analysis of sponge zones for computational fluid mechanics," *J. Comput. Phys.*, vol. 212(2), pp. 681–702, 2006.

[86] J. Freund, "Proposed inflow/outflow boundary condition for direct computation of aerodynamic sound," *AIAA J. Technical Notes*, vol. 35(4), pp. 740–742, 1997.

[87] J. Freund, "Noise sources in a low-reynolds-number turbulent jet at mach 0.9," *J. Fluid Mech.*, vol. 438, pp. 227–305, 2001.

[88] D. Bodony and S. Lele, "Using large-eddy simulation of the prediction of noise from cold and heated turbulent jets," *Phys. Fluids*, vol. 17(8), pp. 085103–1–085103–20, 2005.

[89] B. Morgan and J. Larsson, "Improving low-frequency characteristics of recycling/rescaling inflow turbulence generation," *AIAA J.*, vol. 49(3), pp. 582–597, 2011.

[90] T. Lund, X. Wu, and D. Squires, "Generation of turbulent inflow data for spatially-developing boundary layer simulations," *J. Comput. Phys.*, vol. 140(2), pp. 233–258, 1998.

[91] Z. Xie and I. Castro, "Efficient generation of inflow conditions for large eddy simulation of street-scale flows," *Flow Turbul. Combust.*, vol. 81(3), pp. 449–470, 2008.

[92] A. Smirnov, S. Shi, and I. Celik, "Random flow generation technique for large eddy simulations and particle-dynamics modeling," *J. Fluids Eng.*, vol. 123(2), pp. 359–371, 2001.

[93] T. Baker, "Mesh generation: art or science?," *Prog. Aerosp. Sci.*, vol. 41(1), pp. 29–63, 2005.

[94] L. Eriksson, "Practical three-dimensional mesh generation using transfinite interpolation," *SIAM J. Sci. Stat. Comput.*, vol. 6(3), pp. 712–741, 1985.

[95] R. Sheldahl and P. Klimas, "Aerodynamic characteristics of seven symmetrical airfoil sections through 180-degree angle of attack for use in aerodynamic analysis of vertical axis wind turbines," tech. rep., Sandia National Laboratories, 1981.

[96] J. Kim, A. Lau, and N. Sandham, "CAA boundary conditions for airfoil noise due to high-frequency gusts," in *Procedia Engineering*, vol. 6, pp. 244–253, 2010.

[97] R. Hixon, V. Golubev, R. Mankbadi, J. Scott, S. Sawyer, and M. Nallasamy, "Application of a nonlinear computational aeroacoustics code to the gust-airfoil problem," *AIAA J.*, vol. 44(2), pp. 323–328, 2006.

[98] F. Farassat, "Derivation of formulations 1 and 1A of Farassat," tech. rep., NASA, 2007.